LOCALIZATION

IN DUTCH DUNE SAND AND ORGANIC CLAY

LOCALIZATION
IN DUTCH DUNE SAND AND ORGANIC CLAY

NEW INSIGHT INTO LOCALIZATION MECHANISMS

Proefschrift

ter verkrijging van de graad van doctor
aan de Technische Universiteit Delft,
op gezag van de Rector Magnificus Prof. dr. ir. J.T. Fokkema,
voorzitter van het College voor Promoties,
in het openbaar te verdedigen
op donderdag 1 Juli 2004 om 10:30 uur

door

Xiaohui CHENG

Master of Engineering, Tsinghua Univeristy, Beijing
geboren te Jiangsu, China

DIT PROEFSCHRIFT IS GOEDGEKEURD DOOR DE PROMOTOR:

Prof. dr. ir. F.B.J. Barends

SAMENSTELLING PROMOTIECOMMISSIE:

Rector Magnificus,	Voorzitter
Prof. dr. ir. F.B.J. Barends,	Technische Universiteit Delft, promoter
Prof. dr. ir. K. van Breugel	Technische Universiteit Delft
Prof. dr. ir. F. Molenkamp	Technische Universiteit Delft
Prof. dr. ir. A. Verruijt (em.)	Technische Universiteit Delft
Prof. dr. M.D. Bolton	Cambridge University, Cambridge UK
Dr. ir. E.J. den Haan	GeoDelft Delft
Ass. Prof. ir. A. Scarpas	Technische Universiteit Delft
Prof. dr. ir. J.Blaauwendraad	Technische Universiteit Delft, reservelid

Dr.ir.E.J.den Haan heft als begeleider in belangrijke mate aan de totstandkoming van het proefschrift bijgedragen.

Published and distributed by: DUP Science
ISBN 90-407-2510-1

DUP Science is an imprint of Delft University Press
P.O. Box 98 2600 MG Delft The Netherlands
Telephone: +31 15 27 85 678
Fax: +31 15 27 85 706
Email: dup@library.tudelft.nl

Printed in the Netherlands

Acknowledgement

I feel that I must not let the occasion pass without writing down in words about how much I appreciate the opportunity of learning soil mechanics in Delft. It has been a pleasure for me to participate in the professional activities in both TUDelft and GeoDelft, where I could learn from eminent scientists, engineers and managers over last four years.

It was Professor dr.ir .A.Verruijt who brought me over Delft in 1999, and Professor dr.ir. F.B.J.Barends accepted me to be a Doctoral researcher and ensured the PhD work of mine on the right track. I thank to both of them for supervision and encouragement. Their valuable advices on distinct element modelling of soils are especially appreciated. The financial support granted by Delft Cluster is greatly thanked.

I had the privilege of working closely with Dr.ir.E.J.den Haan. He has been guiding me with keen knowledge of important technical issues, on Dutch organic clays in particular. As advises by him, the investigation of fabric of organic clays and its micromechanical implications was an intensely stimulating experience for me. It is also worth mentioning that I wrote email reports as I thought on a weekly basis, suggested by him as well, producing an accurate, timely history of the initiation, analysis and growth of each task we set out. The enormous communications we had via these weekly email reports have been eventually paid off.

I am grateful to all colleagues involved. Corporation with the group of structural mechanics was pleasant. Mr. J. Olie at GeoDelft greatly helped me with the identification of microbiological items and Soxhlet extraction. Technical assistance from Mr.H.Janssen et.al. at Microlab with ESEM, L.Smidt et. al. of Triaxial Lab at GeoDelft with Triaxial setup and technical staff of Geotechnical lab at TUDelft is kindly acknowledged. Dr. J. Sun and Drs. van Torlen are thanked for their assistance with XRD tests and mineral identification.

Dr. D.Ngan-Tillard has been always supportive since we met at the final stage of my Doctoral research. Prof. V.Osipov, a senior Russian scientist, was patiently answering my questions regarding the lithification of organics on the occasion of a short visit in Holland. The comments that Prof. M. Bolton had were very relevant. Discussions I made with Prof. F.Molenkamp were impressive.

Finally, I am indebted to my dear parents and sisters, X. and friends.

Xiaohui CHENG

Summary

Localization in Dutch dune sand and organic clay

New insight into localization mechanisms

One of the challenging research puzzles in soil mechanics is the subject of strain localization. The investigation of the physico-chemical mechanisms and the conditions under which the strain will localize has been going on for more than a century. The focus of these studies was continuously adapted as new engineering problems occurred or new technologies became available. The objective of the present study is to collect new laboratory evidence of strain localization in Dutch dune sand and organic clay with the emphasis on the application of novel laboratory techniques. In addition to mathematical aspects at the macro level the interdisciplinary knowledge of micro-geology and bio-geochemistry was incorporated in the micro-mechanical approach.

The first part of this thesis describes specific microscopic laboratory findings and their macroscopic effects of a typical Dutch dune sand. Chapter 2 reports on triaxial elemental tests, which were performed to revisit the interpretation of dilatancy of sand and its implication on failure mechanisms. Specific attention was given to pre-peak volume change characteristics. The corresponding characteristic stress state (CSS) was measured with respect to the evolution of deformations. A special mathematical approach in line with Desai yield surfaces was developed to model the observed volume change of sand by incorporating characteristic stress states with an additional state parameter. A hitherto unrecognised intermixing deformation mode, i.e. cone-radial bands of varying density, has been identified. The characteristic stress state is found to be a precursor of the formation of such a deformation mode. Once such an intermixing deformation mode occurs the measured strength, either peak or post-peak strength, is difficult to establish.

Chapter 3 formulates the intermixing deformation mode using the technique of limit analysis. Two failure mechanisms were involved, i.e. a single shear rupture plane and double cones-radial loosening bands. Both associated and non-associated kinematical fields were considered. The Mohr-Coulomb yield criterion was applied. The classical mechanism of energy dissipation in a shear rupture has been adopted. Upper bound solutions were obtained and the orientation of shear-rupture surfaces (cones)-radial loosening bands in a cylindrical sample was formulated in terms of apparent friction angle, apparent dilatancy angle, confining pressure, slenderness of the sample and tensile strength. This finding is important for the interpretation of triaxial compression strength when measured in the laboratory.

Dutch organic clay is the second important subject in this thesis, in recognition of its importance to geotechnical engineering practice in the Netherlands. This material has a distinct mechanical behaviour different from non-organic clays. The reason for its high effective strength index and low coefficient of lateral stress remains as yet unknown. Fundamental aspects of the behaviour of Dutch organic clays, including the effects of strain localization (Chapter 4), the fabric and micro-deformation of organic and clay mineral contents (Chapter 5 and Chapter 6) are reported in this thesis.

Based on observed laboratory behaviour the strain rate dependent characteristics of soft clays was demonstrated and examined in terms of the instability of the material (Chapter 4). The results suggest that the observed phenomena of rate-dependent deformation mechanisms, creep rupture and pre-failure softening are related to this rate-dependent instability. This viscosity-induced instability can lead to strain localization of saturated soft clay, which is different from the critical state. The combined effect of viscosity and drainage was also addressed by demonstrating its correlation with the type of failure of soft clay. The commonly applied undrained conditions adopted for the usual theoretical analysis and the standard engineering interpretation for the strength of soft clay do not occur in the laboratory or practice. Local drainage has to be taken into account and awareness is growing that the introduction of localization into the study of soft clays is relevant, both scientifically and practically.

A high quality electron microscope system (ESEM and EDAX) combined with a mini-loading module was made available. Chapter 5 includes the laboratory investigation of fabric and related micro-deformation of Dutch organic clay with this modern sophisticated experimental technology. Four types of clay states were studied: natural, remoulded, artificial inorganic and fractured. The results suggest that Dutch organic clay has an unusual fabric where microstructures of organics and microfossils play a central role. Emphasis was put on the identification of the complicated microstructures and on live measurement of related micro-deformations in a controlled environment (temperature and humidity). Eventually, at a scale of tens of micrometers, the clay fabric and its micro-deformation characteristics were analysed.

Applying the technique of distinct element modelling (DEM) a sound relation between fabric and common geotechnical properties of clay could be formulated on basis of micro-scale observations (Chapter 6), including an explanation accounting for the fabric matrix suction with regard to the unusual mechanical properties of Dutch organic clay.

Micro-scale approach is promising and inevitable for the enhancement of the fundamental understanding of the fabric of organic clays and its geotechnical implications. Moreover, the study of mechanical behaviour of modified or contaminated clay could benefit from it as well.

Contents

Chapter 1

Introduction

1.1 Practical relevance of strain localization in engineering materials

The localization of strain into shear bands is a fascinating and widely observed phenomenon in engineering materials such as metals, polymers, rocks and soils. It is considered as the initiation to full rupture of these materials. The investigation of the physico-chemical mechanisms and the conditions under which the strain will localize has been going on for more than a century. The focus of methods and studies related to this topic was adapted as new engineering problems occurred, or new technologies became available. The following review of the history in practices will demonstrate the relationship of knowledge development and engineering practice, and explain the importance of a micromechanical approach.

1.1.1 Griffith flaws and unstable Luders bands in mild steel

In extension or compression tests of a mild steel bar, so-called "Luders bands" with a profile of a shallow groove can quickly spread over the whole length of the specimens at a rather regular angle to the axis (Nadal et al, 1931). It was first recorded by the French engineer Luders in 1854. The occurrence and spreading of these fine markings on the surface of mild steel were considered as valuable information for physical implication of the so-called plastic flow surface of strain. It was of great interest to study how these lines started. Such a development was not made until the crystal lattices of steel with the micro-structural imperfections, i.e. Griffith flaws were observed with microscopy. Luders bands were found to be sensitive to these flaws, which can generate an unstable and crack-like propagation of deformation mechanism. Researchers realized that the microstructure of a material is decisive to the patterns of plastic strain.

1.1.2 Fissures and dilatant hardening in saturated natural rocks

When specimens of natural rock are compressed, strain localization, usually referred to as "faulting" in rocks, is observed. It arises from frictional sliding along closed fissures. The final macroscopic faulting may connect a large number of such fissures with varying orientation sometimes. When rocks are saturated and drainage is limited, a drop in pore pressure will occur when fissuring rocks tend to dilate. According to the principle of effective stress, the rocks behave stiffer (hardening). This phenomenon was observed in triaxial tests on saturated rocks (Brace and Martin, 1968) when loading was rapid. Fracture continued after this dilation-related hardening. During earthquake motion and buried nuclear explosions such a phenomenon in saturated rocks is to be expected (Frank, 1965).

1.1.3 Residual strength and progressive failure in overconsolidated clay and clay shales

A well-known example in clays is the progressive failure in slopes of overconsolidated clay and clay shales. Slides of natural clay slopes caused by progressive failure were studied (Bjerrum et al, 1967; Teunissen et al, 1995). Two kinds of geological conditions were distinguished. One was the slide occurring in overconsolidated clay with weak bonds, the other occurred in a zone of the weathered clays (or clay shales) with strong diagenetic bonds. An important observation of these slides was that the average shear stress along the failure surface bears resemblance to the residual shear strength, independent of water content and liquid index, rather than to the peak strength. The ultimate stability of natural slopes depends on the residual shear strength, which is a fraction of peak strength. In addition, excess pore pressures can influence the slope stability either by stimulating or delaying progressive failure. If however all stability calculations are based on the residual shear strength of clays, a conservative and rather expensive solution, especially for a temporary slopes in stiff clays and clay shales is obtained. Although the mechanism of progressive failure has not been fully understood, field observations have suggested that the mechanism of crack and slip-line propagation often take place.

1.1.4 Transient dilatant hardening in saturated sands

One of the major concerns in soil mechanics was and is associated with settlement and stability of ground composed of cohesive soils. In this regard clay has been studied extensively. Cohesionless soil is recognized as a more stable material. This view is true, however, only under the long-term sustained loading conditions. If loading is dynamic, or rapid enough or repetitive, the situation is reversed. The resistance of cohesionless soils against failure tends to decrease under dynamic loading, particularly when they are saturated. The sudden loss of strength (softening) with respect to the fast loading conditions is a significant feature of loosely deposited cohesionless soils. It is known as liquefaction. Strain localization hardly takes place in this case. However, if densely deposited cohesionless soils are concerned, such as dense sands, dilantant hardening could occur. The mechanics of dilantancy was first discussed by Reynolds (1886). Dilatancy is a property of a dense granular mass which under shear will increase its volume (Rowe, 1969). The corresponding reduction of pore pressure will increase the inter-particle forces at contacts and consequently the strength (hardening). An example in daily life is the firmness of wet sand on a beach (Vardoulakis, 1995). Sand on a beach is much firmer underfoot where it is fully wetted with only a very thin film of moisture on the top, than where it is dry or totally submerged. Because of high permeability of sands dilatant hardening is not sustainable. Localized failure will occur in due time.

1.2 Laboratory developments in characterization and measurement of strain localization in soils

A number of experimental studies have been carried out over the last four decades to reveal the physical mechanism of shearing bands or rupture layers in sands and clays. The objectives of these studies are outlined below. A few experiments are described in more detail to highlight the main laboratory findings.

1.2.1 Influence of boundary conditions on failure patterns
The majority of tests related to strain localization over the last decades were carried out to investigate the influence of the boundary conditions imposed by end platens and membranes on the initiation, inclination and thickness of shear bands (Roscoe et al, 1963; Bishop et al, 1965; Hettler et al, 1984; Tatsuoka et al, 1984; Drescher et al, 1982). The results suggested that the slenderness of specimens and end platen restraint are responsible for the development of the non-uniform deformation observed in tests. Measurements of local strains become relevant to the understanding of the boundary effects on the material behaviour studied. But uncertainties involved in measurements of local strain and local drainage certainly bring more difficulties in soil laboratory tests. The techniques being used need to be improved for more reliable measurements.

1.2.2 Investigations of the influence of lack of homogeneity and isotropy of soil samples
The studies in this category were carried out to reveal the relationship between the "inherent" properties of tested soil samples, such as homogeneity and isotropy, and the observed failure modes.

The mechanical behaviour of a loose saturated assembly of sand particles seems quite sensitive to its microstructure. Ishihara (1993) has mentioned in his Rankine lecture that three widely used procedures for the preparation of remoulded loose sand samples, known as wet tamping, dry deposition and water sedimentation methods, will create different fabrics. The induced fabrics are presumed to be responsible for the different mechanical behaviour of saturated loose sands as observed. Arthur (1977) carried out an interesting test in order to emphasize the influence of anisotropy, i.e. shearing an already ruptured sample in a shear box under plane strain conditions. The rupture-induced anisotropy of shear strength was significant. Tatsuoka et al (1990) carried out drained plane strain compression tests of Toyoura sands, from which a correlation of the relative bedding plane direction of sample with the orientation of shearing bands was found. Changes of sand fabric in the simple shear test were studied by Oda (1999). Buckling of column-like clusters of sand particles was identified as the cause of the initiation and development of shear bands.

Vardoulakis and co-workers (1982, 1995) performed biaxial tests on deliberately imperfected sand samples with either an interior density imperfection or a surface notch. The results showed that a surface notch completely changed the pattern of shear bands whilst a small inhomogeneity in density only slightly influenced the behaviour of samples.

1.2.3 Investigation of the effect of different loading paths
Variable loading paths are subject to shear apparatuses. The limitations of different shear apparatuses were examined by Arthur et al (1980) and Molenkamp (1998). Experimental conflicts related to the development of shear bands in terms of variable inclinations and localizations were considered as the results of these limitations, in which two loading parameters, i.e. the ratio of incremental deviator stress to incremental mean stress and the rotation of the principal stresses, were analyzed. The more significant the rotation of the principal stresses, the less the shear bands develop. The higher the ratio of the incremental stress, the more the shear bands develop.

1.2.4 Inclination of rupture surface in simple shear tests

Roscoe & Schofield et al. (1960s, 1970) introduced radiography (X-or γ ray methods) into the laboratory research of soil mechanics in order to "take a good look at rupture layer". During simple shear tests (in a long simple shear box) on medium dense sand (Leighton Buzzard rounded sand, Gs=2.65, particle size 600-850um), horizontal rupture zones were observed. The conclusion was that the rupture surface develops along the direction of zero-extension and not along a plane on which the ratio of the shear stress to the normal stress is a maximum. In a following model test on a vertical cut with a height of 30cm using the same medium dense sand, the wall rotated with respect to toe into the sand, i.e. classical passive earth pressure problem. One member of the zero-extension line family coincided remarkably well with the observed rupture surfaces. An important conclusion was that in any element within the sand a rupture surface could develop along a plane directed in zero-extension at the instant when the greatest stress ratio is reached on any other plane through that element. This condition leads to the so-called Roscoe's angle, that is the inclination angle of a rupture surface with respect to the minor principal stress direction, $\pi/4+\psi/4$, and ψ is the dilation angle at peak, which is different from Coulomb's solution $\pi/4+\varphi/4$, where φ is the internal angle of friction.

1.2.5 Varied orientations of shear bands in biaxial tests

Arthur and Dunstan (1982) carried out plane strain biaxial tests on fine Ham River sand (mean size: 600-850 μm) and the coarse Leighton Buzzard sand (mean size: 1200 -1680 μm). Tests clearly demonstrated that the orientations of rupture layers were mainly related to the particle size, and secondarily to mean stress level, the relative magnitude of the intermediate principal stress and particle shape.

1.2.6 Complex patterns of strain localization in triaxial compression tests

Since the 1980's, Hostun RF sand (D_{50}=320 μm, uniformity coefficient=1.7, Gs=2.65) has been tested as a reference material to study the evolution of shear bands in triaxial tests by Desrues and Chambon et al (1996). With the advent of non-destructive detective methods such as x-rays or gamma rays and the techniques of False Relief Stereophotogrammetry (F.R.S.) and Computed Tomography (CT), it became possible to measure the change of density of specimens quantitatively. In triaxial tests, more or less complex localization patterns can develop in the specimens, depending on test conditions. Constraints favouring symmetry induced multiple localization modes, while circumstances favouring asymmetric breakage, such as biased density profile, badly centred specimen, tilted platens and local weakness of the material, were likely to produce distinct localization modes. The final plateau observed in the corresponding volumetric strain-axial strain curves for dense dilating specimens was not physically relevant. It should be interpreted not as a manifestation of a limit void ratio but as an effect of the strain localization process inside the specimens. Apparently, shear bands may develop on a random basis in laboratory tests, and if local LVDT pairs installed were not able to eventually capture them the plateau of volumetric stain was certainly observed.

1.2.7 Localization and liquefaction in saturated loose sands

For loose water-saturated sand type, Castro (1969) distinguished A and B type liquefaction behaviour. Type A behaviour describes the response where after attaining an initial peak, the shear stress reduces to a constant value after relatively large strains, so called liquefaction. Type B behaviour describes the response where the shear stress reduces to a minimum value followed by a subsequent increase in shear stress, so called limited liquefaction. It was suggested that during steady-state deformation after liquefaction, the original microstructure of sand has been completely destroyed and reworked into a flow structure. Han and Vardoulakis (1991) presented experimental results showing that strain localization does not develop in undrained compression of loose sand, whereas data presented by Mokni (1992) indicates it does. Finno and Mooney et al (1996, 1998) performed plane strain tests on subrounded or subangular loose sand (D_{50}=0.32 mm) under a wide range of confining pressures. Based on the lateral local deformation measured by LVDT's at the upper and lower points of specimens, they could locate the onset of permanent shearing band. They found that in all plane strain experiments concerning undrained compression of loose uniform sand a period of uniform deformation was followed in sequence by the onset of non-uniform deformations, attainment of maximum effective stress ratio and complete formation of a persistent shear band. Before that persistent shear band, parallel crossing bands were often observed by stereophotogrammetry.

1.2.8 Microstructure of shear bands in sand

Since the 1970's, Oda et al have paid much attention to the microstructure of a granular assembly mainly by X-ray photography and microscopy. They studied the drained plane strain behaviour of Toyoura sand (D_{50}=0.206 mm, a uniform dune sand, subangular quartz and feldspar) and Ticino sand (a uniform river sand, D_{50}=0.527 mm, consisting of angular quartz and rock fragments). At the end of the tests, the samples were impregnated by a resin-solvent mixture, and several thin sections (about 5mm or 10mm in thickness) were cut out of the central portion of each sample with a diamond saw for the x-ray photographs observation. Several other thin sections (about 0.3mm thick) were taken for optical study. They described the main characteristics of microstructure of permanent shear bands as follows: The particles inside shear bands reoriented towards the general shear band direction. The boundaries of the shear band were not exactly straight, but gently curved. The particle orientation changed sharply at shear band boundaries. Very large voids, which can exceed the corresponding maximum void ratio, appeared almost periodically along a shear band. The thickness of the shear band was about 7 to 8 times the mean particle size. Based on these observations, they suggested that the fabric or microstructure of sand consists of particle columns, and that their development during the test is responsible for the macro stress-strain behaviour. They related the formation of the shear band to the buckling of those particle columns.

1.3. Developments of strain localization theories

1.3.1 Coulomb and Roscoe solutions

The technique most often used to interpret the observed shear bands is the limit equilibrium method. Solutions to the orientation of shear bands can often be obtained by assuming failure surfaces of various rather simple shapes (i.e. velocity characteristics), such as plane, circular or log spiral, and by using Coulomb's failure criterion (1773). Another approach, the slip-line method (Sokolovski, 1965: cf Lee (ed), 1968), was developed to construct the slip-line network based on slip-line differential equations (i.e. stress characteristics). Further development of limit analysis of perfect plasticity of materials (Drucker and Chen, 1970s) classified limit equilibrium solutions as upper bound solutions, but not as exact as rigorous upper bound solutions. On the other hand, Sokolovski's solution was an example of lower bound solutions, if soil behaves as an associated plastic material, i.e. the velocity and stress characteristics at the moment of failure are identical. Unfortunately, soils in general do not obey this associated flow rule. This is the reason why the orientations of rupture layers in soils have received much attention in research. Two predications are normally examined, i.e. the Coulomb solution and the Roscoe solution.

The Coulomb solution states that the shear bands are parallel to the surfaces, on which the stress ratio satisfies the Coulomb criterion, this surface being known as the maximum stress obliquity plane. However, Roscoe's theory proposes that the shear bands are parallel to the line of non-extension. According to laboratory tests, the difference between the Coulomb orientation and the Roscoe orientation is quite significant as the dilatancy angle is usually much smaller than the friction angle with the maximum difference being up to 30^0.
Besides, the double sliding model developed based on a 2D failure mode of double sliding (de Josselin de Jong, 1988) incorporates two special features of inelastic material: non-coaxiality and non-associativeness. It implies that rupture layers could develop at more variable orientations rather than Coulomb and Roscoe solutions. Taking dilatancy and free rotation of the soil mass into account the model has been extended to predict more sophisticated inelastic behavior of soils (Teunissen, 1995).

1.3.2 Instability of elasto-plastic materials

After Hadamard started the study of the stability of elastic materials in 1903, Drucker, Thomas, Hill and Mandel did pioneering work for inelastic materials in the 1960's. Rice and Rudnicki (1975, 1976) developed the stability conditions for the constitutive descriptions of inelastic response of rocks. A few stability conditions are listed below.

(1) Hadamard theorem
Hadamard in 1903 showed that for an isotropic elastic material two material constants are involved, while the shear modulus is definite positive and the Poisson ratio is between -1 and 0.5.

(2) Drucker's stability postulate or Hill's stability postulate (Vardoulakis et al, 1995)
Based on thermodynamic considerations, inequality (1.1a) below was proposed by Drucker (1951) as a condition of material stability. Using a different approach based on the principle of maximum work, Hill (1958) proposed inequality (1.1b), which in fact provides an extension of the Drucker's postulate.

$$d^2W^p = d\sigma_{ij} \cdot d\varepsilon_{ij}^p \geq 0 \qquad (1.1a)$$

$$d^2W = d\sigma_{ij} \cdot d\varepsilon_{ij} \geq 0 \tag{1.1b}$$

where d^2W^p is the second order of the plastic energy dissipation or work done, d^2W is the second order of the energy dissipation or work done, $d\sigma_{ij}$ is the incremental stress tensor, $d\varepsilon_{ij}$ are the incremental strain tensors, and $d\varepsilon^p_{ij}$ is the incremental plastic strain tensor.
These two stability conditions proved to be a sufficient but not a necessary stability condition, especially for frictional material, such as soils, rocks, concretes etc. Experiments on sand (Lade et al, 1990) have shown that the second increment of plastic work, d^2W^p can be negative while specimens that exhibit dilation remain stable.

(3) <u>Mandel's stability condition</u> (Vardoulakis et al, 1995)
Based on the assumption that a stable material is able to propagate a small perturbation in the form of waves, an additional stability condition was proposed by Mandel (1960). A wave of perturbation can propagate in a material with an elasto-plastic stiffness matrix A, along the direction α, if and only if all the eigenvalues λ_i (i=1,2,3) of the characteristic matrix M (or acoustic tensor), are positive. If one of λ_i is negative or null, then one of the components of the perturbations cannot propagate. This corresponds to instability in terms of the appearance of strain localization along a certain direction.

$$M_{ik} = A_{ijkl} \cdot \alpha_j \cdot \alpha_l \tag{1.2}$$

(4) <u>Rice and Rudnicki' conditions for localization</u>
The pioneering work done by Rice and Rudnicki (1975) on the conditions for localization combined Mandel's stability condition with a realistic and elaborate constitutive description of compressed brittle rock. A hardening function in terms of the cumulative plastic strain was formulated and mathematically examined. Critical values of the hardening modulus with respect to occurrence of material instability were found for various stress paths. Similar calculations were applied to an isotropic-hardening and non-associated constitutive model, which has been widely used in soils and rocks. Several theoretical implications based on those calculations are worth mentioning. Within the framework of theory of plasticity, the material instability depends on the subtleties of the incremental constitutive description, i.e., especially the yield-vertex and non-normality condition. Related to the prevailing stress-state, strain localization may occur even if the material is continually hardening or when it passes the peak strength and is progressively softening. It means that the onset of strain localization is not guaranteed.
Following Rice & Rudnicki's approach the theory of strain localization has been developed for soils (Houlsby, 1980). Not all localization phenomena as observed can be expected to fit their concept, such as the localization mentioned before (Luders bands and Griffith flaws). Apparently, these examples require that the theory of strain localization be generalized by considering the highly non-uniform conditions near the tip of the crack zone. Although Mohr has related the failure of a material to "localized" deformation 100 years ago, this problem is still a challenge today

1.3.3 Drainage conditions and material instability of water-saturated soils

Drainage conditions play an important role in the instability of water-saturated soils. As mentioned before the discussion of instability of water-saturated materials are complex, if local drainage occurs. Such effects of local drainage on the evolution of deformations in saturated soils are clearly observed in laboratory tests. If locally undrained conditions could be imposed, the instability of saturated soils can be discussed straightforwardly in terms of effective stress analysis (Molenkamp, 1991; Vardoulakis, 1995). Rice (1975) made already clear that local drainage should be taken into consideration.

The analysis of former studies given above was aimed at gaining insight into the phenomenon of liquefaction. Liquefaction of water-saturated granular materials is considered as an instability problem of saturated material subjected to locally undrained conditions. A uniform bifurcation mode of on-going deformation occurred due to the occurrence of a zero eigenvalue of the acoustic tensor as defined in equation (1.2). The sooner it occurs, the stronger the contraction of the soil skeleton, and the more distinct is the bifurcation mode. Which bifurcation mode is predicted for saturated soil, either liquefaction or shear bands, depends on the assumed constitutive laws. A uniform bifurcation mode, i.e. liquefaction is supposed to be the dominant mode for loose saturated soils.

Applying perturbation analysis for one-dimensional pore water pressure developed in a saturated rock layer, the material instability of dilatant hardening was examined (Rice, 1975). Considering the boundary conditions of simple shear the perturbations in pore water suction satisfy

$$\frac{\partial^2 p}{\partial y^2} = \frac{1}{c}\frac{\partial p}{\partial t}, \qquad c = \frac{kKH}{\gamma_w (H + \mu\psi K)} \tag{1.3}$$

in which, p: pore water suction [kPa]; K: elastic compressibility modulus [kPa]; μ: the friction coefficient; k: permeability [m/s]; ψ: dilatancy ratio; H: hardening modulus of rock skeleton [kPa]; γ_w: weight density of pore water.

It is apparent that non-uniformities of suction dissipate as long as $c>0$, which implies that the material is stable. As both K and k are positive, the dilatant hardening of saturated rocks is stable only in those circumstances for which the underlying drained deformation would be stable, i.e. $H>0$ (hardening). This explains that induced pore water pressures can temporarily (without drainage occurs) stabilize a saturated rock mass against failure.

1.3.4 Application of fracture mechanics

Less attention has been given to the development of complete slip surfaces. Skempton (1964) and Bishop (1954) suggested that fracture mechanics concepts might explain progressive failure of slopes. Bjerrum et al (1967) discussed a model of progressive failure in terms of stress concentrations at the tip of a slip surface. By using a simple model based on fracture mechanics for the growth of those slip surfaces (called "shear bands" for progressive failure problem), Rice and Palmer (1973) considered the shear band simply as a surface of discontinuity on which a distinct relation between shear stress and relative displacement exists. Using specific analysis (J-integral) they derived the conditions for the propagation of a concentrated shear band.

1.3.5 Micro-mechanics and distinct element modelling

Microstructure of soils and its engineering implications have been paid much attention (McDowell and Bolton, 1998). Recent development of microscopy and micro-loading facilities for soils supported by distinct element modelling enables more advanced studies of micro-soil mechanics. This approach has been followed in the research reported in this thesis, and allows "a better look at the rupture layer".

1.4 Objective, approach and outline of the thesis

The objective of this research is the investigation of strain localization in soils by collecting further laboratory evidence. As the subject concerned is probably one of best-known research puzzles in soil mechanics the emphasis was placed on the new laboratory techniques as well as the incorporation of interdisciplinary knowledge (micro-geology and bio-geochemistry). A comprehensive literature review included in this chapter was essential to knock at a new door to this puzzle. Nevertheless, the fundamental approach, such as mathematical aspects of physical modelling and micro-mechanics seem inevitable with respect to proper interpretations of the experimental results.

At the early stage of this research, localization, fissuring and distinct element modelling in soils and rocks were the focus. Triaxial elemental tests on Dutch dune sand were designed to revisit the interpretation of dilatancy of sand and its implication on failure mechanisms, supported by mathematical modelling. Macroscopic studies of sand by incorporating microscopic laboratory findings are the topic in the first part of this thesis, i.e. Chapter 2 and Chapter 3.

Subsequently in this research, Dutch organic soft clay was also adopted as subject of study, in recognition of its importance to geotechnical engineering practice in the Netherlands. This material has a distinct mechanical behaviour different from non-organic clays and e.g. the reason for its high effective strength index and low at rest coefficient of lateral stress (Den Haan, 1999, 2002) remains unknown. The fundamental aspects of the behaviour of Dutch organic clays, including the effects of strain localization and fabric of both organic and clay mineral contents, has been studied. A high quality electron microscope (ESEM) combined with a specially developed micro-loading module suitable for the study of micro-mechanical stability of organic clays was made available at the Microlab of TU Delft. The approach of distinct element modelling has been applied for the basic interpretation. These topics compose the second part of the thesis (Chapter 4, Chapter 5 and Chapter 6).

Chapter 2

Experimentation and Modelling of Dilatancy and Failure Mechanism of Sand in Triaxial Compression

2.1 Introduction

Routine drained triaxial compression, abbreviated as RDTC, is employed in laboratory investigations to describe sand behaviour. Discrepancies and difficulties in measurements exist for many years in terms of (a) diverse failure patterns of samples, (b) disturbed softening regime. Amongst others the investigation of volume changes, either contraction or dilation, at large shear strain level, is limited by these experimental difficulties. Tatsuoka (1982) drew attention to the reconstitution process of cylindrical sand samples and the subsequent saturation and pre-loading process. He provided how the stress and strain history of samples looks like in the reconstitution process, and estimation Molenkamp et al. (1980) made efforts to elaborate the measured volume change of sand by looking at effects of membrane penetration and loading platen friction. A large and flat triaxial setup was developed as an adapted version of a routine triaxial setup by Hettler and Vardoulakis (1984) to study geometric softening of sand samples in a RDTC test. An argument was made by Arthur (1980) that the rotation of the axis of principal stress is a missing parameter in RDTC. Here, another important aspect in the interpretation of the RDTC test is considered, i.e. the combined effect of indentation of end platens and flexible confinement in the radial direction of a sample in the triaxial cell. This aspect remained unnoticed due to the standard setup for a RDTC test.

Recently, Desrues et al. (1996) have visualized the complex evolution of deformation of sand in a RDTC test by CT scanning, which evidently proves a pattern of induced density variation rather than a simple shear band. Actually, back in the 1970s, similar detailed deformation patterns have been recorded for concrete and rock in a so-called double punch test setup (Chen, 1975). Inspired by laboratory observations, such a deformation mode is repeated in this study by introducing a combination of the effects mentioned above on a cylindrical sand sample in communicating vessels. The deformation mechanism being considered is a mixture of two well-defined mechanisms: shear bands for a frictional material and cracks for a cohesive material. The routine triaxial testing setup is in this respect intermediate between the squeeze test such as that of Hettler and Vardoulakis (1984) and the punch test proposed by Chen (1975). In such a routine setup most soil samples failed axial-symmetrically in a shape of a barrel coupled with a horizontal, circular shear plane rather than a single shear plane.

A transition state from contraction to dilation at relatively small strain levels can take place in some stress paths. For dense sands or stiff clays these states can appear in the early shear-hardening regime. These so-called characteristic states can be captured in the laboratory, but little information exists on the effects of the stress path and on correlations with strain localization. With this point of view re-interpretation of measured volume changes was done by Jakobsen, Praastrup & Ibsen (1999). They tried to understand the characteristic stress state within the framework of elasto-plasticity. They suggested that there is a need to study the role of these stress states in relation to the volume changes of sands. This aspect is a primary objective of the present study.

This chapter starts with a presentation of the RDTC testing program on a Dutch fine sand (Eastern Scheldt Sand, abbreviated as E.S. Sand), in which specific attention is given to the pre-peak volume change characteristics. The corresponding characteristic stress state, abbreviated as CSS, is measured with respect to the deformation evolution of a sand sample. A new deformation mechanism is identified. The conflicts and difficulties of interpretation of volume change of sand are addressed in case that a single deformation mechanism is implied. Following this experimental work, an advanced mathematical model based on Desai yield surfaces (Desai, 1984) is developed within the framework of elasto-plasticity to model the volume change of sand by incorporating characteristic stress states and a special state parameter. The fit between laboratory results and model predictions is examined to demonstrate the suitability of the proposed advanced model for the interpretation of a routine triaxial compression test at the pre- or near- peak moment.

Table2.1 Classification properties for E.S. Sand

Properties	Value
Specific gravity, Gs	2.65
Max. void ratio, e_{max}	0.859
Min. void ratio, e_{min}	0.528
Mean grain size, D_{50}	0.156
Uniformitycoeficient,D_{60}/D_{10}	1.7
Roundness of sand grains	sub-rounded

2.2 Laboratory investigation of volume change and deformation modes

2.2.1 Sand tested, preparation and testing procedures

Tests are performed on reconstituted samples of E.S. Sand, which mainly consists of quartz mineral. The grains can be characterized as sub rounded. The classification properties of the sand are summarized in Table2.1. The tests were performed in a triaxial apparatus modified as proposed by Pedersen and Molenkamp (1981). Measurements of axial load, axial displacement, cell pressure, pore pressure or back pressure, and volume change are automatically and electronically collected for processing. Tests were performed on medium dense and dense specimens with relative densities of 0.4 and 0.7, respectively, and specimens were sheared at two confining pressures. The medium dense specimens (MF series) were prepared with an average initial void ratio of 0.725 in a cylindrical mould by the method of air pluviation. The dense specimens (DF series) were prepared in the same mould by the method of multi-stage vibration, with an average initial void ratio of 0.625. Both preparation methods were acceptable with respect to reproducibility. The homogeneity of reconstituted specimens was not checked due to technical limitations. However, it could play a role in the dilatancy and deformation mechanism.

Since the stress and strain states of the specimen should stay homogeneous during an elemental test, a lubrication layer composed by vacuum grease (30-50 μm in thickness) and a latex disk (200 μm in thickness) was placed on the top and bottom end platens. For the same reason, the specimens with a height and diameter of approximately 66mm were prepared. Some were made slender with a slenderness ratio of 2 (in MS series, contrasting with the flat samples of the MF series) for comparison.

After preparation of the dry sand specimens mentioned above, they were saturated using a combination of CO_2 saturation and water percolation at a water head of around 40 cm. Subsequently, the specimens were isotropically consolidated at a loading rate of 3 kPa per minute, and sheared at a constant axial strain rate of 3% per hour for strain controlled tests, or at a constant axial stress rate of about 3 kPa per minute for stress controlled tests. All specimens were sheared into the softening regime. An unloading and reloading stress path with a stress rate of 10 kPa per minute was followed on some specimens of dense sand to evaluate the elastic behaviour. Three more quick tests, with shear rates of 0.4% per minute for strain controlled tests or 12 kPa per minute for stress controlled tests, were carried out to investigate the influence of loading rates on the characteristic stress states. At the end of the shear tests, the geometrical changes of several specimens with respect to their initial states were recorded by level gauges, digital camera and a magnifier.

2.2.2 Stress path and stress level in the laboratory

The figure 2.1 shows the stress paths and levels involved in the present study on medium dense and dense specimens.

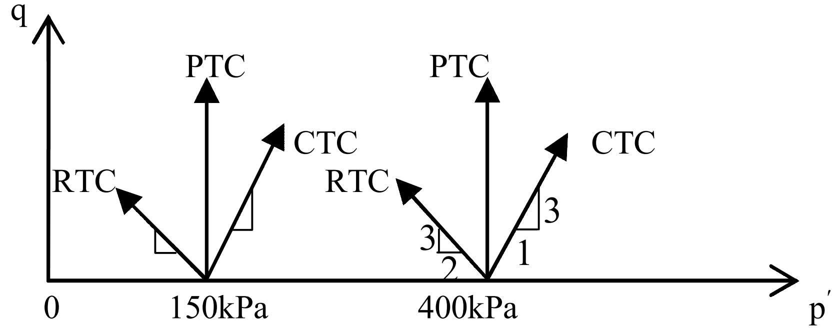

Fig. 2.1 Experimental stress paths and levels
(Notes, CTC: Conventional Triaxial Compression; PTC: Constant Mean Stress Compression; RTC: Reduced Confining Pressure Compression)

2.2.3. Error Analysis and evaluation of the tests

The accuracy and reproducibility of experiments are considered in detail. The errors of experiment data has been attributed to (1) ignoring stress and strain histories during the preparation of samples, and (2) lack of accuracy of the applied measuring techniques. Following the contributions from Tatsuoka & Molenkamp et al (1980s) on this subject, their conclusions are considered applicable to the error analysis here. In this regard the test data can be elaborated for the calibration and validation of mathematical models.

(1) Correction of systematic error

The error analysis on triaxial tests (after Tatsuoka et al., 1982) has given a good insight in the accuracy of the experimental data obtained. The stresses can be measured accurately. The main sources of errors involve the deformation caused by the flexibilities of the load cell, the cap block, the loading frame and the membrane penetration. The total errors can be split into a systematic and a stochastic component, which components can be evaluated according to the approach described next.

The vertical displacement of the sample was measured with a displacement transducer (LVDT) connected to the piston and resting on the frame. So the measured displacement was not only the displacement of the sample, but also the displacements due to the flexibility of the frame, the load cell and the cap block. The systematic error in the vertical displacement is dependent on the magnitudes of the vertical force measured from load cell and the cell pressure measured from a cell pressure transducer. The equation expressing the systematic error reads as follows, which is slightly different from Molenkamp's expression (1982):

$$CD = 1.33\times10^{-4}\times F + 3.39\times10^{-7}\times CP \qquad (2.1)$$

in which, CD (mm) is the systematic error due to flexibilities in the set-up; F (N)= the vertical force; CP (Pa) is the cell pressure.

The axial displacement across the sample is defined by:

$$\Delta_a = \Delta_{a,measure} - CD - \alpha \qquad (2.2)$$

where Δ_a (mm) is the completely corrected axial displacement; $\Delta_{a,measure}$ (mm) is the measured axial displacement from LVDT; *CD* (mm) is the systematic error due to flexibilities in the set-up; α (mm) is the membrane penetration along lubrication layers.

The volume change of the sample was measured by weighing the amount of water expelled from the sample into a reservoir with a diameter of 10 cm on a balance, which method far exceeds the common burette method in accuracy. The reservoir was connected to the pore water of the sample via a drain. The systematic error of volume change of the sample mainly comes from membrane penetration, which depends on the effective stress σ' on the membrane, the Young's modulus of the membrane, the thickness of the membrane, the mean grain size and voids ratio of the sample. For the purpose of simplification, the following approximate expression has been chosen to estimate membrane penetration for present triaxial tests (based on Molenkamp and Luger, 1981)

$$\frac{\alpha}{d_{50}} = \frac{t}{d_{50}}(0.074 + 0.078\ln\frac{d_{50}}{t})(\ln\frac{\sigma}{E} + 4.450) \quad \text{, for } \frac{\sigma}{E} \geq 0.05 \tag{2.3}$$

in which t/d_{50} is the ratio of membrane thickness to mean grain size (=1.28 for this calculation); σ/E is a strain measure; σ is the mean effective stress and E the Young′s modulus of the membrane.

Substituting the value of t/d_{50} into the expression (2.3), the membrane penetration (mm) during current triaxial tests is determined by the following equation:

$$\alpha = 0.01\ln(\sigma/E) + 0.05 \quad \text{for} \quad \frac{\sigma}{E} \geq 0.05 \tag{2.4a}$$

$$\alpha = 0.02 \quad \text{for} \quad \frac{\sigma}{E} < 0.05 \tag{2.4b}$$

The correction for volume change due to membrane penetration during consolidation and shear test along the circumference and the lubrication layers based on geometric considerations is expressed by:

$$CV = \frac{\pi}{2}D^2\alpha + \pi DH\alpha \tag{2.5}$$

in which, CV (mm^3) is the correction for volume change due to membrane penetration along circumference and lubrication layers; D (mm) is the momentary diameter of sample; H (mm) is the momentary height of sample.

The momentary corrected volume change is defined by

$$\Delta_v = \Delta_{v,measure} - CV \tag{2.6}$$

in which Δ_v (mm^3) is the completely corrected volume change; $\Delta_{v,measure}$ (mm^3) is the measured volume change from water volume balance.

<u>(2) Accuracies of the calculated stress and strain</u>

The momentary deviatoric and volumetric strains are defined by

$$\varepsilon_a = \frac{\Delta D_a}{H_i} \quad \text{and} \quad \varepsilon_v = \frac{\Delta vol_m}{vol_i} \text{, respectively.}$$

Similarly, the momentary deviatoric and mean stress are defined by

$$q = \frac{F_{v,m}}{Vol_m / H_m} \quad \text{and} \quad p' = q/3 + \sigma_{cell} - \sigma_{pore}$$, respectively.

By applying the previously explained error formulae, the orders of accuracies of stress and strain are found to be ±0.5% for strain and ±1kPa for stress. The values are relatively small and they inspire confidence in the test results.

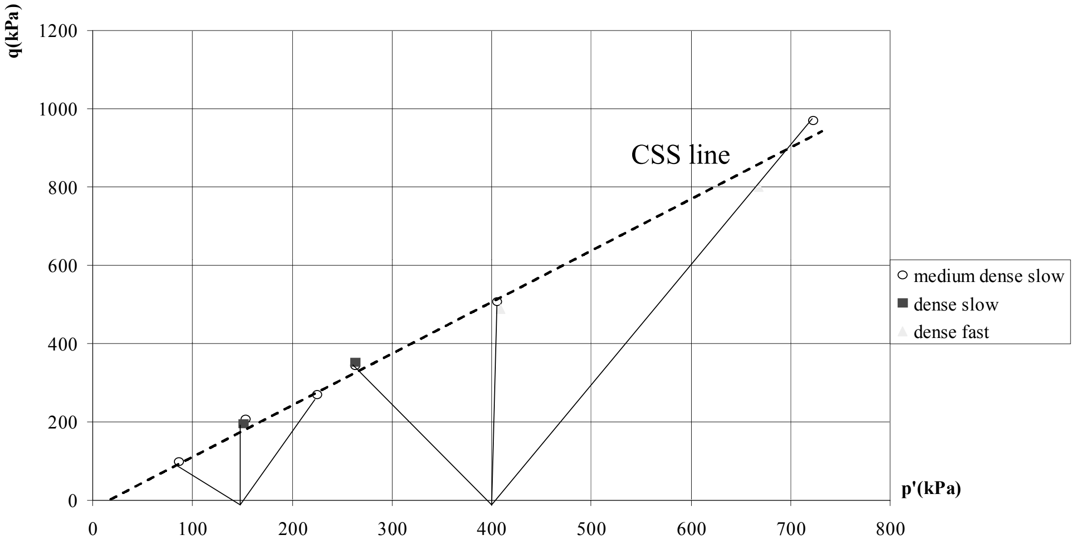

Fig. 2.2a Observed independence of characteristic stress states (CSS) on stress path in TC-tests.

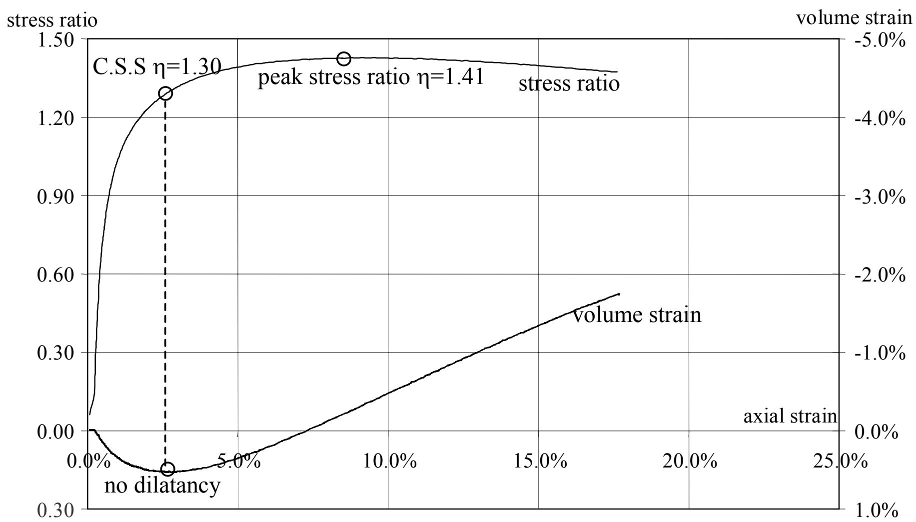

Fig. 2.2b Sand from zero-dilatancy (C.S.S), through peak stress ratio towards its critical state (Test mf1 data)

(3) Elaboration of testing data

All tests have been elaborated according to the expressions mentioned above and are presented in various graphs (see Appendix of Chapter2), in terms of (a) stress ratio η versus axial strain, (b) deviator stress q versus axial strain, (c) volume strain versus axial strain, and (d) compression lines on semi-logarithmic scale.

2.2.4 Characteristic stress states

The characteristic stress state in sand is a state where the transition from volume contraction to dilatancy occurs along a certain stress path. The characteristic stress state, formally discussed as zero dilatancy state by Rowe (1962, 1971) and revisited by Luong (1982), takes place in the early strain regime and therefore it is easier measured in the laboratory in comparison to the critical state. In figure 2.2a characteristic stress states can be observed in all three stress paths. By calculation as shown in Table2.2 for all three paths, the deviation between the highest and the lowest mobilized angle of internal friction measured at CSS is found to be 15% (normalized by the measured average value) while this deviation increases up to 25% for the peak states of stress ratio. This observation suggests that characteristic stress state is more reliable to interpret triaxial compression strength in terms of the angle of internal friction than the peak state of stress ratio. This is so because pure transient friction takes place while a coupled mechanism of friction and dilatancy is at play at the state of peak stress ratio.

Table 2.2 Comparison of measured angles of internal friction at two characteristic states

Stress path	Test No.	q_{css}(kPa)	p_{css}(kPa)	η_{css}	φ_{css}(°) *	η_{peak}	φ_{peak}(°) *
CTC	mf1	343	263	1.30	32.3	1.42	35.0
	mf2a	969	723	1.34	33.2	1.42	35.0
	df1	351	263	1.33	33.0	1.45	35.7
	df4(quick)	801	668	1.20	30.0	1.50	36.8
PTC	mf5	207	154	1.34	33.2	1.55	38.0
	mf6	505	406	1.24	30.9	-----	-----
	df3	194	151	1.28	31.8	1.54	37.8
	df6(quick)	490	409	1.20	31.8	1.63	40.0
RTC	mf3	98	86	1.13	28.3	1.61	39.4
	mf4	269	225	1.19	29.7	1.50	36.8
			Average	1.26	31.4	1.51	37.2

* $\varphi = \arcsin(3\eta/(6+\eta))$

The independence of CSS on the stress paths in terms of stress ratio q/p' is generally accepted (figure2.2).The representation of CSS in the semi-logarithmic compression plane (i.e. $ln(p')$ versus void ratio) exhibits scatter because of the dependence of CSS on the initial void ratios of samples, shown in figure 2.3. Moreover, the isotropic compression lines (ICL) for samples of variable initial densities are almost parallel, and the slopes of ICL are determined. On these ICL, a pre-consolidation pressure P_c defined as the maximum pressure experienced by soil during the laboratory reconstitution history, is the starting point of the ″normally″ isotropic compression line (NICL). It will influence the laboratory properties of soil and its descriptions in mathematical model. A reconstitution and remoulding procedure of sample preparation suggested by Tatsuoka (1982) was employed, and P_c is estimated as 40 kPa and 45 kPa for the medium dense and dense samples, respectively. Further study of the representation of CSS and ICL is important for better understanding the volume change behaviour of sands.

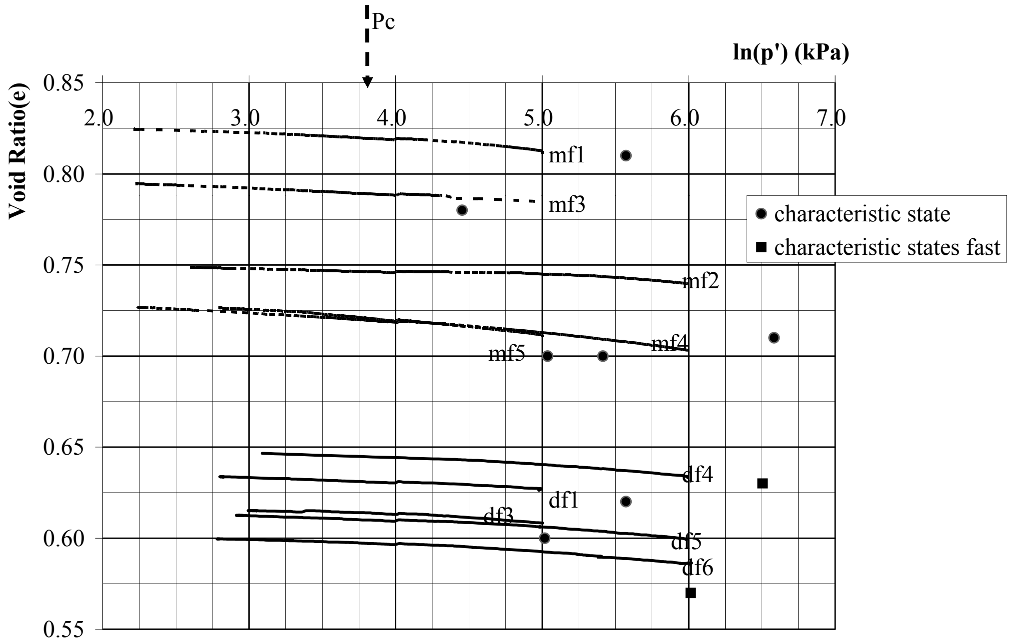

Fig. 2.3 Isotropic compression lines and characteristic stress states

2.2.5 Study of recorded complex deformation modes of cylindrical samples

Under more or less similar boundary conditions, test results (figure 2.4) show variable failure patterns, induced by three stress paths. The initial state of the sample with respect to its lubricated end platens permits some uniform deformation up to an axial strain level of around 5% to 8%. Once the sample has used up its allowance of free sliding on the platens, the non-uniform deformation takes place. But the final failure pattern of the sample depends on the stress path as followed. Precisely speaking the major difference among the three stress paths is the mean stress level induced in the sample. Barreling and bulging with shear bands were observed in RTC and PTC tests on dense sand, respectively, while a mode of axial-symmetric shear bands on the surface of sample was seen in a CTC test at a higher confining pressure. The inclination of one shear band at the centre of the sample with respect to vertical direction was measured as 60 degrees.

a (RTC) b (PTC) c (CTC) d (indentation)

Fig. 2.4 Deformation modes in rountine triaxial compression tests

Boundary conditions for a sand sample induced by a setup for RDTC tests are of primary concern. The influences of friction on top and bottom platens and membrane penetration have been extensively studied, but the effect of indentation of end plates into sample and membrane localization when the lateral deformation extends outside the platens, has not in case of a radial flexible boundary. Because of technical requirements of the laboratory test cell the size of loading platens on the top and bottom are almost the same as the sample. Therefore, such an indentation effect as shown in the figure 2.4 is common in a RDTC test. That is the reason why larger end platens have been used for experimental research purposes. For seeking further evidence on deformation mode of sample affected by such an effect in triaxial cell, a group of indentation tests were carried out on the saturated E.S. Sand contained in a glass vessel (8cm diameter) on one side of the setup (called communicating vessels shown in figure 2.5c). A sponge ring with a thickness of 2cm was placed in this vessel to envelope the sand, allowing the cylindrical sand sample to deform in the radial direction. Indentation of a 2cm-diameter circle disk caused an immediate occurrence of radial dark or light bands. In the light bands moisture content has decreased while moisture content remains in the dark bands. After having lowered the vessel on the other side of the setup, capillarity occurred in the top layer of the sand after some time. The corresponding radial bands can be seen as darker areas (figure 2.5b). This phenomenon is not observed in case of absence of the sponge ring, where the sand sample cannot deform horizontally (figure 2.5a). It is imagined that the part of a sample right underneath the loading platen is kept in a cone shape. A deformation mechanism of cone- radial loosening bands of different densities is most likely to happen as a result of induced boundary conditions. Convincing experimental evidence for the proposed deformation mechanism in a cylindrical sand sample is found in the pictures presented by Desrues et al. (1996), showing the evolution of density distribution in a triaxial compression test of dense sand. Radial bands were clearly exposed with a CT Scanner.

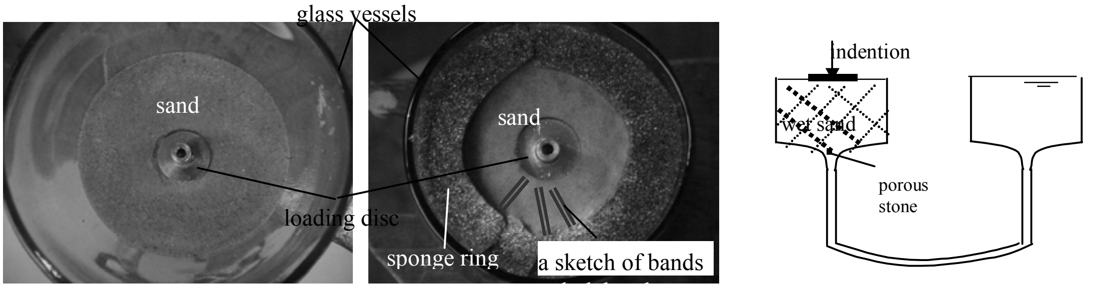

(a) no radial loosening bands (b) radial loosening bands (c) communication vessel setup

Fig.2.5 A setup for visualization of possible deformation mechanism in triaxial compression.

2.3. Development and validation of an advanced elasto-plastic model for modelling the volume change behaviour of sand

This chapter reflects an advance on Desai′ basic elasto-plastic constitutive model, in which the outcome of the previously described laboratory findings is incorporated.

2.3.1. Introduction of characteristic stress state and critical state lines to the Desai δ_0 Model

The yield or plastic flow surface described by Desai's basic model (so called δ_0 Model) in terms of stress invariants is expressed by

$$f_D = \frac{J_2}{p_a^2} - F_a F_b = 0 \tag{2.7}$$

in which,

$$F_a = \left[-\alpha \left(\frac{I_1 + R}{p_a}\right)^n + \gamma \left(\frac{I_1 + R}{p_a}\right)^2 \right];$$

$$F_b = (1 - \beta \cos 3\theta)^{-1/2};$$

$$\cos 3\theta = \frac{3\sqrt{3}}{2} \frac{J_3}{J_2^{3/2}};$$

Here, θ is the Lode angle; α is a hardening function; β, γ, and n are material parameters; P_a is the atmospheric pressure; R is the triaxial tensile strength.

For triaxial element behaviour of sand, a simplified mathematical expression can be obtained in terms of deviator stress q and effective mean stress p' by disregarding the effects of Lode angle and triaxial tensile strength of sand, Substituting $\cos 3\theta = 1$, β=0, R=0, $q^2 = 3J_2$ and $p' = I_1/3$ into equation (2.7) results in

$$\frac{q^2}{3p_a^2} = -\alpha\left(\frac{3p'}{p_a}\right)^n + \gamma\left(\frac{3p'}{p_a}\right)^2 \tag{2.8}$$

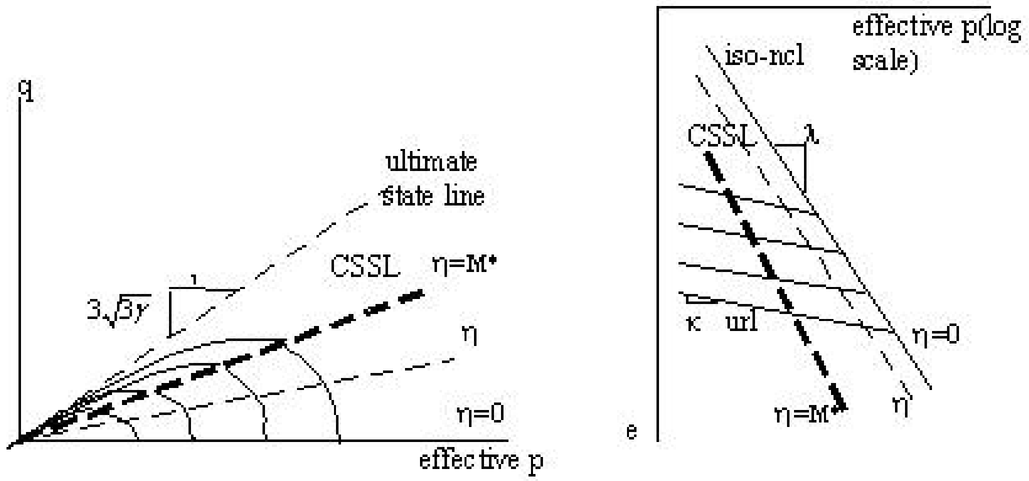

(a) Relationship of Desai yield loci with CSSL in q-p′ plan (b) Relationship of iso-ncl and CSSL in the compression plan

Fig. 2.6 Introduction of CSSL into Desai basic mode

Next, the characteristic stress state line (CSSL) is introduced in this model. The stress ratio of characteristic stress state is a material constant M^*. The yield loci and their correlations with characteristic stress states are shown in figure 2.6a Three assumptions are made for reconstituted saturated sand in the e-log(p′) compression plane. Firstly, the CSSL exists uniquely; Secondly, each yield locus is associated with an unloading-reloading line, denoted as url, in the compression plane which has its tip at $p' = p_0'$ on the isotropic normal compression line, denoted as iso-ncl; Thirdly, both the isotropic normal compression line and unloading-reloading line are straight in semi-logarithmic compression plane. The second assumption is far away from laboratory facts illustrated in figure 2.6b. It can be corrected by assuming a different type of hardening function (see following section). Most of the tests described in the following section, for which an elastic-plastic model, Desai model, is used to predict the response, experienced two transformation states, the characteristic stress and peak states, and eventually an critical state. The condition of perfect plasticity, where plastic shearing could continue indefinitely without changes in effective stresses and volume is referred to as critical state, which can be expressed by equation.2.9 and an effective stress ratio (equation 2.10). These critical states are assumed to be unique for a kind of reconstituted and remoulded soil, i.e. critical state line with a slope of *M* is unique in q/p' plane, provided relatively large plastic deformations are occurring. It should be noticed that M and M^* are not necessarily identical.

$$\frac{\partial p'}{\partial \varepsilon_q} = \frac{\partial q}{\partial \varepsilon_q} = \frac{\partial v}{\partial \varepsilon_q} = 0 \tag{2.9}$$

$$\frac{q_{cs}}{p'_{cs}} = \eta_{cs} = M \tag{2.10}$$

2.3.2. Procedure for development and calibration of the advanced Desaiδ_0 model using triaxial tests

Strain softening in triaxial tests on sand is a challenging topic. A distinction is to be made for the characteristic stress state and peak moments between the strain hardening and strain softening phases. Dilatancy may take place in the strain-hardening regime. The prerequisite for better understanding strain softening of sand is a study of the dilatancy behaviour of sand in the strain-hardening phase. The strain hardening response is therefore of concern in the present study.

(1) Parameter γ

The slope of the ultimate response line (figure 2.6) is controlled by parameter γ. This parameter is related to the peak stress ratio M' of the sand. It is a state parameter rather than a material constant as it may vary with M'

$$\gamma = \frac{(M')^2}{27} \quad \text{, for } \alpha=0 \tag{2.11}$$

(2) Parameter *n*

The dilation behaviour is associated with parameter n. According to the relationship shown in the figure 2.6a, all tangents of yield loci at the intersections with the CSSL vanish, i.e. zero-dilatancy condition. By applying this condition to equation 2.8 *n* has to be chosen according to equation 2.12. It may not be a material constant, but a state parameter as it varies with M' of sand.

$$n = \frac{2}{1-\left(\frac{M^*}{M'}\right)^2} \tag{2.12}$$

The peak strength of sand in terms of stress ratio has been extensively studied in the past and Rowe's stress-dilatancy equation is generally accepted as the most appropriate prediction of peak strength. Several empirical correlations with some state parameters, such as relative density, mean pressure etc., are reported (Bolton et al., 1986). Rowe's stress-dilatancy equation for conditions of triaxial compression is employed to estimate the peak stress ratio M' as shown in equation 2.13 and 2.14 (Wood, 1990).

$$\psi = \frac{9(M^* - \eta)}{9 + 3M^* - 2M^*\eta} \tag{2.13}$$

The M' of peak strength can be obtained, provided the maximum dilatancy ψ_{max} appears almost at the peak moment of strength.

$$M' = \frac{9M^* - 9\psi_{\max} - 3M^*\psi_{\max}}{9 - 2M^*\psi_{\max}} \tag{2.14}$$

To obtain the maximum dilatancy an empirical relation of dilatancy, defined as $\psi = \frac{d\varepsilon_v}{d\varepsilon_a}$ with initial relative density Dr and consolidation pressure, has to be deduced from test data.

<u>(3) Hardening function α</u>

The function α is a measure of the size of the yield surface, and is a decreasing function with regard to the equivalent plastic strain. Several mathematical functions are found to be admissible for α, but physical mechanism should be considered. The dependency of α on stress and strain paths is inevitable for sand because of the incomplete understanding of dilatancy-hardening behavior of sand. The following two functions for α derived from two stress paths in the laboratory are used to further explain this dependency.

$$\alpha(\xi) = \frac{\alpha_0 - \xi_{\lim}\xi}{1 + a\xi} \tag{2.15a}$$

in which $\xi = \int (d\varepsilon_{ij}^p \, d\varepsilon_{ij}^p)^{1/2}$ is the equivalent plastic strain trajectory; ξ_{lim} is the peak plastic strain; α_0 is the elastic limit; a is a regression coefficient. Equation 2.15a represents a curve fit for uniaxial compression test data for concrete (Scarpas et al., 1998), and Equation 2.15b is derived by fitting isotropic compression test data of E.S. Sand using the assumption of linear relationship of $\ln p'$ with volume change.

$$\alpha(\xi_v) = \gamma \left(\frac{3p_c}{p_a}\right)^{2-n} e^{-\frac{(1+e_c)(n-2)}{\lambda-\kappa}\xi_v} \tag{2.15b}$$

in which λ is the slope of normal compression line in semi-log compression plane; κ is the slope of unloading-reloading line in semi-log compression plane; p_c is the pre-consolidation pressure; p_a is the atmospheric pressure; e_c is the initial void ratio; ξ_v is the volume-related plastic strain or work. Equation 2.15a is not suited to correctly estimate the volume change in sand. Equation 2.15b does not account for dilatancy, if ξ_v is only related to the volume change during isotropic loading. An improved mathematical form for α with a reasonable physical motivation is required to predict proper dilatancy, if associated flow is invoked.

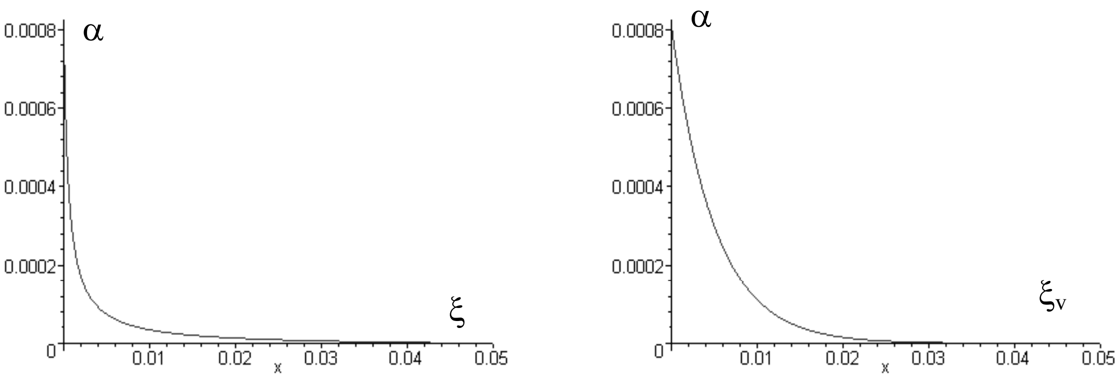

$$\alpha(\xi) = \frac{0.0162 \times (0.05 - \xi)}{1 + 1792\xi} \qquad \alpha(\xi_v) = 0.0162 e^{-(1792\xi_v + 2.99)}$$

Fig. 2.7 Two mathematical expressions for hardening function

The two expressions are graphically shown in the figure 2.7. The parameters involved are determined from Test Df1. The functions control the isotropic hardening rate of yield loci in different ways as can been seen in this graph. Though the physical basis is not clear yet, expression 2.15a is used for the following modeling on basis of Desai yield surface, with the parameters as follows.

$$a = \frac{(1+e_0)(n-2)}{\lambda - \kappa}; \qquad \alpha_0 = \gamma \left(\frac{3p_c}{p_a} \right)^{2-n}; \qquad \xi_{\lim} = \left(\frac{p_c}{p_0}\right)^{n-2} \qquad (2.15c)$$

in which, p_0 is the consolidation pressure; e_0 is the void ratio after consolidation. Except for an empirical procedure for the maximum dilatancy angle ψ_{max} all other parameters can be evaluated from test data (Appendix of Chapter 2) according to the procedure mentioned above. The result for several tests is summarized in Table2.3.

Table2.3 Parameters of Desai δ_0 model for E.S.Sand (evaluated by 12 tests)

Parameters	Values	Description	Equations or figures
M^*	1.37	Slope of CSSL	Fig 2.6a
λ	0.0055	Slope of normal compression line	Fig 2.6b
κ	0.0025	Slope of unloading-reloading line	Fig. 2.6b
n	4~12	Dilatancy parameter	Equation 2.12
γ	0.09~0.12	Peak strength-related parameter	Equation 2.11
α_0	0.001~0.01	Elastic limit	Equation 2.15

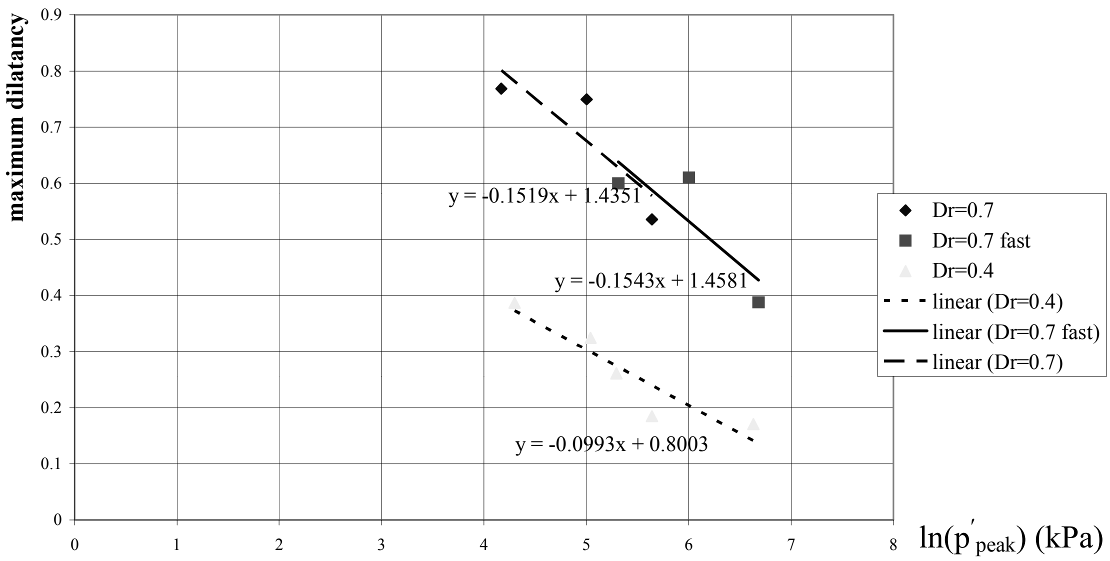

Fig. 2.8 Maximum dilatancy against logarithm of peak mean stress

(4) A regression procedure to determine the maximum dilatancy

An empirical relation for the determination of the ultimate state of sand is suggested (Bolton 1986) treating the peak stress ratio of sand denoted by M' as a state parameter instead of material constant. The fitting process can be seen in the figures 2.8. The maximum dilatancy is expressed by equation 2.16 in terms of initial relative density D_r and effective peak mean stress P'_{peak}.

$$\psi_{\max} = (-0.2Dr - 0.03)\ln P'_{peak} + 2Dr - 0.05 \tag{2.16}$$

2.3.3 Comparison of model prediction and laboratory test results

The stress-strain behaviour of sand in triaxial tests can be predicted by the suggested elastic-plastic model. The program Driver implementing constitutive Desai δ_0 model was employed to predict the hardening response. A comparison between model predictions and laboratory tests is made to validate the calibration procedure and model behaviour. Parameters used in numerical calculations are listed in Table2.3, where n, γ and α_0 are chosen as 8, 0.1 and 0.0015 respectively. As Driver can only simulate CTC behaviour of material, the deformation predictions for the other stress path are not available. For a CTC test as shown in figure 2.9a, the model prediction on CSS in terms of stress is in fair agreement with a measured value represented by an open circle in the picture. A clear yield surface of elastic limit appears and its position in relation to the one at the end of consolidation is quite convincing. However, the predicted volume change in the hardening regime is much larger than the measured values, both for contraction and dilatancy, as shown in figure 2.9b. The application of the associated flow rule in the model for sand has to be blamed for this. After applying a potential surface different from yield surface the prediction of the volume change is improved for a CTC test.

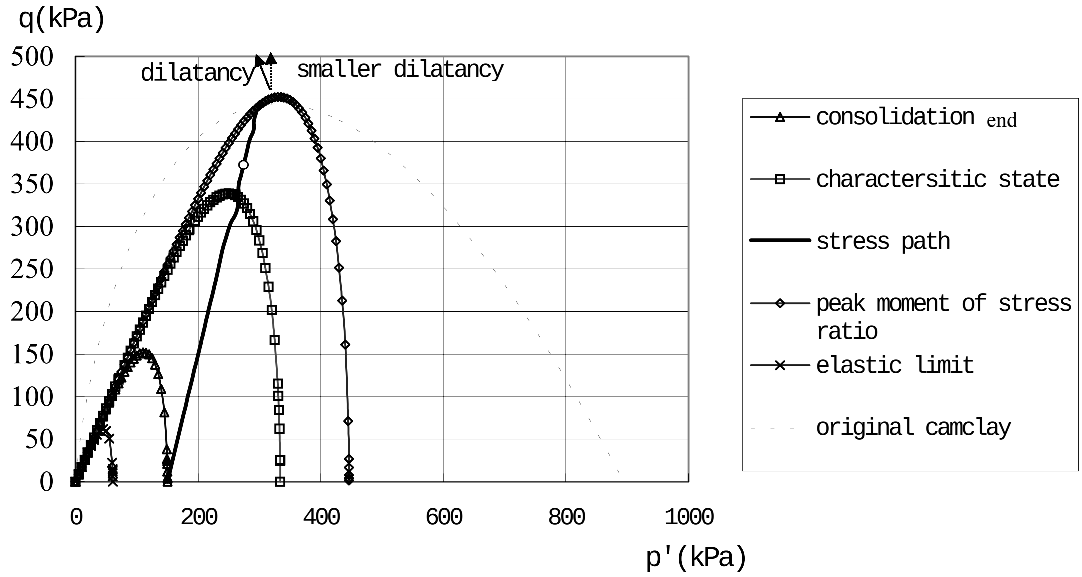

Fig. 2.9a Desai yield or plastic potential surfaces corresponding to variable states for E.S.Sand in CTC test.

(The open circles represent characteristic stress states measured in the laboratory)

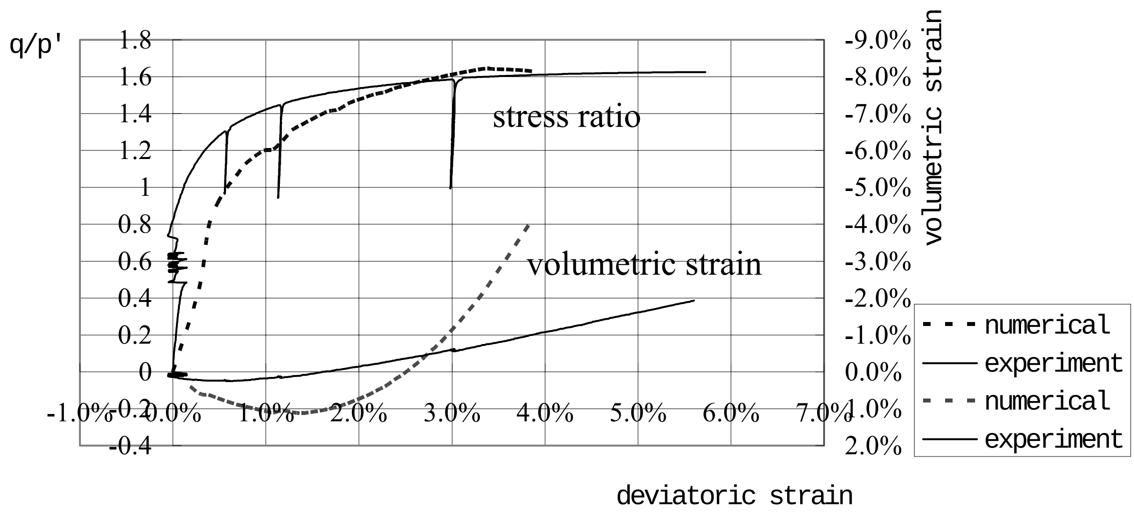

Fig. 2.9b Comparision of numerical predicitions and experimental results for a CTC test.

Although an advanced model is capable of modelling a CTC test better, it will give only elastic deformation for a RTC test for a consolidation pressure of 150 kPa, as shown in figure 2.9c, if the mean stress is reduced to 70 kPa. This obviously contradicts the laboratory facts, because extreme plasticity, nearing failure, occurred immediately along this RTC path. The model could be improved, if a yield surface at elastic limit is considered for RTC path. A comparison in figure 2.9d reveals that the model can capture the characteristic stress state for PTC very well.

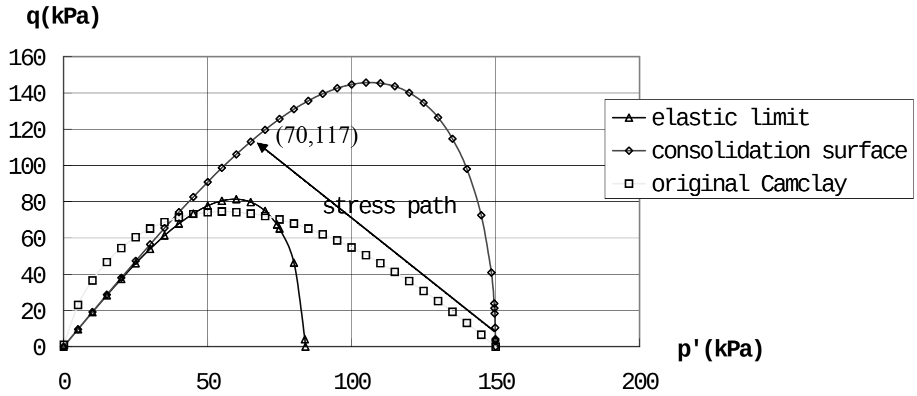

Fig. 2.9c Desai Yield or plastic potential surfaces for RTC tests

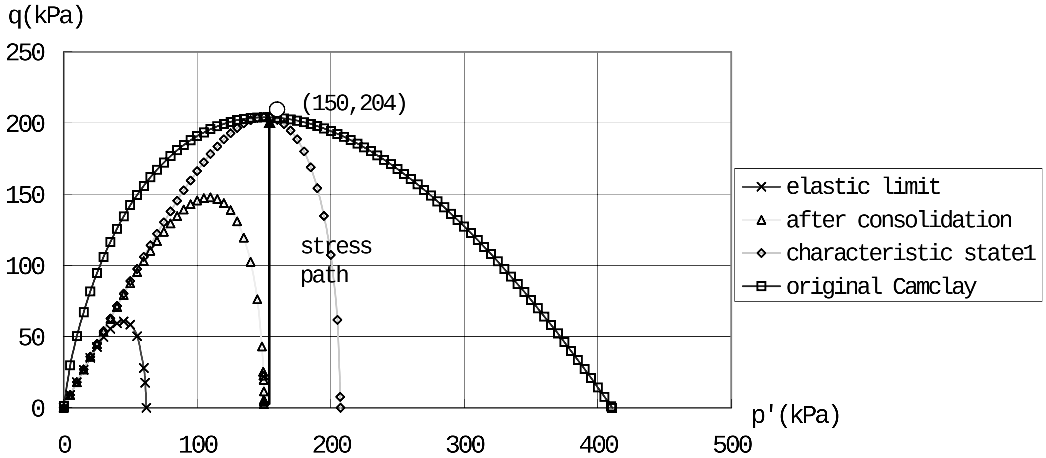

Fig. 2.9d Desai yield surface for PTC tests

2.4. Summary of difficulties in interpretation of RDTC Test

Deformation modes of sand samples in triaxial compression test are quite variable. Mean stress levels and boundary conditions are the main causes of these different modes. Based on RDTC tests a hitherto unrecognized deformation mode (Desrues et al, 1996), cone-radial bands of varying density, has been observed. The characteristic stress state is a precursor of the formation of such a deformation mode. Once such an intermixing deformation mode occurs the measured strength, either peak or post-peak strength, is difficult to interpret and it may have lead to incorrect interpretations of laboratory data in the past. Triaxial laboratory test results, particularly deformation mechanism and volume change, should be interpreted differently. A single deformation mechanism when interpreting laboratory findings is not sufficient.

Besides the generally accepted shear-dilatancy mechanism, another one named the mechanism of cone-radial loosening bands is suggested. Such loosening bands have actually been recognized as cracks in cohesive materials such as concrete or fissures in rocks and stiff clays. With the cone-radial loosening bands mechanism the difficulties in interpretation are more or less solved, and the understanding of liquefaction and dilatancy captured in laboratory can be improved. For that purpose, the elasto-plasticity theory has been used to better interpret laboratory tests with regard to triaxial strength and dilatancy (Chapter 3).

Appendix of Chapter 2

Laboratory data of RDTC Tests

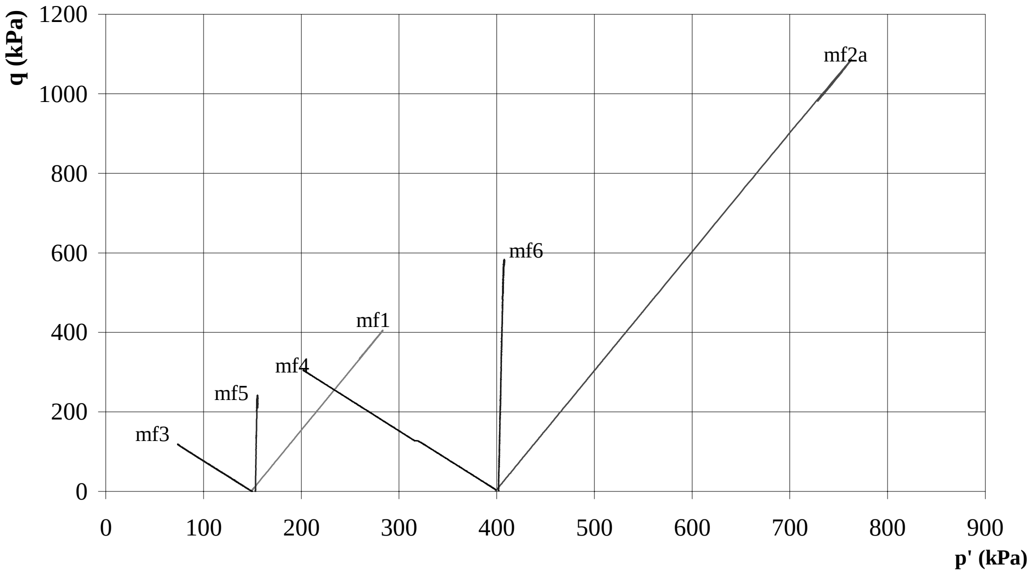

Fig. A2.1 Tests and stress paths involved for the medium dense samples

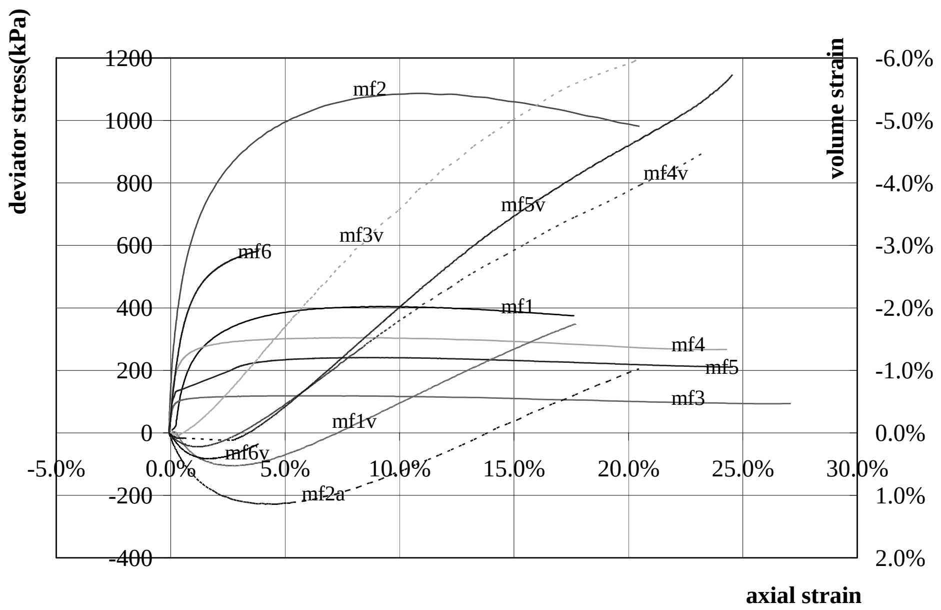

Fig. A2.2 Deviator stress and volume strain versus axial strain for the medium dense samples

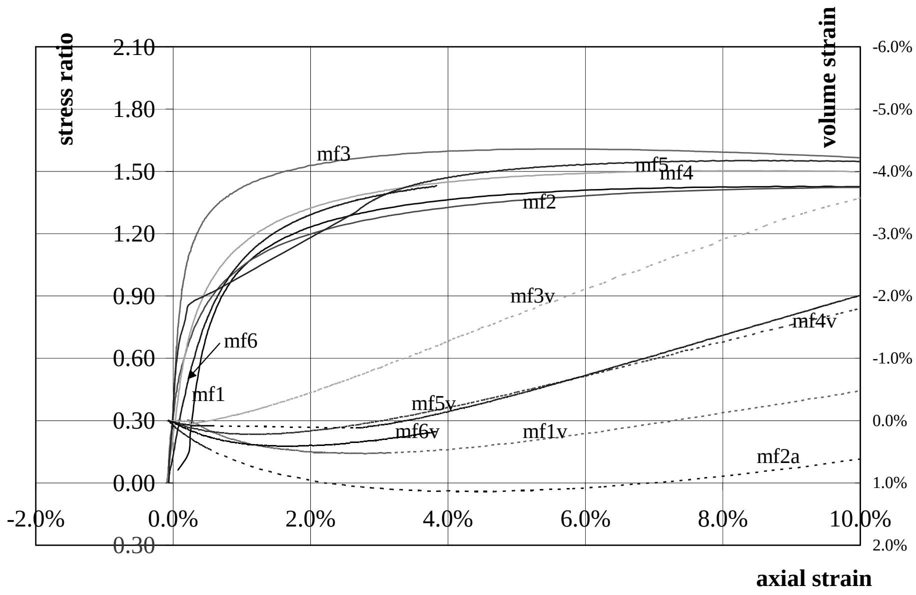

Fig. A2.3 Stress ratio and volume strain versus axial strain for the medium dense samples

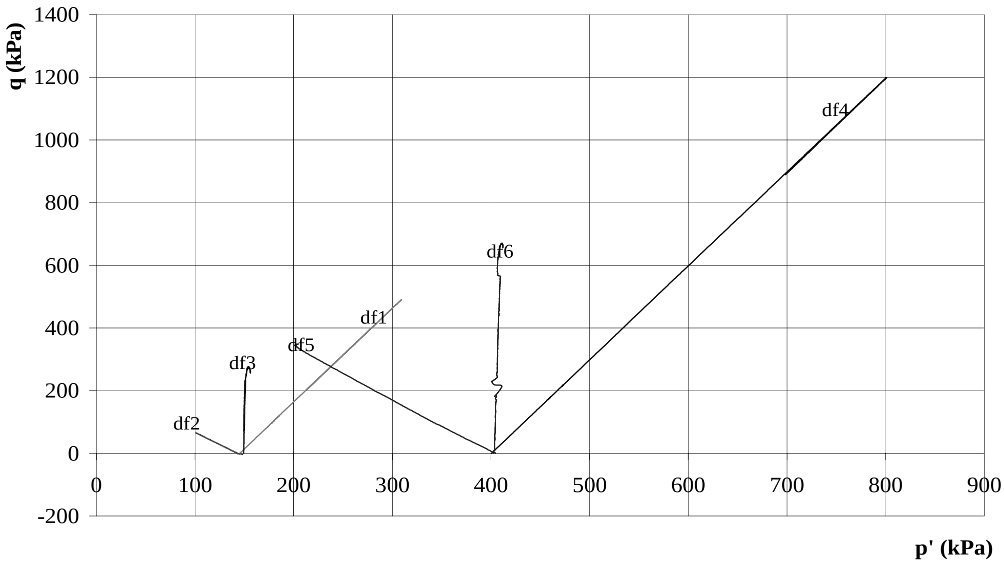

Fig. A2.4 Tests and stress paths involved for the dense samples

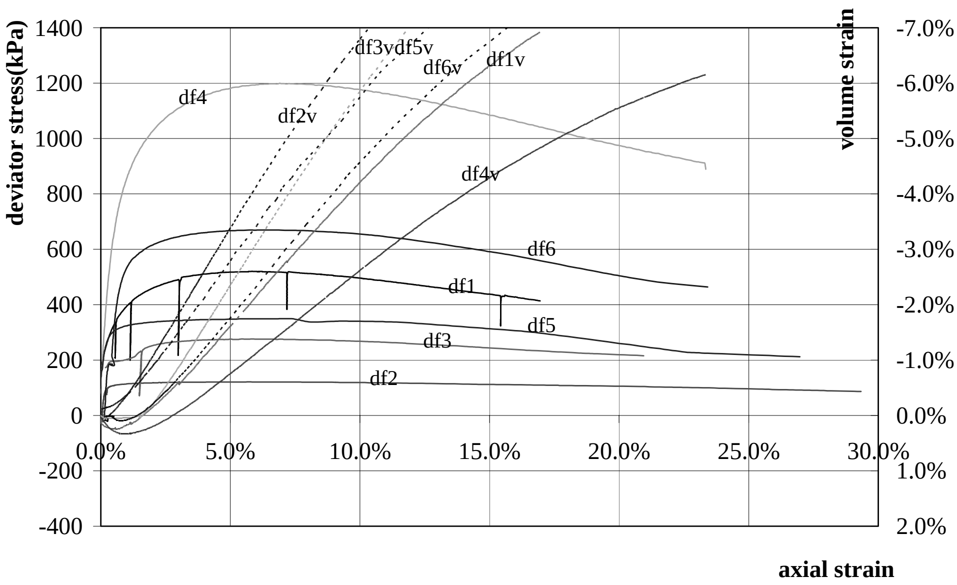

Fig. A2.5 Deviator stress and volume strain versus axial strain for the dense samples

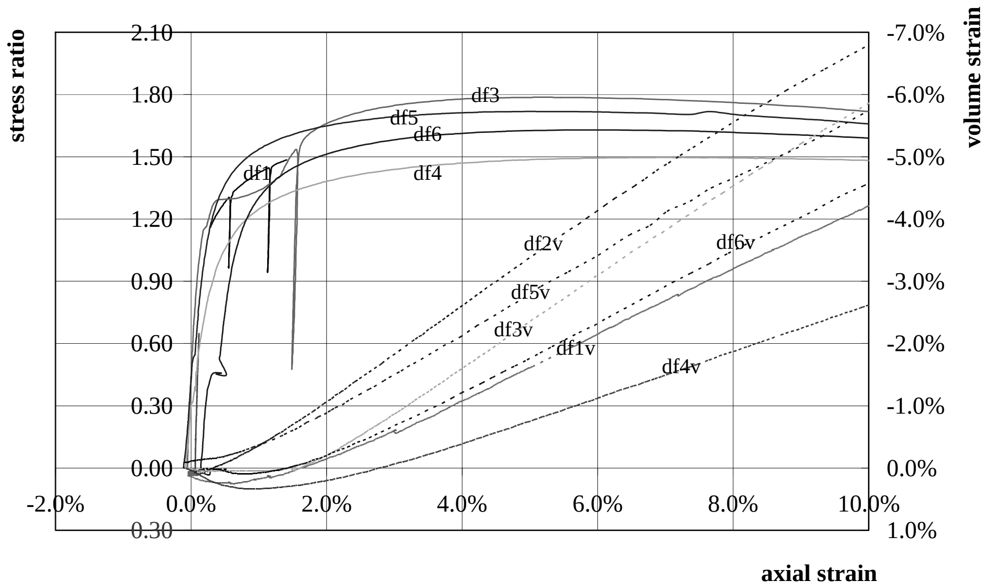

Fig. A2.6 Stress ratio and volume strain versus axial strain for the dense samples

Chapter 3

Limit Analysis (Upper Bound Solutions) of Failure Mechanism of a Cylindrical Sand Sample

3.1 Introduction

A theoretical approach using the technique of limit analysis is applied to formulate the cone-radial loosening band deformation mode (Desrues et al, 1996). Two failure mechanisms are involved, i.e. a single shear rupture plane and double cones-radial loosening bands. Both associated kinematical field and non-associated kinematical field are considered. The Mohr-Coulomb yield criterion is applied. The classical mechanism of energy dissipation in a shear rupture is applied. Upper bound solutions, i.e. extreme values of an analytic function in a certain domain, are obtained in the present study. Finally, the orientation of shear-rupture surfaces (cones) in a cylindrical sample is formulated in terms of apparent friction angle, apparent dilatancy angle slenderness of the sample, confining pressure and tensile strength.

3.2 Mohr-Coulomb material at limit state

Sand at the limit state is assumed to be a Mohr-Coulomb material with a cohesion and friction angle as shown in figure 3.1. The tensile strength f_t comes from the apparent cohesion of an assembly of wet sand particles with a desired density. σ_0 and q_c are confining pressure and deviator stress at limit state, respectively.

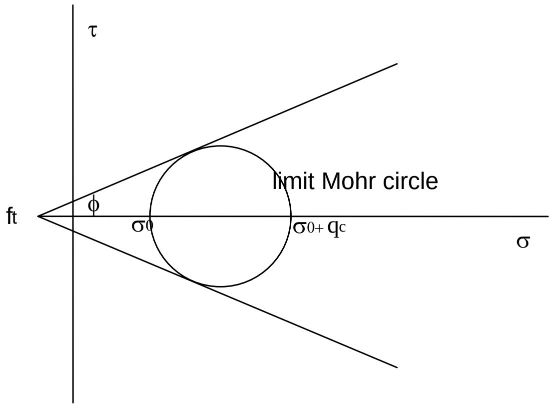

Fig.3.1. Limit state of material

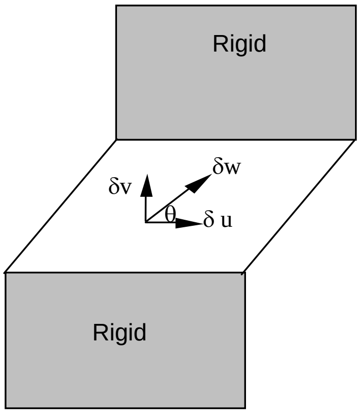

Fig.3.2. Mechanism of energy dissipation

3.3. Calculation of energy dissipation in rupture-shear planes or loosening bands

A classical mechanism of energy dissipation in rupture-shear planes in limit analysis has been defined by Chen (1975) for concrete (figure 3.2). The increment of dissipation of energy per unit area of discontinuity is (see figure 3.2):

$$D = \tau\delta u - \sigma\delta v = \delta u(\tau - \sigma\tan\theta) \qquad (3.1a)$$

The jump in tangential velocity across the discontinuity is denoted by δu, the separation velocity by δv=δu tanθ, and the relative velocity vector δw is at an angle of $\theta \leq \varphi$ to the discontinuity surface.

Two particular cases, simple tensile crack (with the tensile strength of f_t,) and simple sliding for which $\theta = \pi/2$ (δu=0 also implied) and $\theta = \varphi$, respectively, can be obtained as failure mechanism by substituting $\tau_c = (q_c\cos\varphi)/2$ and $\sigma = q_c(1\text{-}\sin\varphi)/2 + \sigma_0$ into equation (3.1a), as shown in equation (3.1b) and (3.1c).

$$D = f_t\delta v \quad \text{for a single crack} \qquad (3.1b)$$

$$D = (q_c\frac{1-\sin\varphi}{2} - \sigma_0\sin\varphi)\delta w \quad \text{for a single sliding} \qquad (3.1c)$$

3.4. Upper bound solutions for a material with perfect plasticity ($\theta = \varphi = \psi$)

3.4.1 Mechanism of a single shear plane

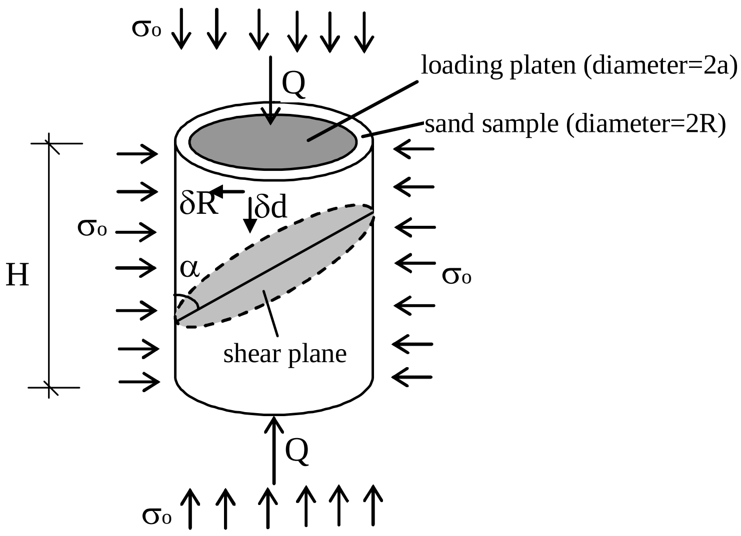

Fig.3.3. Failure mechanism of a single shear plane

Figure 3.3 shows the virtual velocities of upper rigid part of a sample with respect to the lower part adjacent to a single shear plane are δd in the vertical direction and δR in the horizontal direction. Their relations with the relative velocity of the rupture surface δw are elaborated in figure 3.4c.

The rate of dissipation energy across the entire shear plane is:

$$(q_c \frac{1-\sin\varphi}{2} - \sigma_0 \sin\varphi)\delta w \frac{\pi R^2}{\sin\alpha} \tag{3.2a}$$

The rate of external work is:

$$Q\delta d + \sigma_0 \pi R^2 \delta d - \sigma_0 \pi R^2 ctg\alpha \delta R \tag{3.2b}$$

where Q is the vertical loading force.

The last part in the equation (3.2b) describes the virtual work done by the confining pressure of σ_0 on the upper part of the sample. It can be derived according to the following integral:

$$-2\int_0^{\pi} \sigma_0 \cdot R\delta\omega \cdot 2R \cdot ctg\alpha \cdot (1+\cos\omega)/2 \cdot \cos\omega \cdot \delta R = -\sigma_0 \pi R^2 ctg\alpha \delta R \tag{3.2c}$$

where ω is the integral variable.

Equating the rate of external work to the rate of dissipation energy gives the expression of Q as a function of the inclination of shear plane, α

$$\frac{Q}{\pi R^2} = \frac{q_c(1-\sin\varphi) - 2\sigma_0 \sin\varphi}{2\sin\alpha\cos(\alpha+\varphi)} + \sigma_0 \tan(\alpha+\varphi)ctg\alpha - \sigma_0$$
$$= \frac{1-\sin\varphi}{2\sin\alpha\cos(\alpha+\varphi)} q_c \qquad (3.2d)$$

Minimization of Q in the equation (3.2d) will yield that the inclination angle α of shear plane is $\pi/4$-$\varphi/2$ (Coulomb solution). If such a mechanism exists the slenderness of sample has to be larger than 1/tan($\pi/4$-$\varphi/2$). And the independence of the inclination of shear plane on the confining pressure and tensile strength is obvious.

3.4.2 Mechanism of double-cone-loosening bands

An ideal failure mechanism for a tri-axial compression test on a cylindrical sand specimen is shown in figure 3.4a. It consists of many single loosening bands along the radial direction and two cone-shaped rupture surfaces (sliding) directly in contact with the loading platens. A compatible velocity field can be described as the cones move towards each other as a rigid body and push away the surrounding material horizontally. The velocity field is shown in figure 3.4b, where the relative velocity δw along the cone rupture surface is inclined at an angle φ to the surface. The corresponding areas of two kinds of discontinuities (cones and loosening bands) and the corresponding velocities are calculated in figure 3.4c.

The rate of dissipating energy across all discontinuity surfaces is:

$$2(q_c \frac{1-\sin\varphi}{2} - \sigma_0 \sin\varphi)\frac{\pi a^2}{\sin\alpha}\delta w + 2 f_t \pi (RH - a^2 ctg\alpha)\delta R \qquad (3.3a)$$

The rate of external work is

$$2Q\delta d + 2\sigma_0 \pi R^2 \delta d - 2\sigma_0 \pi RH\delta R \qquad (3.3b)$$

Equivalence of the external rate of work and the rate of internal energy dissipation leads to an expression for Q in terms of φ and α:

$$\frac{Q}{\pi a^2} = \frac{(1-\sin\varphi)q_c}{2\cos(\alpha+\varphi)\sin\alpha} + \tan(\alpha+\varphi)(\frac{RH}{a^2} - ctg\alpha) f_t - \frac{\sigma_0 \sin\varphi}{\cos(\alpha+\varphi)\sin\alpha} +$$
$$\tan(\alpha+\varphi)\frac{RH}{a^2}\sigma_0 - \frac{R^2}{a^2}\sigma_0 \qquad (3.3c)$$

The following relationship will be obtained from the figure 3.1

$$2\sigma_0 \sin\varphi - (1-\sin\varphi)q_c = -2 f_t \sin\varphi \qquad (3.3d)$$

Here, α is the unknown angle of the cone.

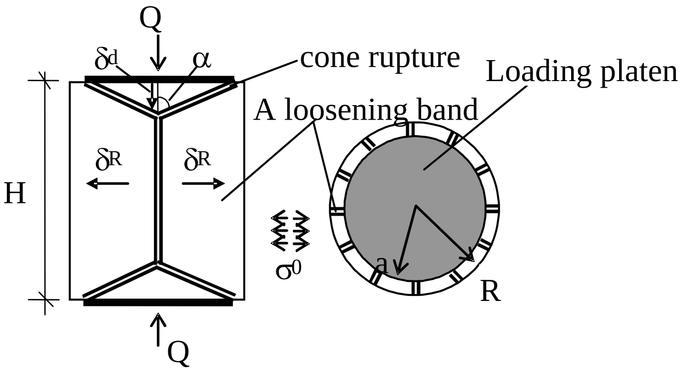

(a) section of a loosening band and top view of sample

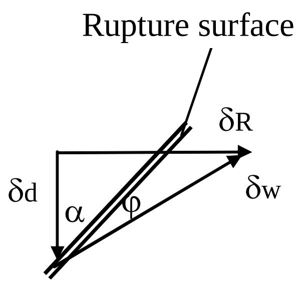

$$\delta d=\delta w\bullet\cos(\alpha+\varphi)$$
$$\delta R=\delta w\bullet\sin(\alpha+\varphi)$$

(b) relation of relative velocities

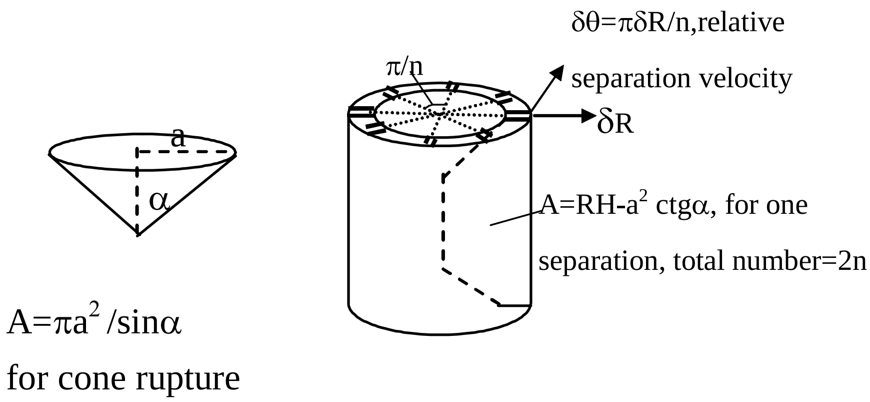

(c) areas of two kinds of discontinuities

Fig.3.4. Mechanism of double cones-loosening bands

An upper bound value for external load is formed when α satisfies the condition of $\partial Q / \partial \alpha = 0$, which gives the following equation (3.4) in terms of variable α:

$$-2 f_t \sin\varphi \cos(2\alpha + \varphi) + B\sin^2\alpha + f_t[\sin(2\alpha + 2\varphi) - \sin 2\alpha] = 0 \tag{3.4}$$

in which, $B = 2(RHf_t + RH\sigma_0)/a^2$

The equation (3.4) holds, if α is zero or $\pi/2$. So this mechanism is no longer valid in terms of cone shape .

3.5. Upper bound solutions for a material with non-associated plasticity

Concerning limit analysis applied to a non-associated plasticity material, substitution of $\theta = \psi < \varphi$ into equation (3.1) yields equation (3.5), which represents the mechanism of energy dissipation for non-associated plasticity material.

$D = f_t \delta v$ for a single loosening band (3.5a)

$D = [\frac{q_c \cos(\varphi - \psi)}{2} - \frac{q_c \sin\psi}{2} - \sigma_0 \sin\psi]\delta w$ for a single shear-rupture surface (3.5b)

3.5.1 Mechanism of a single shear plane

In case of the mechanism of a single shear plane, equating the rate of external work to the rate of dissipation energy gives the expression of Q as a function of the inclination of shear plane, α:

$$\frac{Q}{\pi R^2} = \frac{C + \sigma_0 \cos\alpha \sin(\alpha + \psi)}{\sin\alpha \cos(\alpha + \psi)} - \sigma_0 \tag{3.6}$$

in which $C = q_c \cos(\varphi - \psi)/2 - q_c \sin\psi/2 - \sigma_0 \sin\psi$

Minimization of Q in the equation (3.6) yields the inclination angle α of shear plane is $\pi/4-\psi/2$ (Roscoe solution). If such a mechanism exists the slenderness of sample has to be larger than $1/\tan(\pi/4-\psi/2)$.

3.5.2 Mechanism of double-cone-loosening bands

In case of the mechanism of double-cone-loosening bands, equating the rate of external work to the rate of dissipation energy can give the expression of Q as a function of the inclination of shear plane, α. Minimization of Q leads to the following relationship:

$$-2C\cos(2\alpha + \psi) + B\sin^2\alpha + f_t[\sin(2\alpha + 2\psi) - \sin 2\alpha] = 0 \tag{3.7a}$$

in which $B = 2(RHf_t + RH\sigma_0)/a^2$, $C = q_c \cos(\varphi - \psi)/2 - q_c \sin\psi/2 - \sigma_0 \sin\psi$

The inclination of shear planes, α satisfying equation (3.7a) can be found in the appendix, according to the equation (app. 3.4). It is shown in equations (app 3.4) and (3.3d) that the inclination of shear planes depend on (a) the internal angle of friction, φ, (b) the dilatancy angle, ψ, (c) the sample slenderness, H/R, (d) the ratio of confining pressure to tensile strength, σ_0/f_t and (e) the ratio of loading plate size to sample size, R/a. The influence of the ratio of confining pressure to tensile strength is less significant as far as the following situations are concerned, e.g. $\varphi = 30^0$, $\psi = 10^0$, $H/R = 2$, $R/a = 1$ and $f_t = 10$ kPa. Inclinations of shear plane calculated according to equation (app 3.4) are 23.7^0, 23.4^0 and 24^0, with respect to $\sigma_0 = 150$ kPa, 300kPa and 600 kPa, respectively. Its influence could be significantly increased as the ratio of σ_0/f_t decreases.

Furthermore, two types of non-associate plastic materials are considered as follows to investigate the influence of slenderness. One is the incompressible material which implies ψ=0 (dilatancy angle), and the other is the dilatant material with the dilatancy angle of $\psi=\varphi/2$. Using both these conditions and the equation (3.3d) one can simplify the equation (3.7a) to the following equations (3.7b), (3.7c) and (3.7d). The inclination of cones, α can be obtained.

In case of ψ=0:

$$q_c \cos\varphi \cos 2\alpha = B \sin^2\alpha \tag{3.7b}$$

$$\alpha = \frac{1}{2}\cos^{-1}\left(\frac{1}{1 + a^2 \sin 2\varphi / [RH(1-\sin\varphi)]}\right),\ \alpha \in (0, \pi/2) \tag{3.7c}$$

In case of $\psi=\varphi/2$:

$$-\frac{a^2 \sin\varphi}{RH(1-\sin\varphi)}(\sin\varphi + ctg\varphi - \csc\varphi)\sin 2\alpha + \left(\frac{a^2 \sin\varphi}{RH(1-\sin\varphi)}\cos\varphi + 1\right)\cos 2\alpha = 1,$$
$$\alpha \in (0, \pi/2) \tag{3.7d}$$

Concerning these two types of non-associated materials the equation (3.7) proves that inclinations of cones depend on only the internal angle of friction, φ and the slenderness of samples, H/a.

Table 3.1 gives the calculated inclinations of cones for two non-associated materials aforementioned, if such intermixing deformation mechanism occurs. For the simplicity, let $R=a$ for calculations.

Table 3.1 Predicated inclination of cone

Internal angle of friction, φ (degrees)	Dilatancy angle, ψ (degrees)	Slenderness of sample, H/a	Inclination of cone, α (degrees)
30	0	2	29
30	0	4	23
30	15	2	21
30	15	4	16

Compared to the Coulomb-type ($\pi/4$-$\varphi/2$) and Roscoe-type ($\pi/4$-$\psi/2$) shear bands, predicated cones are sharp in terms of inclinations. In addition, according to the double sliding model (De Josselin de Jong, 1971) inclinations of shear band (or velocity characteristics) are limited by fans whose boundaries deviate by $\varphi/2$ from the bisectrices of the principal stress directions. In case of material presented in Table 3.1 this model implies that non-unique inclinations of shear band for an incompressive elasto-plastic material are within the range of 30^0 to 60^0 with respect to the major principal stress direction, which is due to the non-coaxiality. Admissible shear band inclinations (Vermeer, 1990) means all shear band inclinations within the Roscoe-Coulomb range, i.e. $\pi/4-\varphi/2 \leq \alpha \leq \pi/4-\psi/2$ are possible (other directions are impossible) according to a bifurcation analysis, if the material outside the shear band is allowed to unload elastically.

3.6. Summary

The complex failure deformation patterns in routine drained triaxial compression (RDTC) tests have been formulated in terms of inclination of variable shear rupture surfaces. A theoretical consideration implies that five factors (φ, ψ, H/R, σ_0/f_t and R/a) are responsible for the deformation mechanism. As far as RDTC tests of nearly saturated sand concerned, the two factors of σ_0/f_t and R/a can be disregarded. The theoretical prediction is supported by laboratory observations in the past. Furthermore, the apparent triaxial compression strength of sand as measured in RDTC tests, is related to the sample slenderness. This finding is useful for the interpretation of triaxial compression strength as measured in the laboratory.

Appendix of Chapter 3

Analytical solution of the inclination α for equation (3.7a)

Equation (3.7a) can be rewritten as follows:

$$f_t \cos\psi \sin(2\alpha+\psi) + (f_t \sin\psi - 2C)\cos(2\alpha+\psi) - f_t \sin 2\alpha - B\cos 2\alpha/2 + B/2 = 0 \qquad \text{(app 3.1)}$$

Introduction of intermediate variables β_1 and β_2 to the equation above, leads to:

$$\sqrt{f_t^2 + 4C^2 - 4Cf_t \sin\psi}\,\sin(2\alpha+\psi+\beta_1) - \sqrt{f_t^2 + B^2/4}\,\sin(2\alpha+\beta_2) = -B/2 \qquad \text{(app 3.2)}$$

in which $\sin\beta_1 = (f_t \sin\psi - 2C)/\sqrt{f_t^2 + 4C^2 - 4f_t C\sin\psi}$

$$\cos\beta_1 = f_t \cos\psi / \sqrt{f_t^2 + 4C^2 - 4f_t C\sin\psi}$$

$$\sin\beta_2 = B/\sqrt{4f_t^2 + B^2}$$

$$\cos\beta_2 = f_t/\sqrt{f_t^2 + B^2/4}$$

Let $\beta = \psi+\beta_1-\beta_2$, the following equation can be derived from equation (App. 3.2):

$$\sqrt{f_t^2 + 4C^2 - 4Cf_t \sin\psi}\,\sin(2\alpha+\beta_2+\beta) - \sqrt{f_t^2 + B^2/4}\,\sin(2\alpha+\beta_2) = -B/2 \qquad \text{(app 3.3)}$$

Introduction of one more intermediate variable β_3 to the equation (App 3.3) leads to:

$$\sin(2\alpha+\beta_2+\beta_3) = -\frac{B}{2\sqrt{f_t^2 + 4C^2 - 4Cf_t\sin\psi + f_t^2 + B^2/4 - 2\cos\beta\sqrt{(f_t^2 + 4C^2 - 4f_t C\sin\psi)(f_t^2 + B^2/4)}}} \qquad \text{(app 3.4)}$$

in which

$$\sin\beta_3 = \frac{\sin\beta\sqrt{f_t^2 + 4C^2 - 4Cf_t\sin\psi}}{\sqrt{f_t^2 + 4C^2 - 4Cf_t\sin\psi + f_t^2 + B^2/4 - 2\cos\beta\sqrt{(f_t^2 + 4C^2 - 4f_t C\sin\psi)(f_t^2 + B^2/4)}}}$$

$$\cos\beta_3 = \frac{\cos\beta\sqrt{f_t^2 + 4C^2 - 4Cf_t\sin\psi} - \sqrt{f_t^2 + B^2/4}}{\sqrt{f_t^2 + 4C^2 - 4Cf_t\sin\psi + f_t^2 + B^2/4 - 2\cos\beta\sqrt{(f_t^2 + 4C^2 - 4f_t C\sin\psi)(f_t^2 + B^2/4)}}}$$

Chapter 4

Strain Rate Dependent Behaviour, Material Instability and Localization of Organic Soft Clay

4.1 Introduction

The design of earth structures in the Netherlands has recently been undergoing fundamental changes. The triaxial test produces extremely high strength envelopes for Dutch organic clays (Den Haan, 1996, 1999), the use of which in stability analyses of dykes would yield unrealistically high stability factors. Old Dutch guidelines did not recognize this and contained non-conservative partial material factors for the triaxial test which were based on older testing methods that did not reveal the true extent of the strength envelope As the material partial safety factors are well adapted to the test method and applied design methods, efforts are underway in Dutch engineering practice to revise the partial material factors. These efforts are based on the empirical correction method, where failure is defined not at the peak of the stress-strain relationship, but well before it at some arbitrary low value of axial strain in the shear phase. A correction of this kind is unsatisfactory in the long term. It would be better to find more fundamental ways of determining the strength parameters for organic soft clays through suitable testing methods, because Dutch organic clays have a mechanical behaviour that is quite distinct from that of non-organic soils. One possible approach is then to look into the effects of strain localization in organic soft clays.

The experimental observations of the strain localization of soft non-organic clays have received some attention, but not as much as that of stiff clays. Previous experimental observations suggest that slenderness of specimens and end platen restraints play a role in the development of non-uniform deformation patterns induced in many testing apparatus, which is known as geometrical instability. Three common failure modes in elemental biaxial or triaxial tests have been identified: (a) plastic failure where barrel-type deformation is significant, (b) intermediate type with diffused rupture surfaces and (c) brittle failure where a significant single shear plane appears (Hambly, 1972). Recently, soft, normally consolidated clay (normally consolidated kaolin clay and Chicago soft clay) has been used for the investigation of strain localization (Atkinson, 2000; Sabatini et al, 1996), because (a) some new experimental techniques, such as local measurement transducers (pressure probes and LVDT's) and CT scanner are available, and (b) the increasing interest in developing sophisticated numerical models for coupled or softening analysis of soft soils, which apparently requires more precise experimental observations. It has been shown that when soft clays are loaded quickly in the standard triaxial test, there is insufficient time for pore pressures to equalize, and the sample deforms uniformly to failure. Given sufficient time for locally produced excess pore pressures to dissipate or equalize within the sample (under globally undrained conditions), strains can localize in a shear band, and strength will be reduced. Dutch engineering interests lead to the present investigation of implications of strain localization in organic soft clay for embankment slope stability, as these clays are often very impermeable. Rates of deformation on site are quite low, making it likely that the localization phenomenon described by Atkinson will develop, which would reduce the available strength considerably.

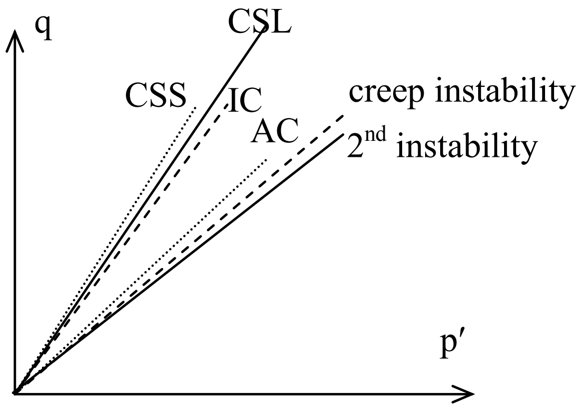

Fig. 4.1. Representation of material instabilities in the plane of shear stress, q, against effective mean stress, p'

There have been several theoretical attempts at interpreting the rupture or localization of soft soils by means of bifurcation analysis. Vardoulakis (1995) applied the material instability condition, which is known as the Mandel condition (a non-positive eigenvalue of an acoustic tensor), to the consolidated undrained shear of clay with a non-associated flow rule, revealing two kinds of instabilities of material, shown in figure 4.1. One was called internal buckling, represented by AC line for anisotropic consolidated clay, and the other was called shear banding, represented by IC line for isotropic consolidated clay. Pradel et al (1999) identified the second instability, shown in figure 4.1, in saturated loose sand under undrained shear by studying Drucker’s postulate in terms of effective stress analysis, which is actually liquefaction He said that this kind of instability of material is different from the first kind, which is the so-called characteristic stress state (CSS) in sand, and is known as the dilatancy shear band. In the meantime, a type of elasto-viscoplastic constitutive law has been developed based on the instability of an elasto-viscoplastic constitutive law for a cohesive material, such as clay (Oka et al, 1994; Plaxis Soft Soil Creep Model, 1999; Loret et al, 1990). As shown in figure 4.1, the visco-plastic instability could appear prior to the well-known critical state line (CSL). This approach is capable of describing the visco-plastic instability for both pseudo-static and dynamic problems, and the numerical calculation for the post-failure problem can be continued without changing the type of constitutive law.

The present investigation started with the introduction of a laboratory-testing program of remoulded Dutch soft clay aimed primarily at testing the strain rate. The strain rate dependent behaviour was shown in terms of failure pattern and stress relaxation, where the effects of boundary conditions and strain rates were examined mathematically and experimentally. Combined with the previous creep and undrained triaxial tests performed at GeoDelft, the material instability in the sense of Lyapunov (Hale et al, 1991) was formulated by analysing the mathematical structure of the Plaxis soft soil creep model. Its implications on the strength parameters of soft clay are represented in terms of q-p'. The special features of soft clay in the laboratory are finally interpreted in terms of material and geometrical instabilities.

4.2 Laboratory investigation of strain rate dependent behaviour and failure of organic soft clay

Extensive laboratory shear tests on Dutch organic clays have been carried out at GeoDelft in the Netherlands and other laboratories. Den Haan (1995, 1999) has summarized the large number of testing results from conventional triaxial compression of natural clay, with the following conclusions. The very high values of effective angle of internal friction were remarkable, so does the fact that it increases as the bulk density decreases. Also the so-called undrained strength was found to be higher than that of inorganic soils. Concerning the behaviour of reconstituted samples, he described a laboratory experience according to which samples prepared by mixing this organic clay with water to a desired water content well above the liquid limit and consolidated subsequently to only 15 kPa, can stand unsupported from the mould. In comparison, inorganic clay such as kaolin clay requires a consolidation pressure of at least 50 kPa. Rate dependent behaviour of Dutch soft organic clay as examined in the odeometer, showed that at constant rate of axial strain the ultimate value of $K_{o,nc}$ of this clay approaches only 0.4 or even less in an oedometer (Den Haan, 2002).

The stress-strain relationship and failure patterns of Dutch organic clays under plane strain condition have been investigated in the present study and results are presented in the following.

4.2.1 Testing apparatus and soft clay samples

The Hambly type biaxial device at TU Delft (Allersma, 1993) shown in figure 4.2, is used to contain soft soil samples in a cubical cell with a fixed height of 50 mm and a variable surface of 2500 mm^2 to 22500 mm^2. All the boundaries are rigid steel plates. The displacements of four boundaries can be controlled very accurately. Four load cells are used to measure the total stress at the boundary. The pore pressure at the centre of the sample can be measured by a pore pressure probe inserted from the bottom of the sample. The fixed top and bottom glass platens introduce the plane strain condition to the sample and a camera view from the top of the sample is used to observe the progress of deformation throughout the test.

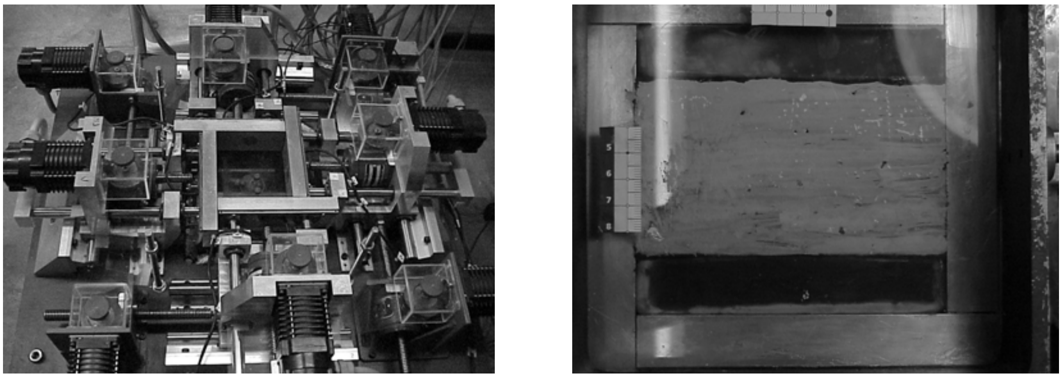

Fig. 4.2. Biaxial testing facility (left); biaxial cell with a sample and two water bags (right)

The soft clay used was taken from a research site Oostenvaardenplassen in the central Holland, and remoulded at GeoDelft. For a sample with water content of 79%, and specific density of 2.53 g/cm^{3,} the plastic and liquid limits are 37% and 120%, respectively. Clay is trimmed into the prismatic samples with two dimensions, i.e. 100*100*50 mm (length*width*height, square sample) and 120*60*50 mm (length*width*height, slender sample).

4.2.2 Testing programme

All samples were consolidated at a constant rate of 0.5 mm/hr, i.e. a constant strain rate of 0.005/hr preceding the shear. A total of 12 strain rate-controlled tests were divided into two groups each with a particular shear rate, i.e. the D ("drained") series (sheared at the rate of 0.5mm/hr) and the U ("undrained") series (sheared at the rate of 5mm/hr, i.e. the strain rate of 0.05/hr). Some samples were also sheared at an intermediate rate of 1mm/hr, i.e. a strain rate of 0.01/hr, referred to as the UD series. Figure 4.3 illustrates the strain paths involved for the D test series, which were also applied to the U and UD series. In order to investigate the influence of slenderness of samples and boundary walls on the failure pattern, an additional 4 tests on slender samples (120*60*50 mm) were performed with two water bags (see figure 4.2). Some tests have been monitored with the camera to trace the development of cracks or shear bands. In tests D06 and U06 the intermediate principal stress (out of plane) was measured with an additional load cell in the upper plastic cover. A sealing technique in which the samples are enclosed in liquid latex that is then solidified, allowed applying undrained conditions for slow undrained shear tests. Moreover, several relaxation tests and stress-controlled shear tests were also performed.

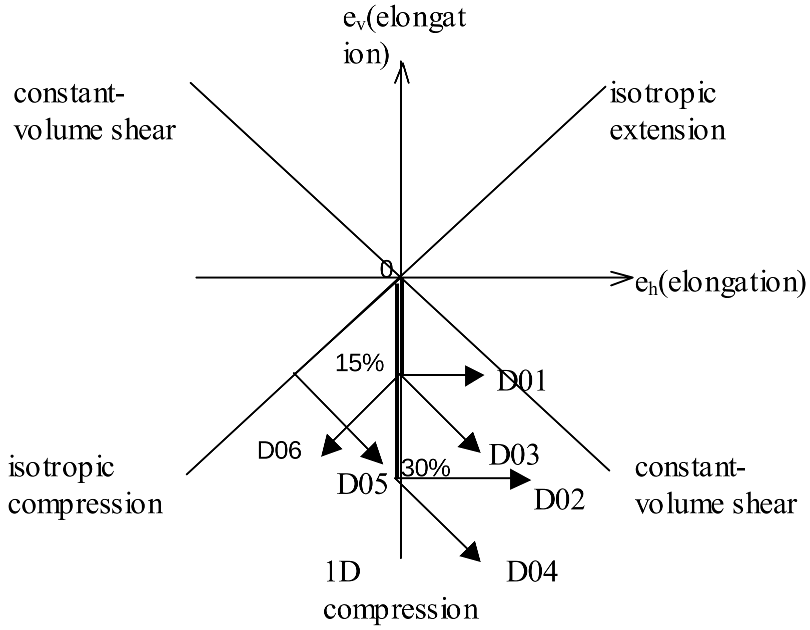

Fig. 4.3 Strain paths involved in plane strain shear tests

4.2.3 Error analysis of laboratory investigation

Testing errors are inevitable. A clear analysis is essential for the interpretation of observed phenomena, especially for the subject concerned here, i.e. material instability and localization of soft soil, as even a small error could lead to instable behaviour of materials. Two aspects were examined with respect to the stress measurements. First, the frictional shear stress between the tested soft clay (without latex membrane) and greased steel platen was measured. It is generally small, e.g. 3% of the normal stress, but sometimes it approaches 15%. This boundary friction is not measurable during the shear tests, but it can be a source of initiation of cracks. Secondly, the measurement of stress relaxation of this soft clay (strain maintained constant after 1D compression) indicates a rather rapid degradation of stress. A cubic rubber sample or a water bag in the biaxial cell showed a more reasonable relaxation, e.g. the average relaxation rates of a rubber sample at 20^0C and a water bag were estimated as 0.75 kPa/hr and 0.25 kPa/hr, respectively. These observations suggest that stress measurement of soft clay at the boundary depends on both the properties of clay and the interface behaviour between clay and steel platens, such as stiffness, saturation and viscosity etc. In the past the reliability of stress measurement in this kind of biaxial cell has been a primary concern (Topolnicki, 1987). It should be mentioned that the condition of zero strain rates in this biaxial apparatus is controlled to compensate the elastic deformation of the load cells. The accuracy of control operations, such as the ceasing or rewinding of the moving loading platens, is well below 0.01mm, but it is not certain whether this is enough for relaxation or constant volume shearing tests, which could cause a relatively quick and significant change of stress. Local drainage may occur at the interfaces of clay with steel platens, which are also responsible for the measured stress characteristics. The pore pressure sensor installed in the centre of the cell cannot indicate the development of water pressure on the interfaces. The faster the tests, the less reliable effective stress measurements are. This effect of strain rates has to be taken into account for the interpretation of laboratory observations.

4.2.4 Laboratory results

The processed testing results regarding the effect of strain rates are presented in terms of (a) the influence of stress relaxation, (b) 1D and isotropic consolidation, (c) constant volume shear, and (d) deformation mechanism and failure patterns.

(a) Stress relaxation. Two relaxation tests were performed following 1D compression at two constant rates of strain (i.e. 0.5% per hour and 5% per hour); shown in figure 4.4. The decay of mean stresses of samples is shown for which an exponential decay function fits the experimental data. The functions are expressed in equation (4.1), in which T [hrs] represents relaxation time and s [kPa] represents effective mean stress. The mean stress decays more strongly for a faster rate of pre-consolidation.

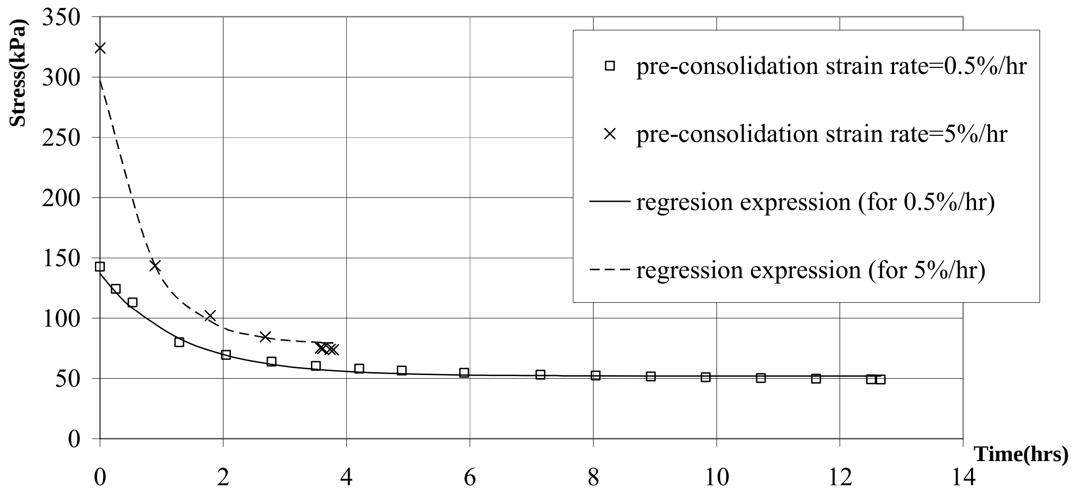

Fig.4.4. The effect of pre-consolidation strain rate on stress relaxation of organic soft clay under plane strain condtions

$$s = 85e^{-0.78T} + 52 \quad \text{for slow pre-consolidation test at 0.5\%/hr} \qquad (4.1a)$$

$$s = 219e^{-1.35T} + 78 \quad \text{for quick pre-consolidation test at 5\%/hr} \qquad (4.1b)$$

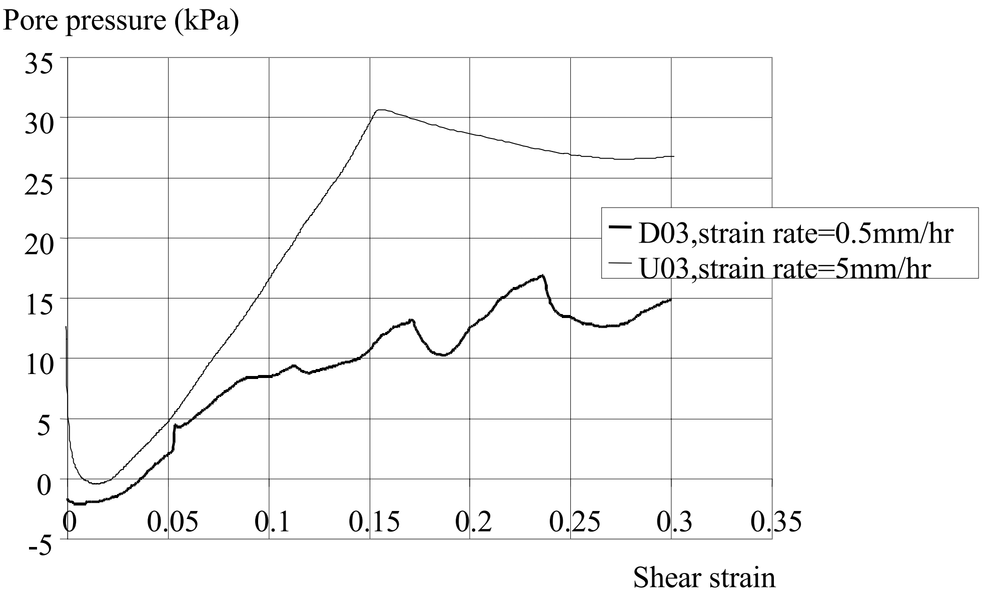

Fig. 4.5. Variance of the pore pressure measured during isochoric strain paths

(b) K_0 pre-consolidation and plane strain shear. The results of selected tests are presented in Table 4.1, where s' and t denote the mean stress, $(\sigma_1+\sigma_3)/2$ and the shear stress, $(\sigma_1-\sigma_3)/2$. The variance of calculated φ′ in the last column is more significant than that of $K_{0,nc}$ in the 4th column. But obtained higher values of $K_{0,nc}$, approximately 0.7, than those of $K_{0,CRS}$ (constant rate of strain oedometer tests), approximately 0.35 (Den Haan, 2002), are because the tested clay in the present study is remoulded. The errors in stress measurement are partly the reason. A significantly increased φ' in case of slower shearing rate is observed. The intermediate principal stress as measured in one test follows the average of the major and minor principal stresses, just a little bit less. To calculate the effective stress the average pore pressure is measured with a probe centrally placed in the sample. It may rise up to 5%-10% of total stress during the consolidation phase. As shown in figure 4.5 the pore pressure recorded during a volume- constant strain path oscillates, which may be the consequence of controlled strain conditions in the biaxial cell. The pore pressure will fluctuate as it is generated by both decreasing mean stress and increasing shear stress. Moreover, the measurements of pore pressures are scattered due to the lack of saturation and due to the leakage of the measuring system (those gaps in between biaxial cell-walls). Back pressure cannot be applied in the apparatus.

Table 4.1 $K_{0,nc}$ pre-consolidation and plane strain shear

Tests	$K_{0,nc}$ consolidation at C.R.S. of 0.5 mm/hr			Shear failure		
	s'(kPa)	t (kPa)	$K_{0,nc}$	s'(kPa)	t (kPa)	φ'(degrees)
D03	129	15	0.79	27	23	31
D04	341	64	0.68	121	72	
U03	125	15	0.78	55	44	16
U04	335	72	0.65	150	70	
D01p	136	21	0.73	136	-	-
D02p	342	62	0.69	342	-	-

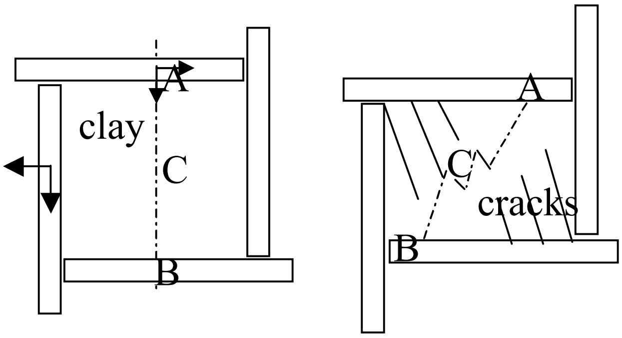

(a) initial state (b) failure state

Fig. 4.6 Biaxial deformation mechanism under plane strain conditions; arrows indicate the directions of movements of platens.

(c) Deformation mechanism. The rigid or confined boundary conditions will inevitably induce boundary shear forces. This leads to the frequently observed deformation mechanism in most tests as sketched in figure 4.6b (cf. figure A4.5). The cracks, which are visible with the naked eyes, may initiate at the corner of biaxial cell and develop along the diagonal to a damage zone near the centre of the tested sample. This deformation mode is reproducible, and the central line of ACB at the initial state (figure 4.6a) always changes to a serrated shape, which implies that both rotation and sliding in between the cracks occur. In case of a more flexible boundary, e.g. the presence of water bags, the sample may bulge in addition to the formation of cracks. The applied strain rates, i.e. 0.5 mm/hr, 1 mm/hr and 5 mm/hr, could lead to different failure patterns as shown in figure 4.7. The cracked zone widens as the strain rate slows. Furthermore, conjugate cracks, which are almost perpendicular to each other, occur in the case of the intermediate strain rate, i.e. 1 mm/hr (see figure A4.3).

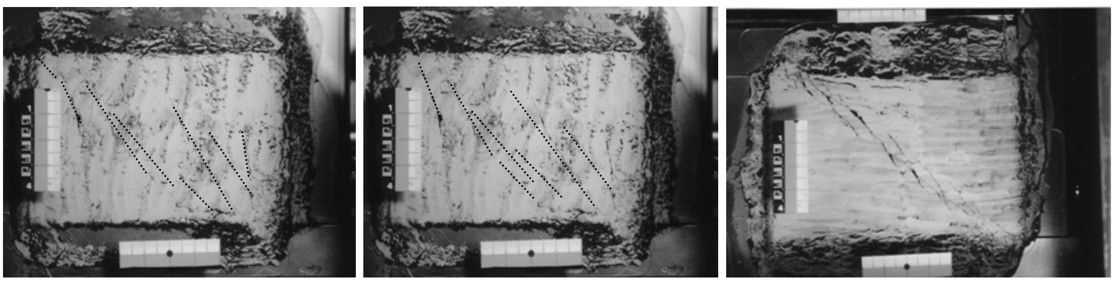

(a) shear rate = 0.5mm/hr (b) shear rate = 1 mm/hr (c) shear rate = 5 mm/hr

Fig. 4.7 The effects of shear strain rates on deformation mechanisms of soft clay: dash lines added in the pictures (a) and (b) help indicate the observed cracks.

4.3 Theoretical interpretations of laboratory observations.

The effects of strain rates on consolidation and shear failure of saturated soft clays are analyzed as follows on the basis of the observed laboratory phenomenon. The purpose is to gain an insight on the main causes of strain localization in soft saturated clays. A problem of plane strain squeeze at constant rate of strain is defined for modelling of the 1D consolidation performed in biaxial cell, and the so-called Poisson differential equation in terms of pore pressure is obtained. The drainage conditions, which are largely unidentifiable in the laboratory tests, can be assumed, and the induced compressive strain fields are obtained from the solution of the differential equations. Regarding the initial conditions, both the non-uniform and transient parts of the strain distribution at the end of consolidation must inevitably be accounted for in interpreting the results of undrained shear tests. Both are also strain rate dependent. Following the consolidation, the pre-failure softening and creep rupture of soft clays observed during the undrained shear phase, will be explained by the rate-dependent instability of material.

4.3.1 Theoretical solutions for 1D plane strain squeeze at constant rate of strain

Consider a plane strain situation in the xy-plane as illustrated in Appendix 1 of this chapter. The axis z is the out of plane direction. . A saturated soil specimen with the dimension of 100*100*50 mm, is set in a biaxial chamber of Hambly type (see figure 4.2), and compacted in the direction of y at constant rate of strain (denoted as r). As mentioned before the drainage conditions are not well controlled. Darcy flow is therefore allowed in a theoretical approach only either in the direction of z, or direction y, or direction x or both x and z. Other assumptions are: (a) infinitesimal strain is concerned, (b) linear elastic behaviour of soil skeleton, (c) frictionless boundary platens, (d) isotropic material. Applying the mathematical techniques of solving corresponding differential equations the distribution of strain and pore pressure within the sample is obtained for different drainage conditions.

The distributions of vertical strain in the direction of y in a consolidated sample can be changed by the drainage conditions. Strains in the direction of compaction are uniformly distributed through the whole sample, i.e. the average imposed strain of $r{\cdot}t$, if the Darcy flow and compaction of soil are not in the same direction. In case of Darcy flow in the same direction as the compaction the strain can be composed into three parts, namely, the uniform strain of $r{\cdot}t$, a non-uniform steady part and a transient part that will decay with the time. Therefore, this pre-consolidation induced strain distribution when followed by the shear-loading phase influences the localization of strain. Before localization occurs, the average pore water pressure at the central point of the sample is primarily determined by strain rate and coefficient of permeability of the clay. The quicker the consolidation test, the more pronounced is the pore water pressure at the central point of the sample, and effective stresses become less homogeneous which can be quantified with the theoretical approach discussed in Appendix 1 of this chapter.

4.3.2 The instability of an elasto-viscoplastic material

The viscous property of clay is responsible for time effects such as relaxation and creep. It also affects consolidation. The combined effect of viscous behaviour and drainage might be as follows: Soil behaves stiffer when the rate is higher, and non-linear consolidation is faster when the hydraulic gradient is higher. However, the combined effects become more complicated if plasticity of soft clay has to be taken into account or strain localization occurs. The strain rate dependent deformation mechanisms of soft clay are evidently related to both viscosity and plasticity. As investigations of creep rupture and shear failure of K_0-consolidated clay have been reported in the literature, the effort is here focussed on the investigation of the instability of an elasto-viscoplastic material. The soft–soil-creep model (SSC) implemented in Plaxis is used for this analysis.

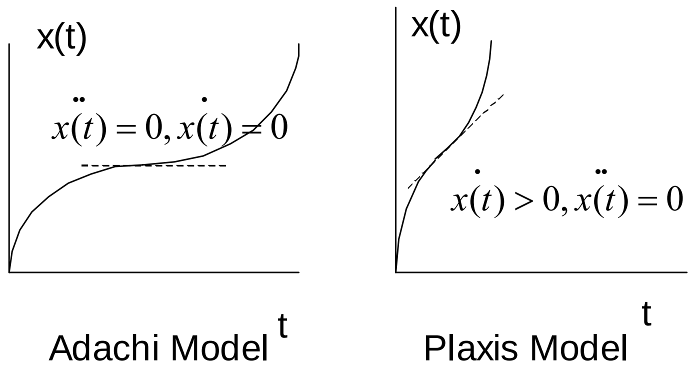

Fig.4.8 The mathematical implication of SSC model regarding undrained triaxial creep rupture: the Lyapunov instability problem.

Undrained triaxial creep leads towards rupture in a decelerating-accelerating way discovered in laboratory and practice (figure 4.8). The mathematical structure of SSC -model as examined in Appendix 2 of this chapter proves that there is a zero value of acceleration of creep displacement. It is this exact moment at which the creep rupture starts. The prediction of SSC -model in terms of creep displacement of x(t) and creep time of t is plotted in figure 4.8. Creep rupture could start at a certain time with a non-zero creep rate. Compared to Adachi's model (Adachi et al, 1996), graphically represented in figure 4.8, the two models are identical with respect to the description of undrained triaxial creep rupture except that the latter has a zero value of creep rate at the start of creep rupture. Such a feature of the trajectory of a material, i.e. non-negative velocity and zero-acceleration is instable in the sense of Lyapunov (Hale & Kocak, 1991). The observed undrained triaxial creep rupture is therefore interpreted as a rate dependent instability.

In the following attention will be focused on the problem of the pre-consolidated clay underlying undrained triaxial shear at a constant vertical rate of strain of *r*. At the onset of softening in the shear phase at time t, the effective stress path has a horizontal tangent and the stress ratio η_s is smaller than the critical stress ratio. For this specific moment, the stress conditions have to be satisfied with the following equations.

$$q_s = \eta_s p_s^{'} \quad \text{and} \quad \dot{q} = 0 \tag{4.2}$$

This yields the following stress ratio (Appendix 2 of this chapter):

$$\frac{2\eta_s}{M^2-\eta_s^{\,2}} = \frac{r}{\left.\dot{\varepsilon}_v^e\right|_{\eta=\eta_s}} = \frac{r}{\left.-\dot{\varepsilon}_v^c\right|_{\eta=\eta_s}} = \omega \tag{4.3}$$

in which, $\dot{\varepsilon}_v^c$ represents the rate of creep volume strain (compression is negative) and $\dot{\varepsilon}_v^e$ is the rate of elastic volume strain. The second equality in (4.3) results from the vanishing volumetric strain rate under undrained conditions, $\dot{\varepsilon}_v^c = -\dot{\varepsilon}_v^e$.

Hence, it follows that:

$$\eta_s = \frac{1-\sqrt{1+\omega^2 M^2}}{-\omega} \tag{4.4}$$

in which, $-\eta_s \in (0, M)$; M = stress ratio at the critical state

Table 4.2 The stress ratio η_s at the start of shear softening in soft clay

M \ ω	-1	-5	-10	-50	-100	-1000
1	-0.414	-0.819	-0.905	-0.980	-0.990	-0.999
2	-1.236	-1.809	-1.902	-1.980	-1.990	-1.999

Calculations of η_s are made for a hypothetical material with certain M, with respect to a set of possible ω; results are shown in Table 4.2. It shows that the material would soften much earlier (η_s is smaller) for smaller ω values. Given a constant rate of strain r, this also implies that more significant viscous creep or elastic swelling of the material leads to a more distinct softening. Lower rate r will likewise result in more distinct softening.

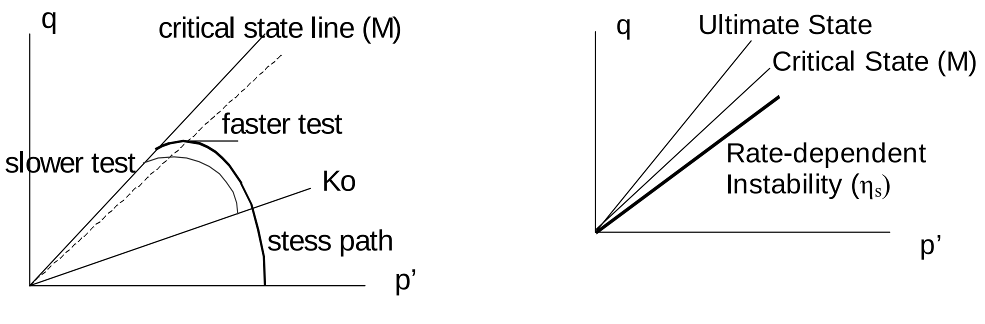

Fig. 4.9 Strain rate dependent softening (left), and instabilities of soft clay (right).

With respect to material instabilities represented in figure 4.1 a new one is added in figure 4.9, which is related to η_s. Before the ultimate state of soft soil, there are two material instabilities. One is the well-known critical state line, and the other is rate-dependent instability, discussed above, such as undrained creep rupture and undrained shear softening. These two instabilities are different. The critical state instability is related to the vanishing of the rate of volume strain. The rate-dependent instability is related to the vanishing of the acceleration of the volume strain.

4.3.3 Interpretation of observed localization of soft clay

Rate-dependent instability of material should be responsible for the observed deformation mechanisms of soft clay in biaxial tests. The soft clay with respect to slower rate has more potential of being instable. More discontinuities of deformation (cracks) occur in the tests. In addition to this material instability, boundary conditions play an important role in the development of possible deformation mechanisms. The influences of drainage conditions and boundary friction, and displacement and velocity conditions on the boundaries are important. It is likely that gaps or discontinuities of displacement develop at rigid boundaries in case of active straining, while shear banding is more likely at flexible boundaries. All these influencing factors on localization of soft clay can be taken into account in numerical simulation by a suitable extension of the constitutive material model.

4.4 Summary

The rate-dependent behaviour of saturated soft clay is carefully examined in the laboratory and by available mathematical models. It is suggested that the observed phenomena, the rate-dependent deformation mechanisms, creep rupture and pre-failure softening, are related to a rate-dependent instability of material. The combined effect of viscosity and drainage is addressed by demonstrating the correlation with failure patterns of soft clay. Such a correlation has been quantified within state of the art framework of elaso-viscoplasticity. It is emphasized that the undrained conditions applied for both the theoretical analysis and the engineering interpretations for strength of soft clay do not occur in laboratory and practice. To improve the knowledge of the strength and deformation of soft clays, local drainage should be taken into account. Unfortunately, the measurement of distribution of pore water pressure in the element tests requires more reliable techniques than available in this study. Hopefully, increasing possibilities of numerical simulations on softening will allow for extending this aspect. Localization of soft clays is relevant, both scientifically and practically.

Appendices of Chapter 4

Appendix 1. Theoretical solutions for 1D plane strain squeeze at constant rate of strain

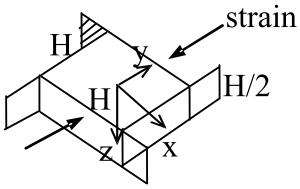

Fig. A4.1 Biaxial test

Consider a plane strain situation in the xy plane as illustrated in figure A4.1. A soil specimen with the dimension of *H*H*H*/2, is set in a biaxial chamber, and compacted in the direction of y at constant rate of strain (denoted as *r*). The drainage conditions are allowed in one direction, x, y, or z direction, in two directions both x and z. Other assumptions are: (i) infinitesimal strain is concerned, (ii) linear elastic behaviour of soil skeleton, (iii) frictionless boundary platens, (iv) isotropic material.

(a). Drainage is perpendicular to the strains (in the direction of x or z).
Strain compatibility condition in the direction of compaction is:

$$\varepsilon_y = -du_y / dy \qquad \text{(A4.1)}$$

where compressive strain is chosen positive. So the equilibrium equation in terms of displacement will read as below

$$\frac{\partial^2 u_y}{\partial y^2} = 0 \qquad \text{(A4.2)}$$

where *E* and ν represent the elastic properties of soil skeleton. Consider the boundary conditions of displacements and drainage as follows:

$$\text{for} \quad y = \pm H/2, \quad u_y(y,t) = \mp rtH/2 \qquad \text{(A4.3)}$$

in which r is the constant rate of strain. The vertical displacement and strain will read as follows.

$$u_y(y,t) = -r \cdot ty \tag{A4.4}$$

$$\varepsilon_y = r \cdot t \tag{A4.5}$$

<u>(b). Drainage is parallel to the strains (in the direction of y)</u>
The governing equation in terms of displacement will read

$$\frac{E(1-\upsilon)}{(1+\upsilon)(1-2\upsilon)} \frac{\partial^2 u_y(y)}{\partial y^2} = \frac{\partial p(y)}{\partial y} \tag{A4.6a}$$

or $$(\lambda + 2G)\frac{\partial \varepsilon_y(y)}{\partial y} = -\frac{\partial p(y)}{\partial y} \tag{A4.6b}$$

Equation (A4.3), the boundary condition of displacements, holds. The drainage condition yields:

For $y = \pm H/2$, $p = 0$ (A4.7a)

For $y=0$, $\partial p/\partial y = 0$ (A4.7b)

Darcy's law applies as described below:

$$q_y(y) = -\frac{K}{\gamma_w}\frac{\partial p}{\partial y} \tag{A4.8}$$

So, the second governing equation for pore pressure distribution will read

$$-\frac{K}{\gamma_w}\frac{\partial^2 p(y)}{\partial y^2} = \frac{\partial \varepsilon_y}{\partial t} \tag{A4.9}$$

Differentiating both sides of equation(A4.6) with respect to y and substituting equation (A4.9) gives the following equation:

$$c_y \frac{\partial^2 \varepsilon_y}{\partial y^2} = \frac{\partial \varepsilon_y}{\partial t} \tag{A4.10}$$

where $c_y = K(\lambda + 2G)/\gamma_w$ represents the consolidation coefficient in the y-direction. The mathematical techniques used to solve the equation (A4.10) have been described (Wissa & Christian et al, 1971), where the method of separation of variables and superposition of integrals were applied. By considering the following dimensionless parameters:

$Y = 2y/H$ ($Y \in [0\ 1]$ for y=[0 H/2]) (A4.11a)

$$T_y = \frac{4c_y t}{H^2} \tag{A4.11b}$$

the strain at any point and time for the upper-half of the sample becomes:

$$\varepsilon_y(Y,T_y) = r \cdot T_y H^2 [1 + F(Y,T_y)]/4c_y \tag{A4.12}$$

in which:

$$F(Y,T_y) = \frac{1}{6T_y}(3Y^2 - 1) - \frac{2}{\pi^2 T_y}\sum_{n=1}^{\infty}\frac{\cos n\pi(1-Y)}{n^2}\exp(-n^2\pi^2 T_y) \tag{A4.13}$$

(c). Drainage is in both the directions of x and z

The equation describing the distribution of pore pressure, the so-called Poisson Equation, becomes:

$$-\frac{K}{\gamma_w}\left(\frac{\partial^2 p}{\partial x^2} + \frac{\partial^2 p}{\partial z^2}\right) = \frac{\partial \varepsilon_y}{\partial t} = r \tag{A4.14}$$

The problem described by equation (A4.14) with the homogeneous boundary condition (pore pressure has to vanish at all boundaries) belongs to so-called Dirichlet problem where Green's function could be used to find solutions. However an elaborate analytical solution to this problem, even in the case of 2D space, involves the infinite series and is therefore cumbersome. An approximate solution can be obtained by using the method of Calculus of Variation, where the so-called Euler equation has to be defined. In case of two independent variables the Euler equation can be written as:

$$\frac{\partial}{\partial x}\frac{(\partial F)}{\partial P_x} + \frac{\partial}{\partial z}\frac{(\partial F)}{\partial P_z} + \frac{\partial F}{\partial P} = 0 \tag{A4.15}$$

where $P_x = \partial p/\partial x$, $P_y = \partial p/\partial y$

The integrand for F reads:

$$F = (\partial p/\partial x)^2 + (\partial p/\partial z)^2 + \frac{2r \cdot \gamma_w}{K} p \tag{A4.16}$$

The optimized function for a quarter of the area considered in the x-z plane is:

$$I[p(x,z)] = \int_0^{H/2}\int_0^{H/4}[(\partial p/\partial x)^2 + (\partial p/\partial z)^2 + 2pr\gamma_w/K]dxdz \tag{A4.17}$$

A simple approximation to p is given by the following equation which satisfies the boundary conditions

$$p(x,z) = A((1/2)^2 - (x/H)^2)((1/4)^2 - (z/H)^2) \qquad \text{(A4.18)}$$

The task of optimization is to find the value of A that minimizes I in the expression (A4.18) which can predict the volumetric flow rate within 1% of the exact solution. Therefore, the approximate expression for p is found as follows:

$$p(x,z) = 0.263\frac{r\gamma_w H^2}{K}((1/2)^2 - (x/H)^2)((1/4)^2 - (z/H)^2) \qquad \text{(A4.19)}$$

Appendix.2 Mathematical structure and interpretations of SSC Model

The Soft Soil Creep Model implemented in Plaxis is formulated in equations (A4.20), where tensile stress and strain are taken positive. Using two equivalent stresses defined in Fig A4.2 one can derive this generalized expression of creep strain rate (A4.20a) on basis of the observed one dimensional odeometer test results. The rates of viscoplastic volume strain, $\dot{\varepsilon}_v^c$ and elastic volume strain $\dot{\varepsilon}_v^e$ are expressed in equations of (A4.20a) and (A4.20b), including the initial conditions. The constitutive law of an elasto-viscoplastic material is formulated in equation (A4.20d) in terms of total rates of principal strains and stresses. For an isotropic material, there are two elastic material parameters involved, i.e. the compression and unloading-reloading coefficients λ^* and κ^*, respectively. The stress dependent elastic tangent modulus E_{ur} and Poisson ratio ν are also used. The material parameter μ^* is used to represent the viscous behaviour. The plastic potential function p^{eq} follows the modified cam-clay yield surface; where M represents the maximum stress ratio (critical state), and (p,q) represent mean effective stress and deviator stress, respectively (figure A4.2a). The pre-consolidation effective pressure represented by p'_0 is used to indicate when the viscous volume changes occur.

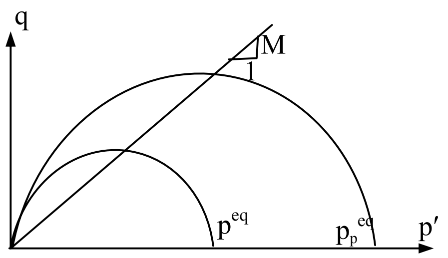

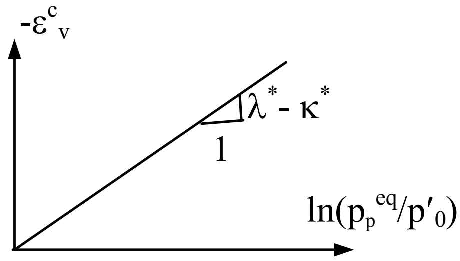

Fig A4.2 Concept of equivalent mean stress, p^{eq} and equivalent end-of-consolidation pressure, $p^{eq}{}_p$

$$\dot{\varepsilon}_v^c = -\frac{u^*}{\tau}\left(\frac{p^{eq}}{p_p^{eq}}\right)^{\frac{\lambda^*-\kappa^*}{\mu^*}} = -\frac{u^*}{\tau}\left(\frac{p' + \dfrac{q^2}{M^2 p'}}{p'_0 \exp(\dfrac{-\varepsilon_v^c}{\lambda^* - \kappa^*})}\right)^{\frac{\lambda^*-\kappa^*}{\mu^*}} \quad \text{with} \quad \varepsilon_v^c\Big|_{p'=p'_0} = 0 \qquad \text{(A4.20a)}$$

$$\dot{\varepsilon}_v^e = -\kappa^* \frac{\dot{p}'}{p'}, \qquad \text{with} \qquad \varepsilon_v^e\Big|_{p'=p_0'} = 0 \tag{A4.20b}$$

Integration of equation(A4.20b) yields:

$$\varepsilon_v^e = -\kappa^* \ln\left(\frac{p'}{p_0'}\right) \tag{A4.20c}$$

$$\begin{bmatrix} \dot{\varepsilon}_1 \\ \overset{*}{\varepsilon}_2 \\ \dot{\varepsilon}_3 \end{bmatrix} = \frac{1}{E_{ur}} \begin{bmatrix} 1 & -\nu_{ur} & -\nu_{ur} \\ -\nu_{ur} & 1 & -\nu_{ur} \\ -\nu_{ur} & -\nu_{ur} & 1 \end{bmatrix} \begin{bmatrix} \dot{\sigma}_1' \\ \dot{\sigma}_2' \\ \dot{\sigma}_3' \end{bmatrix} - \frac{1}{\partial p^{eq} / \partial p'} \frac{\mu^*}{\tau} \left(\frac{p^{eq}}{p_p^{eq}}\right)^{\frac{\lambda^* - \kappa^*}{\mu^*}} \begin{bmatrix} \dfrac{\partial p^{eq}}{\partial \sigma_1'} \\ \dfrac{\partial p^{eq}}{\partial \sigma_2'} \\ \dfrac{\partial p^{eq}}{\partial \sigma_3'} \end{bmatrix}, \tag{A4.20d}$$

with $p'\Big|_{\tau=0} = p_0'$

<u>(a) Undrained triaxial creep</u>

In case of un-drained triaxial creep, the following stress conditions apply:

$$q^2 = (\sigma_1 - \sigma_3)^2 = (\sigma_1' - \sigma_3')^2 = \text{const.} \tag{A4.21a}$$

$$p' = (\sigma_1' + \sigma_2' + \sigma_3')/3 \tag{A4.21b}$$

$$\eta = -q / p' \tag{A4.21c}$$

As the volumetric strain rate has to vanish under undrained conditions the following relation is obtained:

$$\dot{\varepsilon}_v^c = -\dot{\varepsilon}_v^e = \kappa^* \frac{\dot{p}'}{p'} \tag{A4.22}$$

Integration of (A4.22) yields:

$$\varepsilon_v^c = k^* \ln\left(\frac{p'}{p_c'}\right) + (\varepsilon_v^c)\Big|_{p'=p_c'} \tag{A4.23}$$

or

$$p' = p_c' e^{\frac{\varepsilon_v^c - (\varepsilon_v^c)\big|_{p'=p_c'}}{\kappa^*}} \tag{A4.24}$$

where p_c' is the effective mean pressure just before the execution of undrained conditions. Substitution of (A4.23) into (A4.20a) yields:

$$\overset{*}{\varepsilon_v^c}\,\tau = -\mu^*(a_1 e^{a_2\varepsilon_v^c} + b_1 e^{b_2\varepsilon_v^c})^m \tag{A4.25}$$

in which,

$$a_1 = \frac{p_c^{'}}{p_0^{'} e^{(\varepsilon_v^c|_{p^{'}=p_c^{'}}/\kappa^*)}} \quad \text{and} \quad a_2 = \frac{\lambda^*}{\kappa^*(\lambda^* - \kappa^*)}$$

$$b_1 = \frac{q^2 e^{(\varepsilon_v^c|_{p^{'}=p_c^{'}}/\kappa^*)}}{M^2 p_0^{'} p_c^{'}} \quad \text{and} \quad b_2 = \frac{2\kappa^* - \lambda^*}{\kappa^*(\lambda^* - \kappa^*)}$$

$$m = \frac{\lambda^* - \kappa^*}{\mu^*}$$

By differentiation of equation (A4.25) with respect to time(dt=dτ, t≥τ_c),

$$\overset{\bullet\bullet}{\varepsilon_v^c} = \frac{m(\mu^*)^2 \Phi_1^{2m-1}\Phi_2 + \mu^*\Phi_1^m}{\tau^2} \tag{A4.25a}$$

in which:

$$\Phi_1(\varepsilon_v^c) = a_1 e^{a_2\varepsilon_v^c} + b_1 e^{b_2\varepsilon_v^c}$$

$$\Phi_2(\varepsilon_v^c) = a_1 a_2 e^{a_2\varepsilon_v^c} + b_1 b_2 e^{b_2\varepsilon_v^c}$$

<u>(b) Undrained triaxial shear</u>

In case of undrained triaxial shear at a constant vertical strain rate of *r*, the major and minor effective principal stresses are expressed as follows in terms of q and $p^{'}$

$$\sigma_1^{'} = p^{'} - 2q/3 \tag{A4.26a}$$

$$\sigma_3^{'} = p^{'} + q/3 \tag{A4.26b}$$

$$q = \frac{1}{2}\sqrt{(\sigma_1 - \sigma_2)^2 + (\sigma_1 - \sigma_3)^2 + (\sigma_2 - \sigma_3)^2} \tag{A4.26c}$$

Because of the conservation of volume and the triaxial condition, the following holds:

$$\dot{\varepsilon}_3 = -\dot{\varepsilon}_1/2 = -r/2 \tag{A4.27a}$$

$$\sigma_2 = \sigma_3 \tag{A4.27b}$$

By substituting equations (A4.26) and (A4.27) into equation (A4.20d) the following is found:

$$\dot{\varepsilon}_1 = \dot{\varepsilon}_1^e + \dot{\varepsilon}_1^c = \frac{1}{E_{ur}}((1-2\nu_{ur})\,\dot{p}' - \frac{2}{3}\dot{q}(1+\nu_{ur})) - (\frac{1}{3} - \frac{2qp}{M^2p^2 - q^2})\frac{\mu^*}{\tau}\left(\frac{p^{eq}}{p_p^{eq}}\right)^{\frac{\lambda^*-\kappa^*}{\mu^*}} \tag{A4.28}$$

By adding the equations (A4.20d), the stress-dependent tangent stiffness E_{ur} can be derived according to:

$$E_{ur} = 3(2\nu_{ur} - 1)\frac{p'}{\kappa^*} \tag{A4.29}$$

Appendix 3 Rectilinear "undrained" deformation patterns of soft clay samples in biaxial cell

The laboratory evidences collected below might suggest that the failure patterns of soft clays are strain rate dependent, and therefore more diverse than the known two types , plastic uniform deformation and shear band.

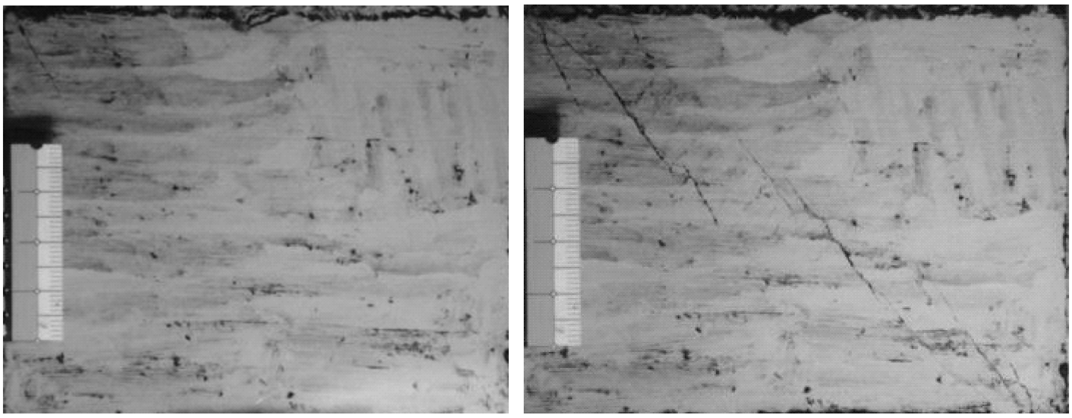

(a) imitation of cracks at corner of sample (b) conjugated cracks at a strain of 30%

Fig. A4.3 Constant volume shear test at 1mm/hr (No.UD03)

Figure A4.3 shows the test results of sample UD03 where a shearing rate of 1 mm/hr is applied. The left picture shows the initiation of cracks in the corner of the sample at a strain of 19%. The right picture shows conjugated cracks as they have further developed at a strain of 30%.

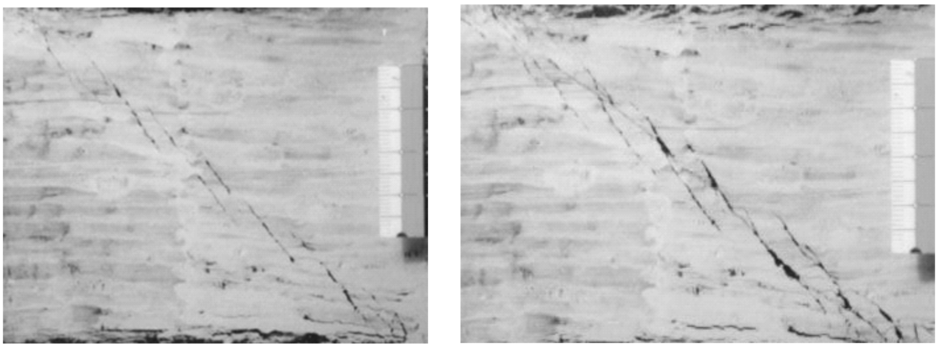

(a) diagonalized cracks initiated from corner (b) further development of diagnalized cracks

Fig. A4.4 Constant volume shear test at 5 mm/hr (No.U03)

Figure A4.4 shows the test results of sample U03 where a shearing rate of 5 mm/hr is applied. The left picture shows the diagonalized cracks from the corners of the sample at a strain of 32% (left) and in a further development at 42% (right).

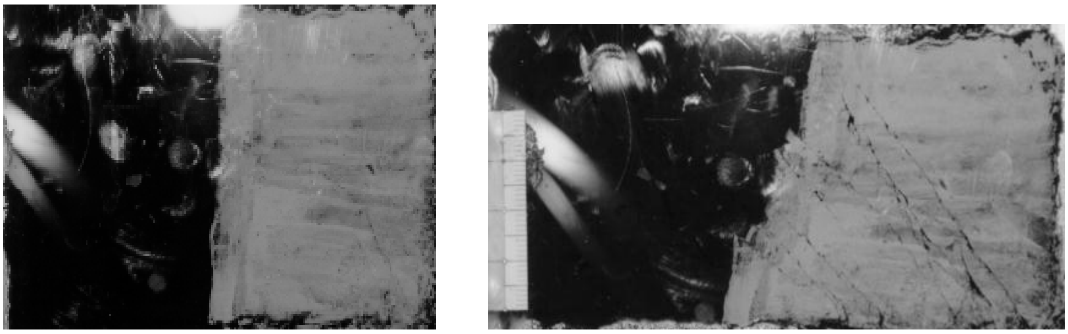

Fig. A4.5 Constant volume shear test at 0.5 mm/hr (No.D04)

Figure A4.5 shows the test results of sample D04 where a shearing rate of 0.5 mm/hr is applied. The left picture shows the initiation of cracks in the sample at a strain of 33%. The right picture, where half of the sample was painted before to visualisize the crackt, shows the cracks pattern as they have further developed at a strain of 50%.

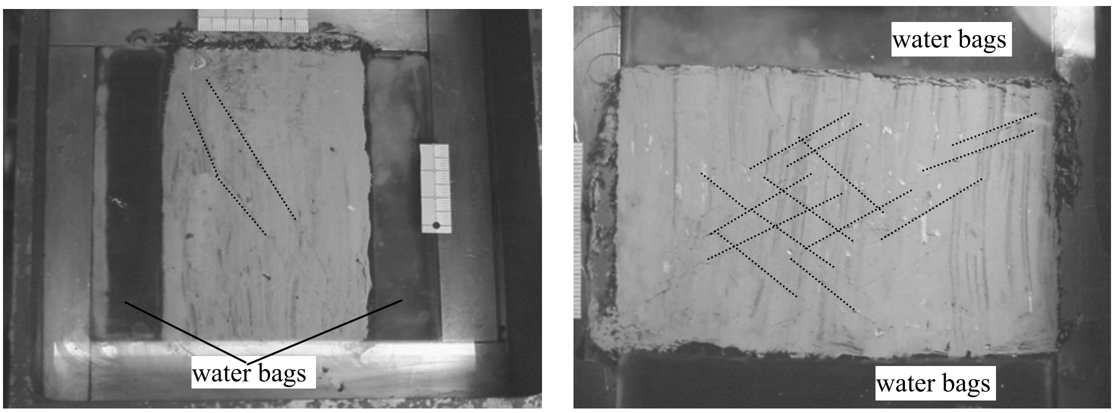

(a) two significant cracks (test No.flex03) (b) a net of cracks observed in test No.flex04

Fig. A4.6 Sample supported by water bags in biaxial cell

(added dash lines in the pictures are used to highlight the observed cracks)

Figure A4.6 shows the test results of sample flex03, where a K_0-consolidation was applied to lateral confining pressure of 55kPa, and subsequently then the sample was sheared at the rate of 1mm/hr. At both sides water bags where placed in order to eliminate the rigid boundary constraint. Cracks were observed in one direction. The right side shows a similar test set up (on two opposite sides water bags were placed), Isotropic consolidation was applied to a confining pressure of 55kPa , and then the sample was sheared at the rate of 1mm/hr. A double crack pattern was observed (double shearing).

Chapter 5

Micro-deformation and Unusual Fabric of Dutch Organic Clay

5.1 Introduction

As one of the lowest parts of a reclaimed polder (Zuidelijk/South Flevoland) in the central Netherlands, the Oostvaardersplassen comprise a complex of large shallow, freshwater lakes, reed beds, willow scrub and wet meadows. In some parts of this land, groundwater levels are kept artificially high, while other areas are allowed to undergo natural water level fluctuations. As far as is concerned in geotechnical practices the geological history of this polder is therefore limited to the period after the last ice-age (Weichselien to 8000 B.C.), at the end of which the sea levels and groundwater levels rose as a result of the melting of the ice caps, and peat formation flourished . Halfway through the Altanticum (6000-3000 B.C.) the sea level rose to such levels that transgressions far inland were possible. Periods of transgression and regression alternated for a while, during which a large proportion of the peat areas was eroded and the inland freshwater lakes Flevo and Almere and eventually the inland sea Zuiderzee developed. Sedimentation continued, and the Lake Flevo and Almere deposits (900 B.C.-1600 A.D.) occurred in fresh water conditions whereas the Zuiderzee deposit (1600 A.D.) formed in brackish or salt water conditions due to widening of the connection between the Zuiderzee and the Waddenzee. After the damming of the Zuiderzee in 1932, recent IJsselmeer deposits were formed. In the 1930's a start was made with reclaiming the parts of IJsselmeer Zuiderzee which eventually led to the creation of the polder Flevoland in 1968. The Holocene clay deposits to a depth of 5.7m below ground level are believed to be representative of Dutch organic and calciferous clay, which occur generally throughout the Dutch delta area. Dutch geotechnical engineering practice such as dykes and embankments design and construction is to occur on these soft soils. Oostvaardersplassen clay, abbreviated as OVP clay, has been used for research purposes for many years in the Netherlands.

Den Haan (1995) has summarized a large number of testing results from conventional triaxial compression of natural organic clay. He concluded that the values of angle of internal friction φ' and undrained strength c_u are remarkably high, and that these values increase as the bulk density decreases. Tigchelaar (2000) performed systematical shear tests on reconstituted OVP clay and demonstrated that a pre-failure state exists for normally consolidated clay, where deviator stress reaches maximum prior to so-called critical state line. At constant rate of axial strain, the ultimate value of $K_{o,nc}$ of this clay approaches only 0.4 or even less in an oedeometer (Den Haan & Kamao, 2003). These observations of special properties of Dutch organic clay are not understood and have been poorly investigated to date. The properties of strength and deformability of Dutch organic clay remain not understood.

Research engineers in Japan have recently realized that Japanese marine clays have a relatively high φ' as well. This was explained (Tanaka & Locat, 1999) by the presence of diatom microfossils which have a dominant influence on the geotechnical properties of this clay. As referred to by Cleveringa et al. (1995), Harting (1812-1885) already reported in 1852 about the presence of a layer with an abundance of microfossil diatoms in the Amsterdam underground. This “layer of Harting” as it is now called, contains finely decomposed plant remains, diatoms, fine sand and clay fractions at a depth of about 40m under ground level. The transition from fresh water to salt water in the Netherlands in the last 10,000 years resulted in a massive growth of diatoms, followed by decay, sedimentation and a perfect fossilization. Paul & Barras (1999) showed the Atterberg limits of the Bothkennar clay are significantly linked to the geochemical composition of organic matter and therefore the unusual observed geotechnical properties, e.g. the increased Atterberg limits and the higher yield stress ratio of about 1.6 and above, can be explained by considering the formation of flexible organic cements (absorbed large organic molecules). Meanwhile, they concluded the typical estuarine organisms have excluded the reinforcing mechanism of the plant tissues and fibers in an estuarine biological-origin clay. Their study implies the importance of fabric investigation for explaining unusual geotechnical properties of clays.

At the early ages of the development of soil mechanics, the fabric of non-organic clay was studied to investigate the anisotropic strength, deformation and permeability characteristics. From the unconfined compression tests on Vienna soft clays, Hvorslev (1960) has suggested the influences of orientation of clay particles on the pattern of rupture surfaces and strength would be important. He also addressed the physicochemical constitution of clays and recognized the intrinsic forces acting in the soil-water system are of importance. Dutch organic clay has shown distinct mechanical properties different from those of non-organic clays. This chapter presents the results of a fundamental investigation of geomechanical effects of the fabric and micro-deformation of organic clay with modern techniques. An introduction of physicochemical properties of OVP clay is first given. To discover the fabric of clay at different states, more advanced experimental techniques applied are outlined where environmental scanning microscopy (ESEM) is crucial. The description of preparation of samples used for purposes of fabric study follows as well. The characterization of fabric of Dutch organic clays is subsequently presented. Particularly, an experimental pioneering work to collect evidence of the micro-deformation of OVP clay in the ESEM chamber is attempted and presented.

5.2 Physico-chemical properties

The combination of data from the literature and from the geotechnical classification and index tests performed on a boring in the Oostvaardersplassen clay (GeoDelft contract number : CO-378510, boring number 1) has resulted in the geological and geotechnical classification of the layers encountered at the site as shown in Table 5.1 and Figure 5.1. According to Dutch soil scientific classification the upper 0.9-1.2m clay is unripened, lightly coloured calcareous young sea clay, not containing peat, under which the deeper Holocene organic clays are of interest. As the former Zuiderzee bottom has a number of characteristic features, such as the increase of organic content with depth , the increase of the carbon/nitrogen ratio with depth and the variation of the ratio of clay particles(< 2 μm) to silt with depth etc, the physico-chemical properties of the studied clay should be of concern. The physical properties of Dutch organic clay has been studied and reported by Tigchelaar et al. (2000) and Tigchelaar (2001). Water content (w) increases from approximately 35% at 0.5 m below ground-level to 200% at 2.5 m depth. Organic content (N) increases from a few percent to some 20% at 2.5 m depth. The bulk density of soil (γ_n) decreases with depth. The plastic limits (w_p) also increase with depth. The material studied here had a water content of 79%, and plastic and liquid limits (w_L) of 37% and 120%, respectively.

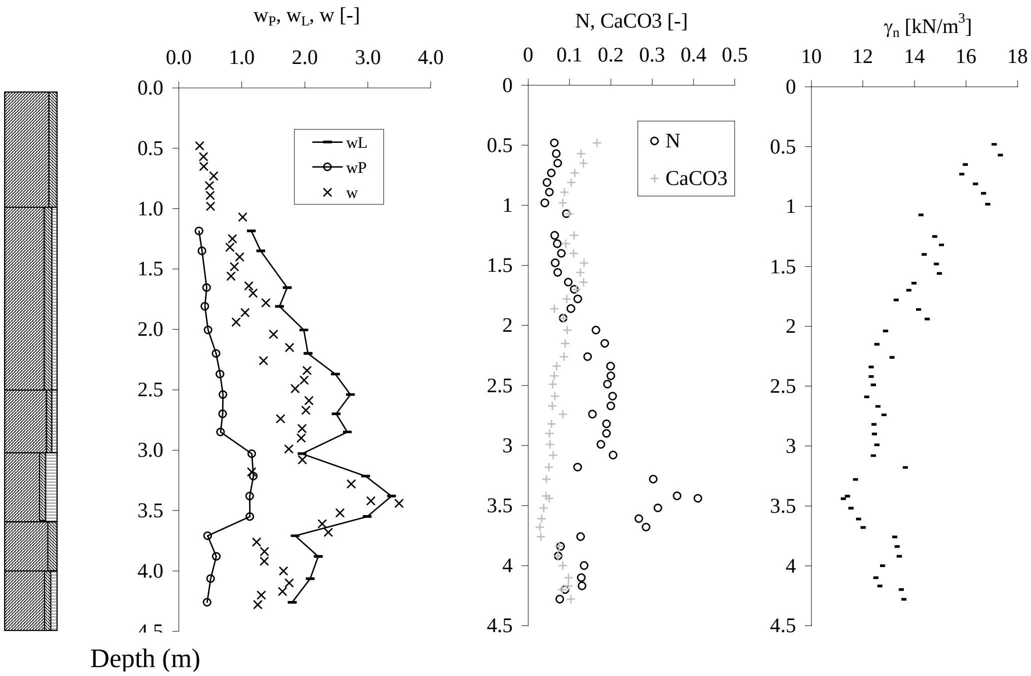

Fig. 5.1. Geotechnical data of a boring in the Oostvaardersplassen clay (GeoDelft Contract CO-378510, No.1)

Table 5.1 Geological and geotechnical classification of soils layers at the studied site in the Oostvaardersplassen

Depth (m)	Geotechnical classification	Geological year
0-0.9	clay, medium to very silty with shell remains (IJsselmeer/Zuiderzee deposit)	Holocene
0.9-1.6	clay, weakly silty, weakly organic (Almere deposit)	
1.6-2.0	clay, weakly silty, organic(Almere deposit)	
2.0-3.0	clay, weakly silty, strongly organic (Almere deposit)	
3.0-3.6	clay, strongly organic (detritus gyttja) (Lake Flevo deposit)	
3.6-5.8	peat and clay layers (mudflat deposits, clays and peats)	
5.8-	sand (Weichselien)	Pleistocene

The contents of organic matter and carbonate are 9.5% and 9.2%, respectively. Using sieves (d>38 μm) and Sedigraph (2 μm < d <38 μm) determinations, the grain size distribution indicates the dominance of silt particles up to 70% with the D_{50} of 160 μm. The specific area of 144 m^2/g implies a high activity of the clay grains concerned. As an important aspect of organic soils the specific density of dry clay grains as determined as 2.53 g/cm^3 has to be paid much attention to. Skempton and Petley (1970) demonstrated that the specific density of organic soils can be obtained from a two-component model of soil composition. A similar relation was obtained in Dutch organic soils and it also applies to the clay concerned:

$$1/\rho_s = N/1.365 + (1-N)/2.695 \tag{5.1}$$

where, ρ_s is specific density of the dry soil matter; N is the loss-on-ignition (approximately equal to organic content); organics with density 1.365 and mineral matter with density 2.695.

5.3 Experimental methods

Philips PW 1729 with k_α radiation of Cobalt was employed to perform X-ray diffraction (XRD) on the representative samples collected at a depth of around 1.5 m below ground level. Besides the average analysis of mineralogical composition by XRD, an electron microprobe, which is a combination of XRD and conventional scanning electron microscopy (SEM), was used to identify non-organic microstructures of a clay sample in terms of chemical elements composition, at a magnification of 2000 to 4000 times. The morphology of the non-clay fraction and biological information of OVP clays were obtained by a Leica polarizing optical microscope connected with a digital camera with a magnification up to 630 times. Micro-chemical tests, such as acid and organic solvent solubility, were performed under the microscope to examine the presence of carbonate and organic microstructures at a level of tens of micrometers. Philips XL-30 ESEM (see Appendix 1 of this chapter) combined with energy diffraction analysis of X-rays (EDAX) was employed to characterize the clay fabric in its different states, at magnifications ranging from 250 to 4000 times. The advantage of ESEM is to allow a sample to be examined intact under natural moisture conditions rather than as required in SEM where a standard procedure of drying-polishing and coating must be followed. A built-in cooling stage in the chamber of ESEM allows the relative humidity close to the clay sample surface to be adjusted from 95% to a completely dry situation.

Experimental investigation of the micro-deformation of the clay fabric was performed with a 10 kN tension/compression loading stage specially designed for the Philips XL30 ESEM. This small uniaxial loading device, made operational in this study for soil, is shown in Figure 5.2 and it can clamp a prismatic or spindle-shaped sample ($l \times w \times h$=35×15×15 mm) placed in the chamber of ESEM, after which live changes of clay fabric due to uniaxial compression/extension at magnifications of 500 and 1000 times can be captured. The loading occurs at a constant velocity, 2 μm/sec being employed generally throughout this study.

5.4 Sample preparation

The fabric of clay evolves with its geological and geotechnical history. Four types of clay fabric were prepared. The first type was the natural and intact fabric representing

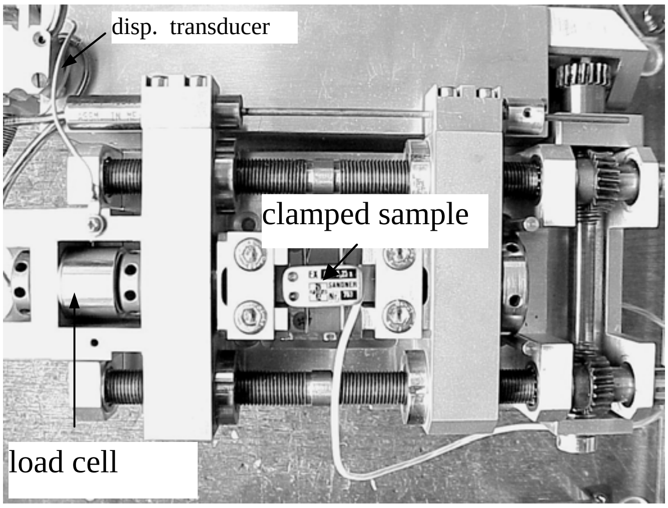

Fig. 5.2. Tensile/compression module for ESEM

the natural soft Holocene clay collected with a soil sampler. Some of these fresh clays were remoulded under vacuum at a water content of about 140% and consolidated in a cell for half a year at a pressure of 45 kPa. This is, denoted as remoulded clay, and is the second type of fabric studied. To investigate the role of organic matter, the third type of fabric was artificially produced in chemical laboratory in which efforts were made to remove organic compounds of clay. Two methods were followed: the Soxhlet extraction method was applied to an amount of OVP clay powder by using an extractant mixture of hexane and acetone(1:1). 12-hours extraction for 20g clay powder was repeated several times to collect enough clay residuals for the following process of reconstitution. The second method applied to remove organics from the clay was by means of a table centrifuge. Clay suspension was centrifuged at a speed of 3000 rpm for half an hour where lighter organic matter was separated to the top solution and non-organic clay particles settled at the bottom. Both methods proved effective and the collected residual clay powder mixed from the soxhlet and the table centrifuge was then consolidated and reconstituted in an oedometer to a pressure of 15kPa. The fabric of this third reconstituted clay is termed artificial inorganic fabric. On the occasion of a large geo-centrifuge model test at Geodelft, a piece of OVP clay underneath a model dyke was sampled in the shear zone where sheet piles crossed as sketched in Figure 5.4e to represent fractured fabric of the shear zone: the fourth studied fabric.

The different techniques applied to the study of the clay fabrics require specific preparation methods. XRD analysis was carried out on 80^{o} C oven-dried and crushed clay fraction of samples (<50μm). A standard clay slice with a thickness of 30 μm was prepared for the polarizing optical microscopy. Biological observations with an optical microscope need a drop of clay suspension. Concerning the microprobe, a

30mm diameter resin-contained clay cylinder was made, the surface of which was polished and carbon-coated. Conventional SEM also requires a dried-polished and gold-coated sample. Hand splitting or a steel saw cutting surface is good enough in ESEM. By a specially designed aluminum mould, spindle-shaped clay samples for extension and prismatic clay samples for compression in ESEM could be prepared.

5.5 Characterization of fabric of Dutch organic clay

The fabric described below for Dutch organic clay includes the size, the formation and the function of different fabric elements at a level of a few μm to hundreds of μm.

5.5.1 Clay mineral composition

XRD analysis (shown in Figure 5.3) revealed the mineral components where quartz (A) and calcite (B) are significantly dominant, supplemented with minor quantities of dolomite, feldspar and plagioclases (E). Illite (C), chlorite (D) and glauconite are three clay minerals which represent a 10% fraction of the solids of the examined clay samples. Organic matter was estimated to around 10% of total sample mass. The low content of clay minerals, and the absence of clay minerals such as kaolinite and montmorillonite, is conspicuous, suggests Dutch organic clay is unusual.

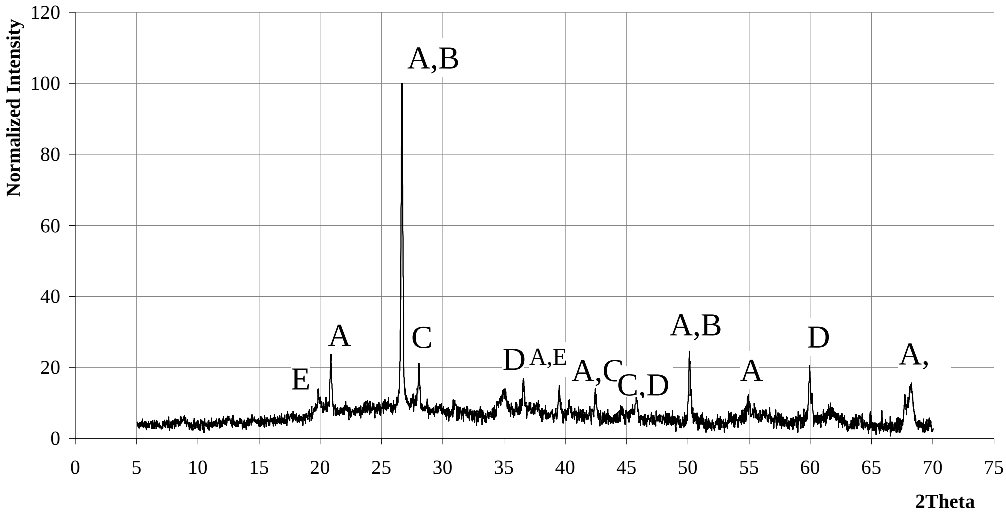

Fig. 5.3. XRD analysis results

5.5.2 Fabric elements, interaction and pores

A clear identification of fabric elements is rather complicated, because each element may have not only a morphological but also a physicochemical meaning. A preliminary result is presented in an atlas of fabric elements in Table 5.2 where the identified fabric elements are grouped into six categories. These are in accordance with the classification used in the areas of clay science and micro-geology (Grabowska-Olszewska et al, 1984; Smart et al, 1981). Quartz grains were found distributed in a wide range sized from 10 μm to 100 μm and statistics of hundred of micrographs showed a 50μm size is the most relevant one. However, as the first micrograph shown in Table 5.2 indicates, micro-crystals of silica are growing on the bigger crystalline silica or quartz silts in the area specified by solid white circles while some quartz in the area specified by dashed white circles has no secondary growth of micro-crystals. All this crystallized silica should be responsible for the silt particles of

Table 5.2 Atlas of the fabric elements of Dutch OVP clay

Fabric elements	Micrographs from optical microscopy, ESEM, SEM and microprobe	Size(μm) and Content
(a) Quartz grains (SiO_2)	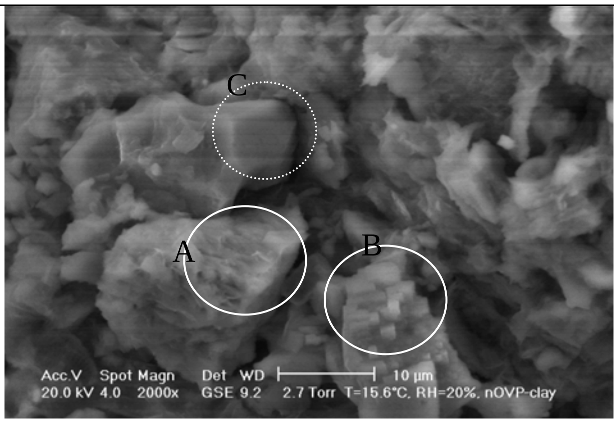 10um (scale bar)	10-100 rich
(b) Microfossils (1) Diatom ($SiO_2.nH_2O$)	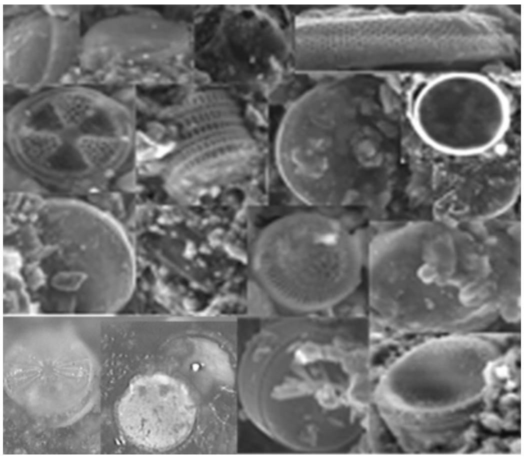 (lines in this picture come from the mergence of variable pictures)	30-80 less rich (as counted as 10 diatoms found in a area of 315×315μm)
(2) Shell microfossil ($CaCO_3$)	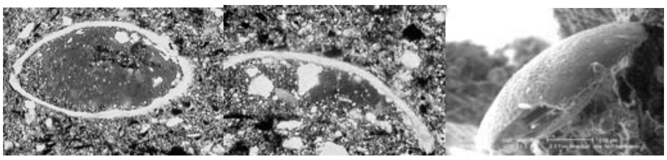 150μm	5-700 less rich
(c) Inclusions of microcrystals (salt, pyrite)	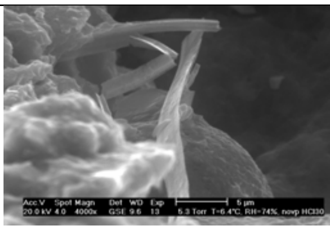 5μm 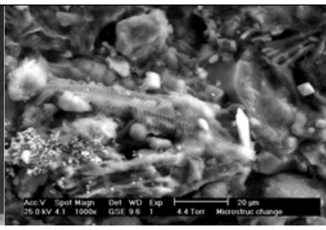 20μm	<10 less rich *to be continued*

(d) Primary particles and microaggregations (Illite & Chloride) Organic films, Sulphate	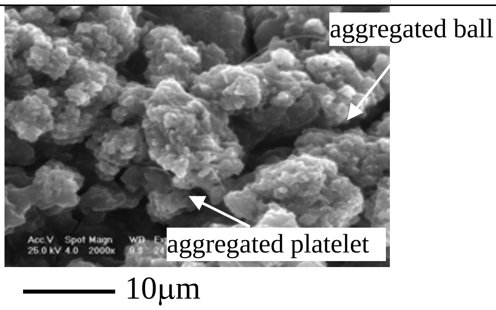 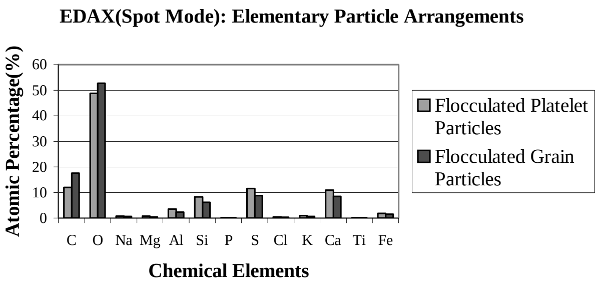	0.5-20 less rich
(e) Organics-related	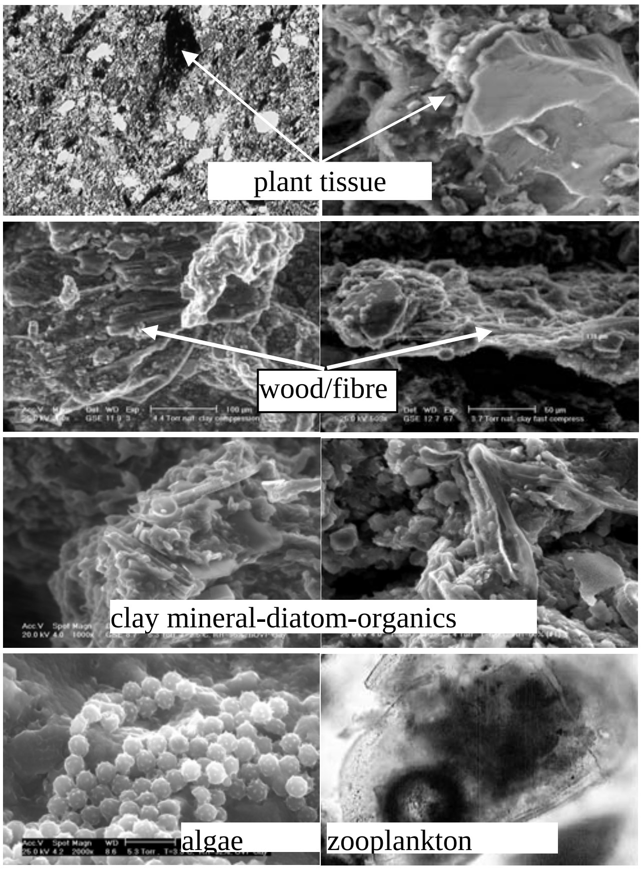	0.1-500 rich *to be continued*

(f) unknowns	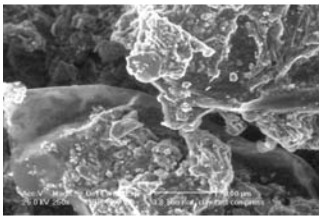 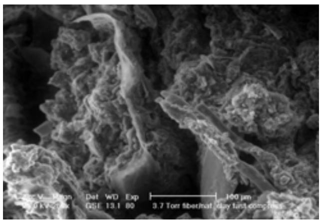 100 μm	300-500 poor

this material. The bulky nature of micro-crystals of quartz is proof of a quick deposition of silica. The inclusions of microfossils such as micro-flora and micro-fauna are mainly found as fragments of the diatoms and carbonaceous skeletons. A collection of diatoms found in this clay is shown in Table 5.2 where the centrosymmetric type is dominant with a size of around 50 μm. The content of diatoms is less rich compared to quartz grains and is lower in the depth range of 1.8 m to 2.2 m relative to in the depth range of 2.8 m to 3.0 m. The diatoms are golden-brown algae which grow in fresh water conditions and secrete frustules of amorphous opaline silica ($SiO_2 \cdot nH_2O$). Many micro-pores remain within its skeleton which could lead to variable bulk densities ranging between 1.8 to 2.2g/cm^3 and high water content (Tanaka et al, 1999).

Both quartz and amorphous opaline silica found in ESEM characterize the microstructures of the phase of SiO_2 in XRD., Calcite and dolomite have been discovered by polarized microscopy but in too small amounts to correlate with XRD results. A transparent egg shell-like microfossil was sometimes found and proven to be carbonate,, see Table 5.2. These microfossils have an estimated thickness of 20μm, and a size of around 700μm. Besides its intact forms, broken pieces are found, sized in a wide range. Along with silt grains and microfossils, microcrystals of ore minerals and salts of biochemical origin in a size of several scores of μm are found, usually as collomorphic accumulations of finely dispersed $CaCO_3$ flakes , octahedral pyrite and filamentous gypsum. Primary clay mineral particles shaped either as isometric or elongated plates (<2μm) such as illite and chlorite are aggregated to spherical or plate-shaped micro-aggregations in a size of around 20 to 40 μm.

Organic matter related fabric was found present in different microstructures. As has been reviewed (Turner & Millward, 2002) suspended particles sized from 1 μm to 500 μm form sediments (i.e. medium clay and silt, fine sand and mineral-organic microaggregate) and seston (i.e. bacterium, phytoplankton and invertebrate larvae). The similarity between the micrographs in Table 5.2 and the literature descriptions suggests that the organics related matter in Dutch organic clay have their origin in suspended particles which may play a key role in the estuarine biogeochemical cycles. Decomposed or decayed organisms and plant debris (i.e. colloid or humic material) which are dark brown in colour, coat the surface of clay minerals in the form of organic or hydrogenous films. The various types of mineral-organic microaggregates are popular, such as aggregates including wood or fibre remnants and aggregates including clay minerals, carbonate flakes, diatoms and organics. The biogenic components such as a dead zooplankton and algae remains were found as individual phases as well. Some components as big as a few hundred μm remain unidentified, and are presented in Table 5.2 as unknown material.

These six groups of fabric elements interact at contacts whose number, geometry and nature will primarily determine the strength of clay. The face to face contacts are dominant between primary clay particles at the nanometer scale. Almost no direct contacts between silt grains, e.g. silt grains A, B and C in the first micrograph listed in Table 5.2, are observed as they are connected by the fabric elements sized from a few to hundreds of μm. Thus, the contacts between these fabric elements (a few to hundreds of μm, including organics related microstructures, fragments of microfossils and microcrystals, in the following text abbreviated as inclusions) are primarily of influence in terms of geometry and nature. However, none of three classical contact types of clay particles in terms of geometry known as face to face, face to edge and edge to edge in non-organic soft clays applies in Dutch organic clay, because of the replacement of clay mineral microstructures with the inclusions. Meanwhile, it is obvious that an even greater important effect on the properties of clay is exerted by the nature of the contacts. Three types of contacts can thus be distinguished in terms of the nature for clay soils (Grabowska-olszewska et al, 1984): coagulation, transition and phase contacts. Coagulation contacts are characterized by the presence of a thin equilibrium film of absorbed water in the contact zone which take place in young and poorly compacted clay soils whilst phase contacts are distinguished by the presence of a new phase such as organics, silica, gypsum and carbonates etc, developed at the contacts and cementing the clay particles and microaggregates; And transition contacts fall in between. Presumably, from the point of view of the nature of the contacts, the unusual fabric of Dutch organic clay implies that the coagulation or transition contacts occurring in young non-organic clay sediments could be degraded while the phase contacts induced by the inclusions prevail.

According to the image analysis of micrographs obtained from electron microprobes, i.e. by statistically counting the pixels at a certain threshold of grey level for the recognized pores in grey graphs, the inclusions change the size and distribution of pores of this organic clay in comparison with other inorganic clays, where micro pores classified as those sized between 0.5-10 μm are common and have an isometric shape. The macro pores (>10 μm) and the micro pores (<0.5μm) which dominate the inorganic silt clay and inorganic plastic clay, respectively, are more or less missing.

5.5.3 Comparison of four fabrics: remoulded, natural, artificial inorganic and fractured

Representative ESEM micrographs of fabrics for the four ways of preparation of clay samples presented earlier, are given in Figure 5.4, at a magnification of 500 or 250 times. The differences among them are significant in terms of fabric element interaction and porosity. A regular aggregation with particle matrix, referred to as the remoulded mode (figure 5.4a) and a fractured lattice mode with local conjugate planes (indicated with a circle in figure 5.4d) can be seen, are developed from the original natural mode (figure 5.4b). The regular aggregations are more oriented in the natural than in the remoulded mode. Artificial inorganic clay (figure 5.4c) has the loosest skeletal fabric where fine particles are largely absent and the contacts of aggregations are more or less clay bridges. Correlation of the fabric with geotechnical compression behaviour in the laboratory tests indicates the skeletal fabric, i.e. the artificial inorganic fabric corresponds to the lowest shear strength because of the low strength of clay “bridges”. The natural fabric corresponds to the highest shear strength probably because of the nature of transition or phase contacts of aggregations developed. A statistical image analysis has demonstrated that the porosity of the natural fabric remains rather low at a level of 0.2 and 20μm to 50μm is a suitable scale to characterize the fabric of this clay at a microscopic level. It is more or less related to the size of silt particles, mineral-organic microaggregates and the microfossils. The less rich fraction of clay minerals such as illite and chlorite (<2um), combined with fine fractions (<2um) of organic colloid and collomorphic carbonate pieces (<2um) are presented to help form two basic microstructures, i.e. spherical and plate-like microaggregates, denoted as elementary particle aggregations shown in Table 2. EDAX results as presented in Table 2 (e) indicate different chemical element components of two microaggregates. The presence of much carbon indicates the presence of organic or carbonate-related matter, in addition to illite/chlorite clay minerals. Such an organic film is estimated to have a thickness of 90-140nm by ESEM, clothing particles and clay minerals (<2um) and may alter the charge and surface area of the particles and therefore enhance the physicochemical forces (mainly van der Waals interactions). The elementary particle aggregates may be strengthened by these physicochemical bond forces (i.e. true cohesion in the clay).

5.5.4 Idealization of fabric of Dutch organic clay :a double lattice model

The previously proposed models in literatures for characterization of young sedimentary clay fabric, such as honeycomb, matrix and laminar etc (Smart et al, 1981; Grabowska-olszewska et al, 1984; Mitchell, 1992), hardly apply to the Dutch organic clay. A mixed fabric type is found here. Reconstruction of a 3D structure of clay fabric based on 2D ESEM micrographs seems impossible due to the limitations of imaging principles of the used scanning microscopy. Instead, on the basis of the categorization of fabric elements in Table 5.2, an idealized fabric of Dutch organic clay can be obtained as shown in Figure 5.5. Consider a clay particle of $0.25mm^3$, where two types of lattices are introduced to idealize the clay fabric at primary and secondary levels. The primary lattice is made up of quartz, diatoms, inorganic carbonate microfossils and large mineral-organic aggregates. The secondary lattice (20μm) which is nested in the primary one is made of mainly two forms of microaggregates (plate-like and sphere-like), inclusions of microcrystals, organic colloid particles and carbonate flakes. Nesting is the way of linking up the two lattices with true cohesion which may come from clothing organic films, fine clay particles and collomorphic carbonates. 50-80μm is a characteristic length for primary lattice, while 20μm is characteristic for secondary lattice. Both lattices have different mechanical properties concerning stiffness and strength. The response of such a clay particle structure to external load is crucial for interpreting the complex behavior of clay from a micro-mechanics point of view. Moreover, both the improvement of existing constitutive models based on continuous elasticity and plasticity and a new generation of mathematical models for clays require a sound physical concept including a proper characterization of clay fabric.

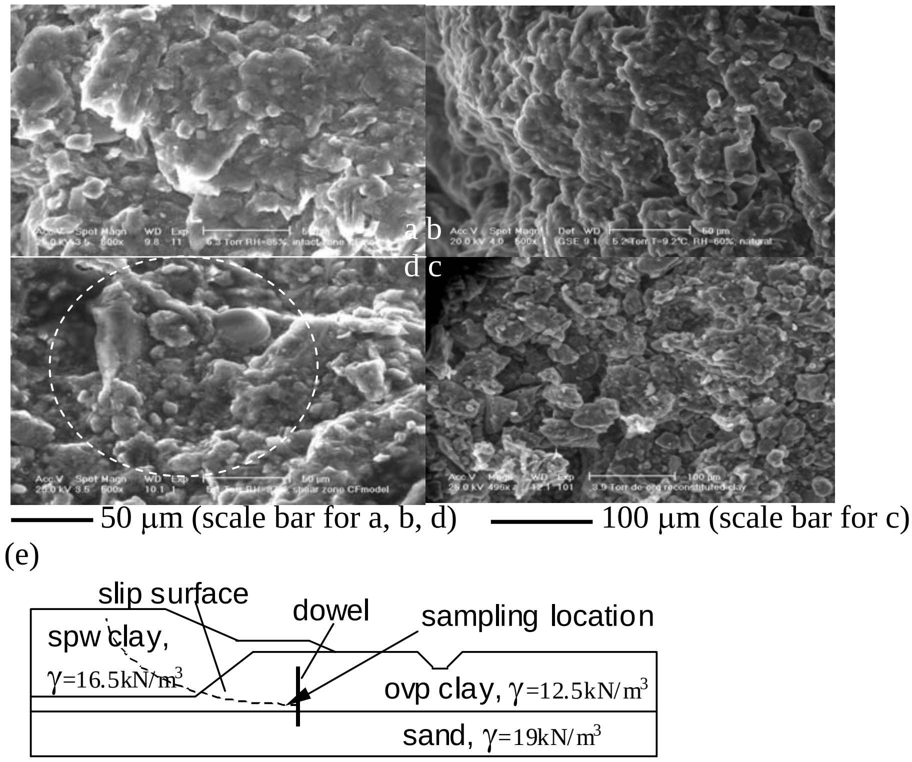

Fig. 5.4 Overview of four fabrics:
(a) remolded, (b) natural (c)artificial inorganic, (d)fractured (observation surface parallel to slip surface shown in(e), (e)the sketch of geocentrifuge modeldyke

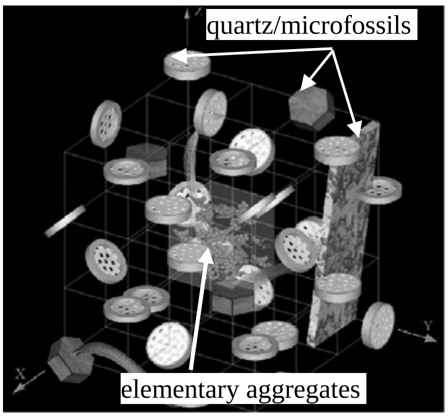

Fig. 5.5 Double lattices model for OVP clay (a clay particle of 0.25 mm^3)

5.6 Micro-deformation of fabric

Direct measurement of the mechanical properties of different fabric elements seems impossible in standard laboratory facilities. However, as mentioned above, this aspect has been advanced with a micro loading module combined with ESEM. During a micro loading test in either compression or extension, the clay fabric can be monitored and a load-displacement curve can be recorded by a load cell and by displacement transducer as indicated in Figure 5.2. To capture the micro-mechanical response of clay fabric with respect to the external load a series of uniaxial compression/extension tests were carried out in this way. Elaborated compressive stress-strain curves are presented in Figure 5.6 where natural clay samples show the highest strength and stiffness and reconstituted artificial inorganic samples the lowest. The live images of fabric change are presented in Table 5.3. Natural clay with more spherical colloid microaggregates was compressed from an axial strain of 0% to 5% while more micro-cracks (fissure-like pores) are opening up. The disconnecting or rejoining of these colloid microaggregates was achieved by rigid translation and rotation. The macro behavior of natural clay as shown in Figure 5.6 is interpreted as growth of micro-cracks and induced buckling of the surrounding microstructures at a level of about 10-20 μm. The microstructures of natural clay at a lower level (a few μm) appears unaffected by external mechanical energy. The growth and connection of the micro-cracks at a size of about 10μm appears to be forming a potential damage zone as visible in the micrographs (a) and (b) shown in Table 5.3. The mechanical behavior of natural clay should therefore be related to the fabric at a micro scale of 10 μm.

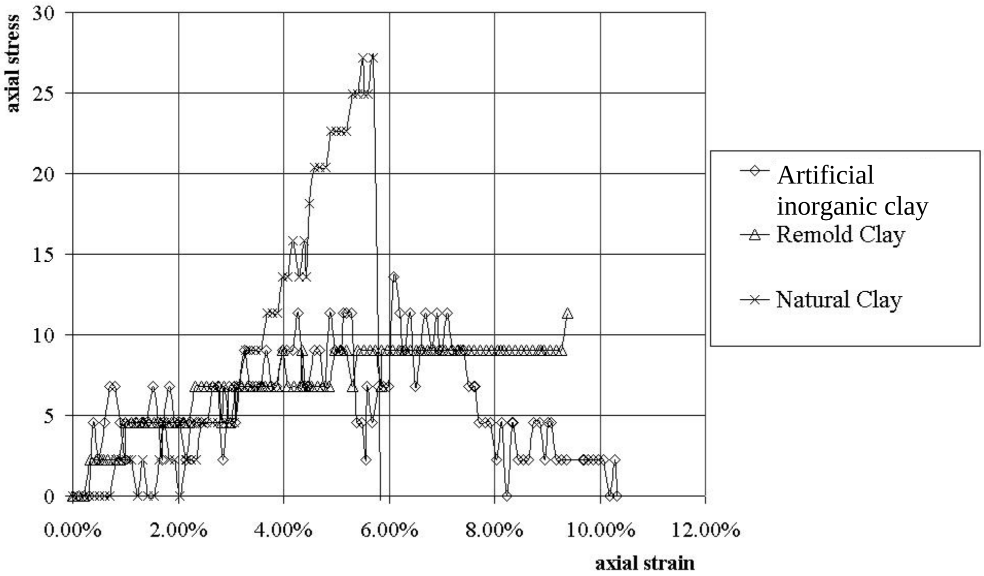

Fig. 5.6 Uniaxial micro-compression of clay

Reconstituted artificial inorganic clay with less colloid microaggregates reacts to external load in a different way. At a micro scale where silty particles of around 50 μm or less are disconnecting or rejoining, a clear localized crack occurred (80 μm in width) instead of a damage zone. In accordance, the mechanical behaviour of reconstituted clay should be related to microstructures at this level of 100 μm. Compared to natural clay response, strength and stiffness of reconstituted clay are much lower while ductility remains. It supports the idea that externally input mechanical energy is dissipated in reconstituted clay at a micro level of around 100 μm.

Table 5.3 Live micrographs and data of fabric change due to uniaxial compression

Sample	Natural clay (test: comns03)		Deorganised clay (test: comdns01)		
Conditions	Relative humidity =0.2 , Speed=2μm/sec, Compressed vertically				
Strain history	2.0%	5.0%	3.3%	5.0%	6.6%
Fabric change	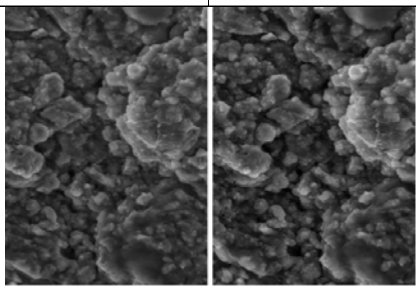 (a) (b) Image width= 112 μm		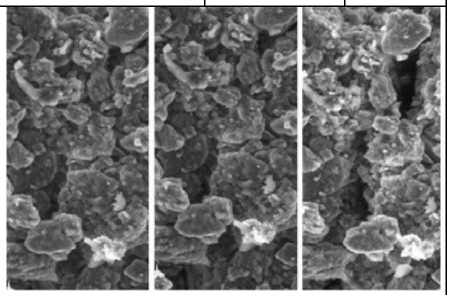 (a) (b) (c) Image width=137μm		

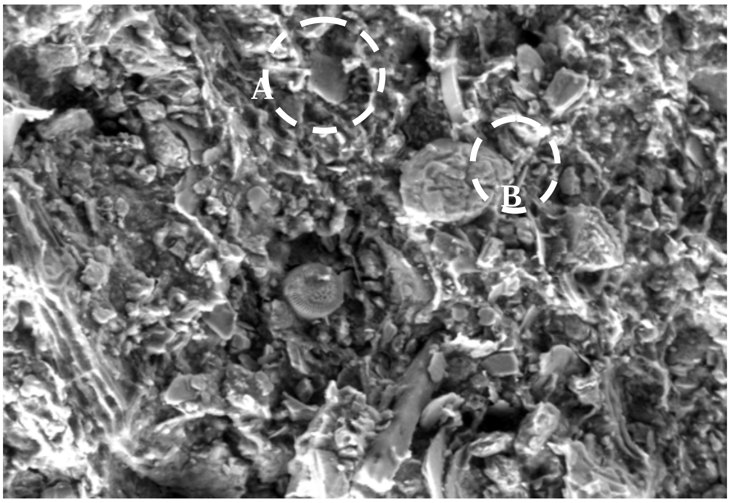

Fig. 5.7 Tension-ruptured surface of clay

(Image width=237μm, speed=2μm/sec, tensile stress=3kPa)

Concerning the role of organic matter and biological-originated carbonate flakes, the nature of contact bonds are basically changed and therefore the mechanism of energy dissipation in clay can influence the so called true cohesion. Natural clay looks stronger probably because smaller microstructures at a level of 10-20 μm are mechanically active.

The ESEM monitored extension test produced apparently an unstable response. However, the concept of relevant lattices is physically evident in the micrograph in Figure 5.7 of the tension-ruptured surface. Circle A indicates the lattices in a size of 20μm and circle B indicates the lattices of around 5μm. Identified elements forming such lattices have been summarized in Table 5.2. These lattices can be activated by an external tensile stress of around 3kPa.

5.7 Summary

Oostvaardersplassen organic clay consists mostly of microfossils, biological remains, organic colloid/tissue clothed silt particles, with the presence of less than 10% clay minerals, such as illite and chlorite. This study has shown that the organic and carbonate matter are mainly originated from estuarine suspended particles. The skeleton at a level of 50 μm to 80 μm is identified as be microfossils ($SiO_2 \cdot nH_2O$, $CaCO_3$), crystallized quartz and organic-mineral aggregates. Distributed primary particles (≤ 2 μm) or their fluctuated ball-like and flake-like microaggregates (around 20 μm), are mainly clay minerals, organic colloid and carbonate flakes, which may play the role of comment agent. The pore size distribution found suggests micro-pores (0.5 to 10 μm) are dominant in Dutch natural organic clay. This feature of fabric favours the development of capillary forces in the fabric of natural clay. Geotechnical properties of this clay are based on the particular fabric and their micro-deformation behaviour. The presence of microfossils, organic films and biological origin carbonate essentially alter stiffness and strength of fabric at a level of tens of micrometers which is responsible for micro deformation of clay.

Appendices of Chapter 5

Appendix 1 Philips XL30 Esem&Edax setup and Soxhlet extractor

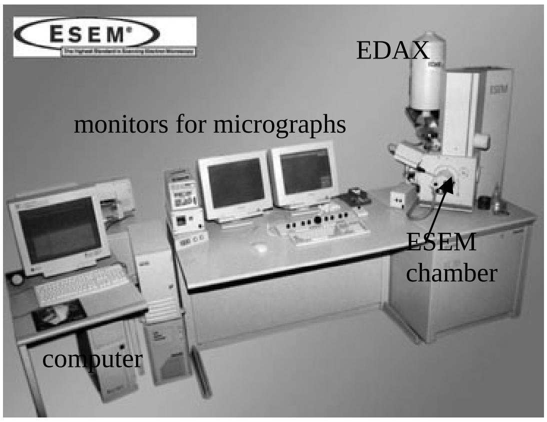

(a)ESEM&EDAX setup

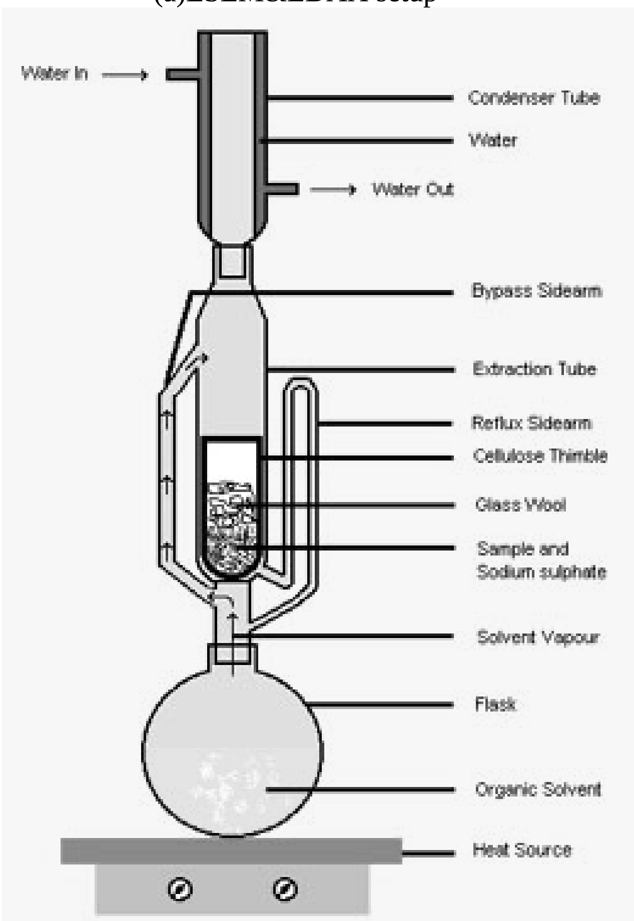

(b) Soxhlet extractor for the removal of organic matter off clay

Fig.A5.1. Philips XL30 Esem&Edax setup and Soxhlet extractor

The XL30 ESEM sets a new standard for scanning electron microscopy. Only the ESEM provides high resolution secondary electron imaging and X-ray analysis in a high pressure gaseous atmosphere such as water vapour as well as in high vacuum. Gas ionisation in the ESEM eliminates charging artefacts in both images and X-ray analysis. Chamber pressures well above 4.6 Torr (133.3 Pa) are essential requirements to keep wet and hydrated samples in their original state. A built-in source of water vapour and an auxiliary gas manifold permitting the use of a wide variety of gases in the chamber. This advanced technology allows the stable imaging of hydrated and wet samples and pure SE (Scanning Electron) imaging of non-conducting, uncoated materials, thus eliminating any need for specimen preparation.

Soxhlet extractor is used to extract the organics from clay suspension. This is a widely acceptable method in geochemical experiments. But it should be noticed that not all organics in estuarine clays can be extracted by Soxhlet. And the efficiency of this method seems lower relative to the method of centrifugation.

Appendix 2 Optical and electron microscopy of soft soils: applied techniques and examples

The collection of micrographs of Dutch organic clay from Oostvaardersplassen (OVP clay) and Spice White kaolin clay (SPW kaolin) is used to discuss the influences of a variety of techniques required including the preparation methods of sample and interpretation of micrographs. In general, the information in the captions is presented as follows: identified fabric elements, magnifications (e.g. 25M), preparation methods and discussions.

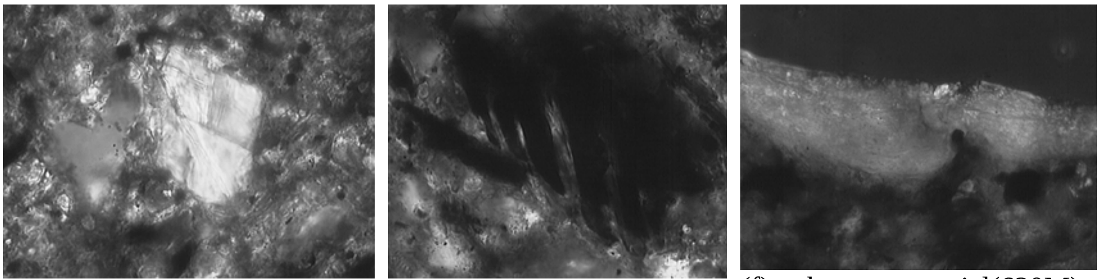

(d) calcite/dolomite (630M) (e) dark brown organic tissue(630M) (f) unknown material(630M)

Fig A5.2. Cross polarized light microscopy of OVP clay

(a) Discussion on optical microscopy :

The polarizing microscope is essentially the same as a common light microscope. The difference is that the polarizing microscope is equipped with polarizing discs above and below the microscope stage, and a means to rotate the stage to alter the orientation of the specimen with respect to the vibration direction of the polarized light. Optical features of minerals and other fabric elements, such as colours, distinction of optical intensity and twinning effects help identifications. Dark brown organic tissues are easily recognized. Some silt particles and micro-crystals can be identified too. Combined with the results of XRD, it is the first step to characterise the fabric of silty clays by obtaining optical micrographs at magnifications of 25 to 630.

(b) Discussion on electron microscopy:

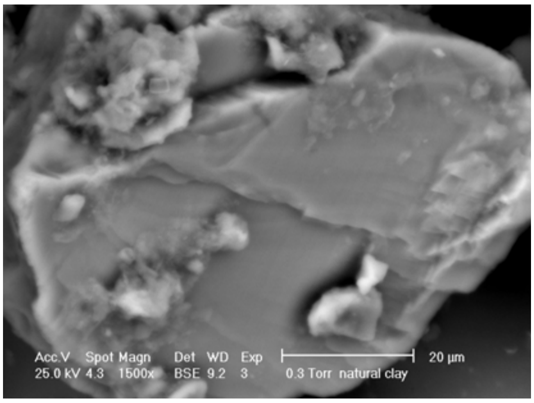

(a) organic films by BSED (Backscatterred Electrons Detector) (OVP clay)

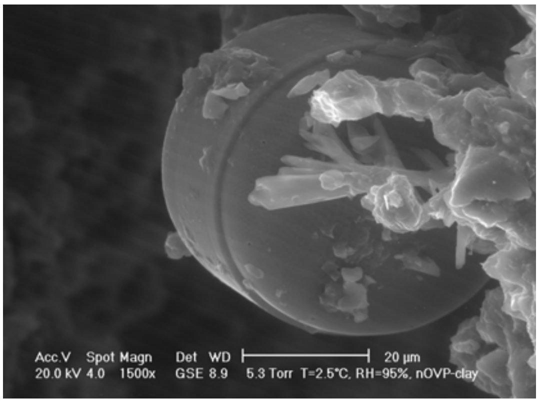

(b) interaction of microfossil and micro-crystals (OVP clay)

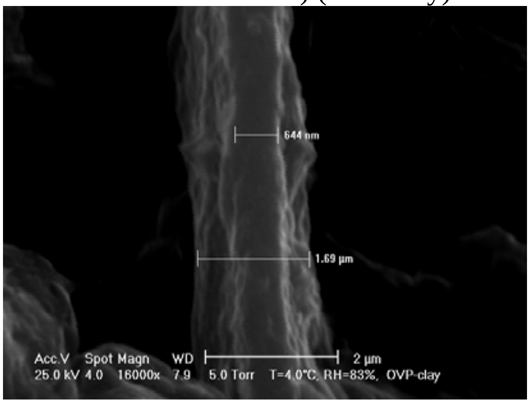

(c) high magnification and humidity mode (OVP clay)

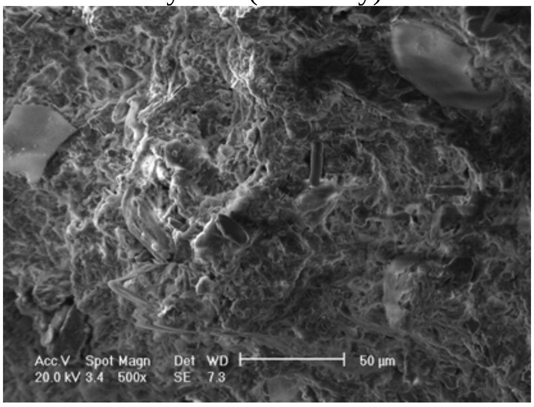

(d) SEM micrograph: high vacuum mode (OVP clay)

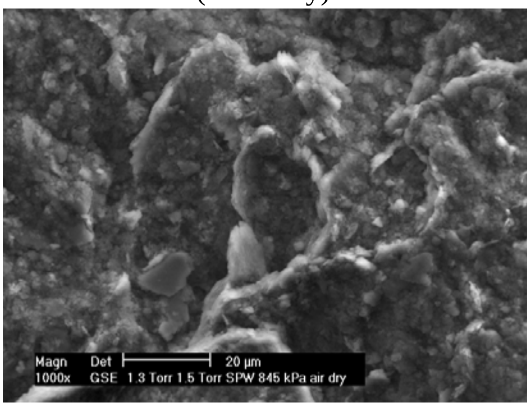

(e) consolidated SPW kaolin clay (air-dried, consolidation pressure= 845 kPa)

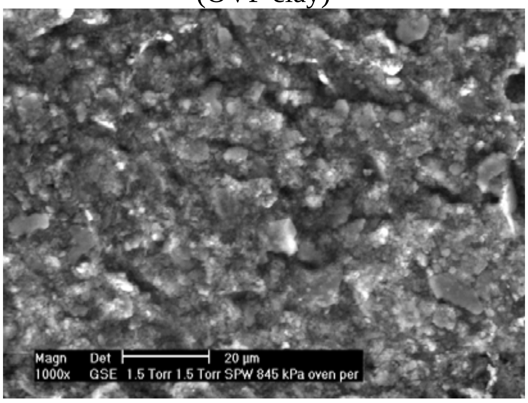

(f) consolidated SPW kaolin clay (oven-dried, consolidated pressure=845 kPa)

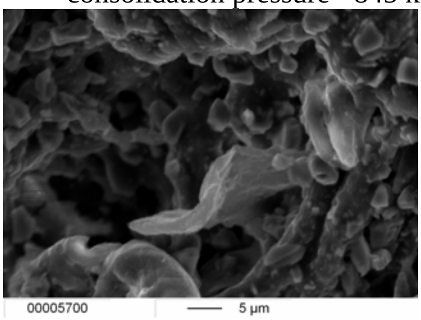

(g) Electron microprobe (JEOL 8800)

Qualitative analysis result of the sheet-like object observed in the micrograph (left): the chemical elements of it are ranked as C, O, Al, Si, S and Ca

Fig A5.3. Electron microscopy of soft clays

Identification of organic matter by ESEM is a difficult task. Sufficient amounts of carbon were detected in OVP clay, but could not be allocated. A methodical investigation combining ESEM and EDAX described as follows showed that the microstructure of the clay was covered with well-dispersed colloid film pieces of carbon-based material (Fig. A5.3(a) and Fig. A5.3(b)). Although this colloid film is penetrable for the primary electrons from the beam, information about the structure of the surface by means of secondary electrons (Gaseous Scanning Electron or Backscatter Scanning Electron) originates from the upper 10-20 nm of the surface. Therefore both BSE and GSE detectors should be attempted as the interaction of beam with organics-related microstructures is significant. Quantitative analysis of EDAX can start only from the element of carbon with respect to the chemical elements periodic table. When combined with ESEM, the effect of beam scatter reduces its accuracy too. Despite these limitations, by varying the accelerating voltage of the beam, an EDAX can be used qualitatively to determine the thickness of a layer on a substrate (Goldstein *et al.*, 1981). When a low accelerating voltage is applied, the interaction volume of the beam only interacts with the layer and doesn't reach into the substrate. The layer is mainly carbon and oxygen, while the substrate contains Si, Ca, S etc. When the voltage is increased to 2.2-2.8 keV, information from the substrate is added. Monte Carlo simulations indicate a layer thickness of 90-140 nm. This thickness is rather uniform through the sample.

The preference of environmental climates in the chamber depends on both the purpose of investigation and whether the quality of images is good. Three environmental parameters, i.e. humidity, temperature and vacuum pressure have to be set according to the three-phase graph of water. Figure A5.3 (c)-(g) illustrates the effects of different chamber climates on the qualities of images obtained. The higher vacuum and lower humidity, the higher qualities of images obtained, which, however, at the cost of more techniques of preparation of samples and more disturbances to intact fabric of clays. The artefacts induced by drying processes are demonstrated in Figure A5.3 (e) and (f). In addition, an electron microprobe is used and SEM-type micrograph (shown in figure A5.3(g)) is obtained with chemical elements analysis.

Chapter 6

Distinct Element Modelling of Fabric and Properties of Organic Clay

6.1 Introduction

The unusual fabric and its micro-deformation of a Dutch organic clay have been observed in the laboratory as explained in Chapter 5. The fabric of this clay is believed to be responsible for specific geotechnical behaviour that can not be understood in the framework of classical soil mechanics (Chapter 5). In order to gain an insight in the correlation of fabric with geo-mechanical behaviour, the distinct element modelling (DEM) is applied where a clay sample is described by an assembly of distinct cohesive particles. The chosen code is PFC2D which can perform two dimensional analyses (Itasca Inc, GeoDelft licence). Additional routines were programmed to be able to model the typical clay fabric.

Numerical simulations of soil fabric with DEM have been carried out in the past (Pruiksma, 2002; Van Baars, 1996; Robertson & Bolton, 1999), but mainly for sand and sandstone rather than clay. Pruiksma (2002) has investigated with PFC2D the biaxial behaviour of a non-cohesive material paying much attention to the study of micro strength and stiffness parameters. Van Baars(1996) demonstrated with the code Grain that a shear band appearing in a cohesive and granular sample, e.g. sandstone, was due to the growth of micro-cracks, i.e. the broken contacts between the particles. The contacts broke up because of tensile failure rather than shear failure and particles inside the shear band were observed to rotate subsequently. Robertson and Bolton (1999) have simulated crushable grains where regular 0.5mm-sized agglomerates of bonded elementary spheres were generated by using the cluster option implemented in code PFC3D. The size effect such as the percentage of initial flaws and crushability of regular agglomerates was well observed regarding its correlation with splitting strength. They have initiated the study of the influence of fabric on soil behaviour by the distinct element method (DEM). However, as Bolton mentioned (1999), their approach was not so meaningful for clay since there were no imaging facilities available at that time for live observation of the change of clay microstructure under load. In the present study these drawbacks have been overcome to some extent. Environmental Scanning Electron Microscopy (ESEM) tests (Chapter 5) form the experimental basis for this numerical study and the use of DEM is shown to be meaningful.

The main objective of this approach is to determine the influence of clay fabric consisting of strip-like and flake-like microstructures and micro-fibres on the behaviour of biaxial compressions. The calculations are then performed for cohesive materials. Therefore, the contact behaviour of the distinct particles includes bonding. Both strength characteristics and deformation mechanisms are concerned. Micro-mechanical parameters for strength and stiffness are determined by simulating a ‘basic sample' which represents remoulded clay. The sample structure is composed in a consistent random fashion by the computer model and 30 basic realizations are considered. Further calculations are carried out to investigate the role of the three microstructures aforementioned. The 'fabric sample' in which certain microstructures are therefore implemented are generated on basis of the 'basic sample'. The role of the microstructures is investigated by following the biaxial compressions of the 'fabric sample'.The deviation of strength and deformation characteristics of 'fabric samples' from those of 'basic samples' is studied. The mechanism is analysed based on statistical numerical results.

6.2 Constitutive models for bonding

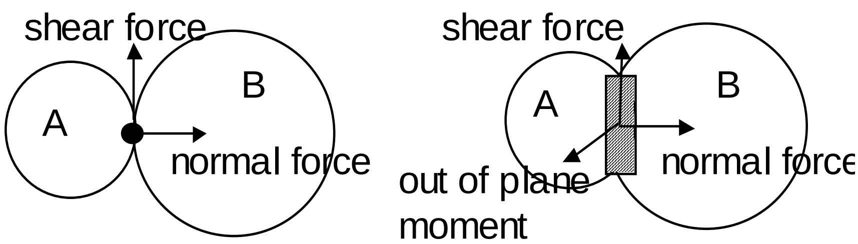

(a) contact bond (b) parallel bond

Fig.6.1. Constitutive models for bonding applied in DEM

The distinct element code PFC2D is capable of describing the movements of particles in an assembly under influence of external forces and inter-particles forces in two dimensions. The particles are presented as discs of unit thickness. All discs flow by following the second law of Newton. Disc contacts result in inter-particle normal and shear forces. The normal forces are determined by particle overlapping and shear forces are determined by the relative rotation of each pair of discs. PFC2D allows particles bonded together at contacts in case of modelling cohesive samples. Two constitutive models for bonding are used, i.e. contact bond and parallel bond models. A contact bond can be envisioned as a pair of elastic strings (or a point weld, see Fig. 6.1(a)) with constant normal and shear stiffness acting at the contact point. The magnitude of the shear contact force is limited by the given shear contact bond strength, as is the normal contact force. But a tensile contact force is allowed to develop at the bond-contact as well. If the magnitude of the tensile normal contact force equals or exceeds the normal contact bond strength, the bond breaks and both the normal and shear contact forces vanish. However, if the bonds break due to shear, contact forces remain such that the shear force doesn't exceed the friction limit. The parallel bond model describes the constitutive behaviour of a finite-sized piece of cementation deposit between particles as shown in Fig. 6.1(b). Apparently moments can be transmitted between particles by parallel bonds. The corresponding normal and shear stresses in the bond periphery are calculated via elastic beam theory.

6.3 Preparation of distinct numerical cohesive samples

By using the embedded FISH language of PFC2D, some routines have been programmed to create (1) homogeneous cohesive samples, denoted as “basic samples”; (2) two or more clustered-discs cohesive samples, denoted as “fabric samples”. To generate basic samples, a 4-walls bounded area as large as the sample size is made where all discs are randomly generated with initially a smaller average radius. The required porosity determines the total number of discs generated in this step providing the distribution of disc size is given. Following a procedure of ‘radius expansion’ the assembly of discs with the correct average radius has to be brought to the initial conditions, i.e. a homogeneous stress distribution is introduced. The initial stresses have to be as low as possible, which is required for the simulations. Fig. 6.2(a) demonstrates how a homogeneous basic sample looks like in terms of inter-discs contact force distribution. The dark lines among discs (shown in light grey balls of the picture) represent contact links whose thickness is proportional to the magnitude of initial contact force. The dark grey balls are representing those floating discs with less contacts to the surroundings.

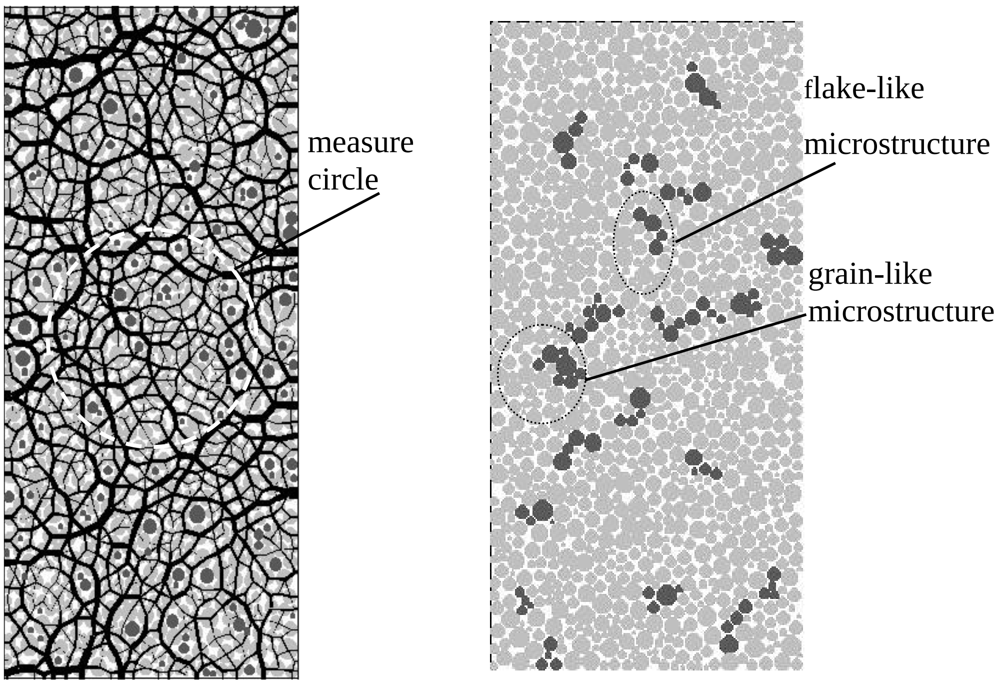

(a)basic sample (b) fabric sample

Fig. 6.2. Sample preparation for DEM

To model representative microstructures of clay observed in the micro-lab studies, clusters of 2 or more particles are generated. The clusters shown in dark grey in Fig. 6.2(b) are groups of particles that are physically and geometrically similar to microstructures in reality. The two elementary microstructures, i.e. grain-like and flake-like types, are represented by different shapes of clusters, respectively, shown in Fig. 6.2(b). In addition, fibre or film microstructure could be modelled as well provided that the corresponding physical and geometrical parameters are consistent.

Table 6.1 Parameters for cohesive samples generated with the PFC2D

parameter	basic sample	fabric sample	
radius (μm)	minimum: 25(min.) mean: 55 maximum: 85(mean) uniform distribution	minimum: 25(min.) mean: 55 maximum: 85(mean) uniform distribution	
mean porosity	0.17	0.17	
sample size(mm)	2.5*5.0 (1091discs)	2.5*5.0 (1091discs)	
disc stiffness (MPa)	8 (shear, normal)	within cluster	0.8 (shear, normal) or 8
		outside cluster	8 (shear, normal)
contact bond strength(tensile, shear) (kN)	8 (mean value), 1 (standard deviation), normal distribution	within cluster	30 (mean value),
		outside cluster	8 (mean value),
contact bond stiffness(normal ,shear) (MN/m)	0.8 (normal stiffness) 0.5 (shear stiffness)	0.8 (normal stiffness) 0.5 (shear stiffness)	
parallel bond strength(tensile ,shear) (kPa)	8 (mean value),1 (standard deviation), normal distribution	within cluster	30 (mean value)
		outside cluster	8 (mean value)
parallel bond stiffness (MPa/m)	0.8 (normal stiffness) 0.5 (shear stiffness)	0.8 (normal stiffness) 0.5 (shear stiffness)	
disc friction coefficient	1.3 (applied when bond breaks)	1.3 (applied when bond breaks)	
wall friction coefficient	0.6 (rough boundary at top and bottom)	0.6 (rough boundary at top and bottom)	

6.4 Evaluation of micro-parameters

There are a dozen micro-parameters to determine in order to conduct a numerical simulation. The effects of the micro parameters on macro behaviour have to be studied in order to gain insight into the distinct element system. It has always been one of the most difficult problems in distinct element modelling that an event can take place in a probabilistic way, and especially that some parameters are physically undetermined. Moreover micro parameters of stiffness and strength are responsible for either macro strength or deformation characteristics. By fitting the micro-uniaxial compression tests as aforementioned in Chapter 5 relevant parameters are determined

(Table 6.1). During this process of parameter evaluation the rule that numerical samples resemble clay sample in terms of peak strength and strain of uniaxial compression is ensured. Basic samples resemble remolded clay with lower strength of uniaxial compression while fabric samples resemble natural clay with higher strength. Concerning the choices of stiffness of individual balls and bonds, the single-mineralogical particle crushing test performed by Nakata et al. (1999) is also considered. For 2 mm-quartz particles and feldspar particles, they measured a normal stiffness of 2 MN/m and 0.5 MN/m, respectively.

6.5 Modelling of uniaxial compression

The simulation of uniaxial compression is performed by adjusting the boundary condition, i.e. movement of walls. The laterally supporting walls are released and the top and bottom ones are set to move closer at a constant velocity approaching a prescribed displacement. Stress and strain of sample are measured within the circular area shown in Fig. 6.2(a) in the central part by averaging the resulting contact forces and displacements of each disc.

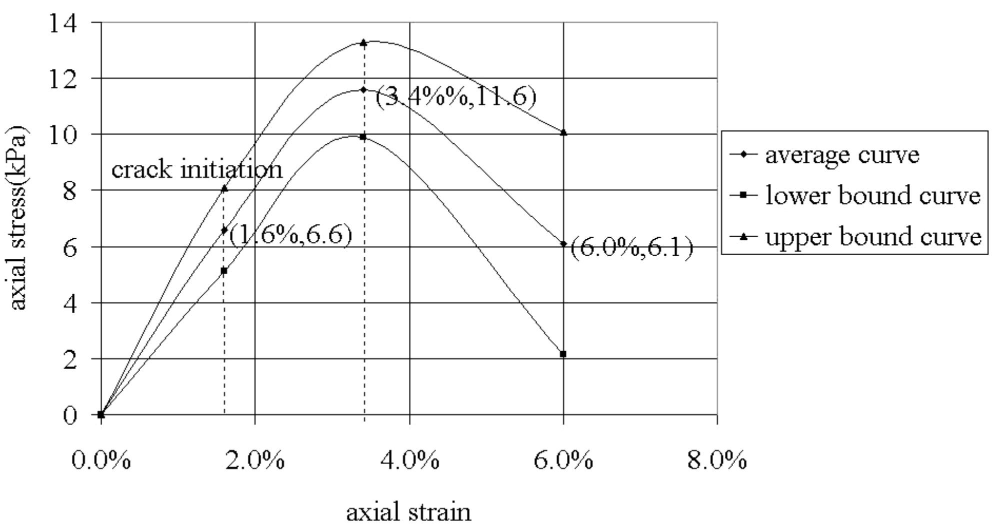

(a) stress-strain relationship

Fig.6.3. Uniaxial compression of basic samples

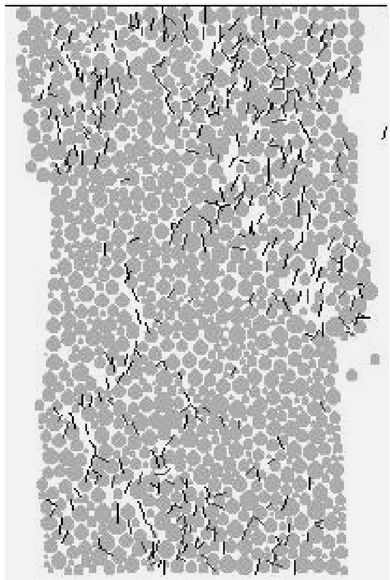

(b) micro-cracks (Sample No.14, at the strain of 8%)

Fig.6.3. Uniaxial compression of basic samples

6.5.1 Uniaxial compression of basic samples

The 30 basic samples have on average the same mean parameter values. Variation in the behaviour is related to the micro-geometric difference. All 30 samples are then uniaxially compressed in order to observe variation in the behaviour. Elaborated stress-strain curves are schematically reproduced in Fig. 6.3(a) showing pre-peak, peak and post-peak regimes. Initially negligible variation in microstructure becomes significantly amplified, in particular at the regime of post peak strength. A micro-crack is defined in the simulation as a broken bond due to either tension or slip failure. The first micro cracks always take place at the lateral boundary of samples where certain discs are less connected to others than on average. These less connected discs are squeezed out and the adjacent microstructures are affected subsequently. It is the moment when cracks initiate as indicated in Fig. 6.3(a). As the amount of micro cracks increases to about 4% of the total bonds the axial stress reaches its peak. The bond strength turns out to be lower than peak strength of samples but larger than the stress for initiation of micro cracks. When 13% bonds are broken in the micro cracks the stress drops by almost half whereas the strain has developed up to 6%. The corresponding deformation patterns at a macro level are variable. The diffused crack pattern has developed to localized shear bands as demonstrated in Fig. 6.3(b). Most of micro cracks orient vertically. This parameter study has shown that micro-mechanical parameters for bonds play a central role in the overall unaxial compression.

6.5.2 Uniaxial compression of fabric samples

Fabric samples containing strip-like or flake-like microstructures are stronger than the basic samples in terms of compressive strength. The extent to which the strength can be increased depends strongly on the content of the two microstructures rather than on other factors, such as type of microstructure or fabric anisotropy. The various effects are discussed next.

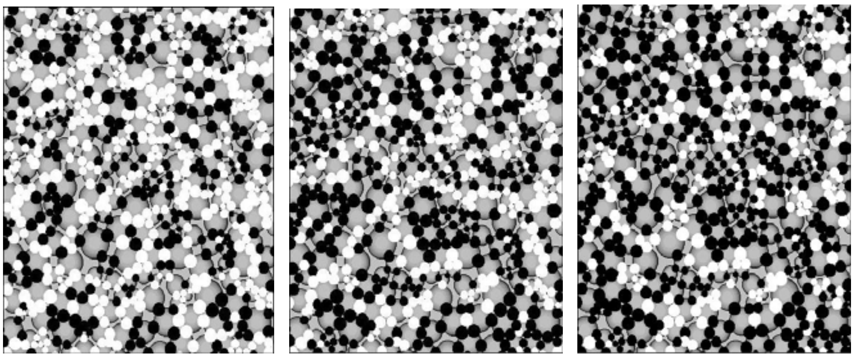

45% content 55% content 75% content

Legend: black dots: high strength bonds
White dots: normal bonds dark grey circles: discs

(a) images of content and distribution of high strength bonds

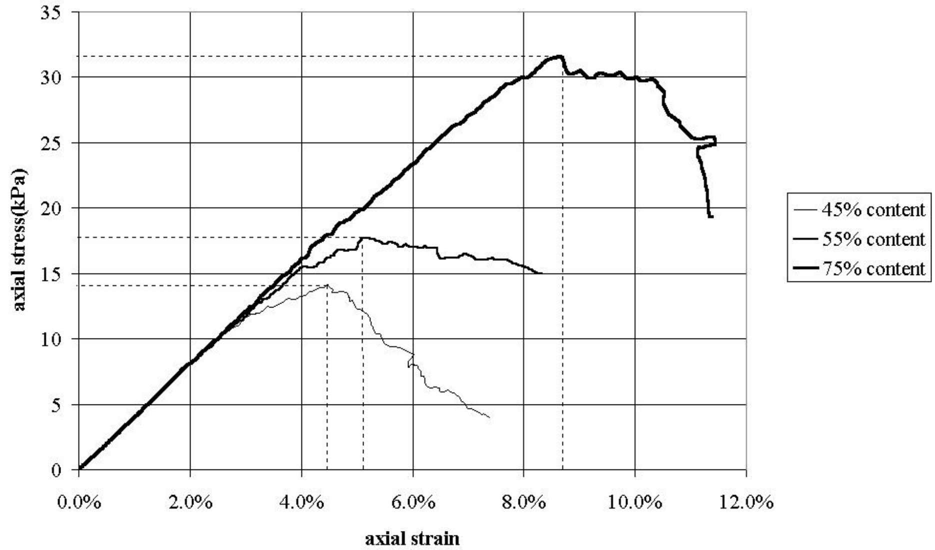

(b) comparison of fabric samples with variable contents of high strength bonds

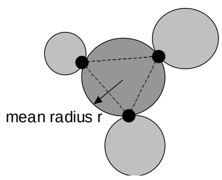

(c) characteristic length $r\sqrt{3}$ in dash line

Fig. 6.4. Uniaxial compression of fabric samples

(a) High strength bonds

The content of the two microstructures, i.e. strip-like or flake-like in a sample implies how many bonds are of high strength (30kN or 30kPa as referred to Table 6.1). The more bonds of high strength (dark dots in Fig.6.4(a) in a representative area of sample) the higher the strength of uniaxial compression is, as shown in Fig.6.4(b). It is noticed that the strength does not significantly increases unless the content of bonds of high strength reaches a certain level, e.g. 45%. This implies that the spatial distribution of the high strength bonds has to reach such a level that the mechanism of micro cracks propagation becomes active. The spatial distribution density of high strength bonds reaches maximum in case of 100% content of high strength bonds, which can be alternatively characterized by a mean radius of discs-related length ($r\sqrt{3}$)as illustrated in Fig. 6.4(c), where the number of contacts per disc is assumed to be equal to 3. For the purpose of simplification, this characteristic length (l_c) has been estimated for the three fabric samples in Fig. 6.4(a) as $r\sqrt{3}/0.45$, $r\sqrt{3}/0.55$ and $r\sqrt{3}/0.75$, respectively. The apparent peak strength of fabric samples can be conceived as an adaptation of the peak strength of basic samples by accounting for the internal characteristic length, expressed in the following empirical formula.

$$S_{fabric} = S_{basic}(C_{high} / C_{low})(\sqrt{3}r / l_c)^{2-\sqrt{3}r/l_c} \tag{6.1}$$

where, S_{fabric} is the peak strength of fabric samples; S_{basic} the peak strength of basic samples; C_{high} or C_{low} the strength of high or low strength bond; l_c the internal characteristic length; r the mean size of discs. Exponent 2 represents a regression coefficient with a 10% error.

(b) Fabric anisotropy

The anisotropy of the sample has been investigated in order to define its influence on the overall strength. Two numerical simulations were chosen of flake microstructures in which 2 discs are clustered with a high strength bond (in black), and in which the mean orientations of the microstructures with respect to the horizontal direction are 22.5 degrees and 67.5 degrees in Fig. 6.5(a) and Fig. 6.5(b), respectively. The calculations reveal that the anisotropy is not significant, as shown in Fig. 6.5(c), when 20% of total bonds are belonging to flake-like microstructure. This content can not be increased much more as otherwise the orientation of these microstructures is lost. It is observed that the sample with horizontally oriented fabric fails in a more brittle way than the one with vertically oriented fabric, in particular after softening occurs, shown by point A in Fig. 6.5(c). This coincides with the preference of vertical micro cracks as observed in the basic samples and it is related to the loading system (vertical compression). It is evident that anisotropy of fabric leads to different post peak behaviour.

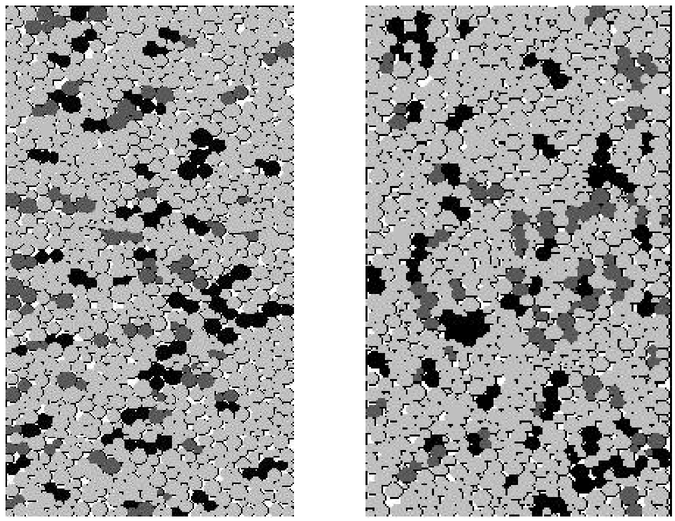

(a) horizontally oriented fabric (b) vertically oriented fabric

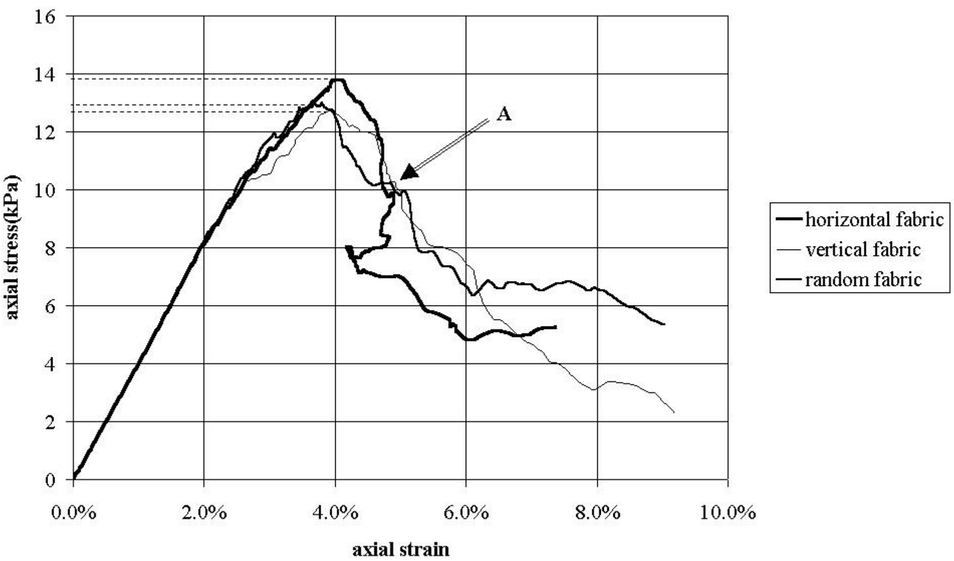

(c) fabric-induced anisotropy of strength

Fig. 6.5. Fabric anisotropy and sample strength

(c) Fibre

Since some fibres of biological origin were found in Dutch organic clay, its role in determining strength of sample is of concern. The fibre elements with an average slenderness of 4 as shown in Fig. 6.6(a) are added into basic samples with a content of 20%. The fibre elements are implemented as four discs bonded together with high tensile strength of 30 kPa and two type of stiffness are considered. Fibres provided with higher stiffness than surrounding discs, called stiff fibres, reinforce the sample. Fibres provided with lower stiffness than surrounding discs, called soft fibres, weaken the sample (see Fig. 6.6(c)). This approach is basically different from what has usually studied in the finite element analysis, i.e. fibre elements always strengthen samples no matter what stiffness. To explain the effect of the stiffness of fibres a local part of sample including a fibre has been examined. In case of stiff fibre this local part will become stronger and stiffer under the longitudinal extension (F1) and not be much influenced in terms of strength under the transversal extension (F2). Meanwhile, if soft fibre is present the sample could become stronger but more flexible under the transversal extension (F2), and may not be influenced under the longitudinal extension (F1). In conclusion the mechanical behaviour of fibre-reinforced soil depends on fibre structure, i.e. stiffer, orientation and loading conditions.

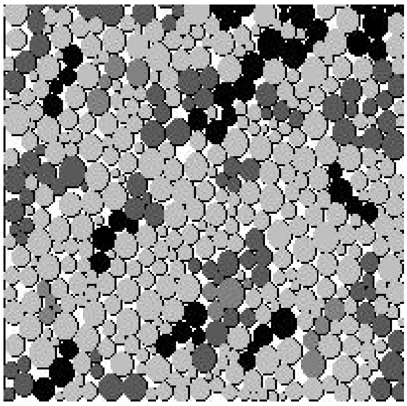

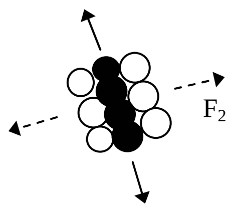

(a) fibre elements in black or dark blue (left)

(b) a local part of sample with a fibre (right)

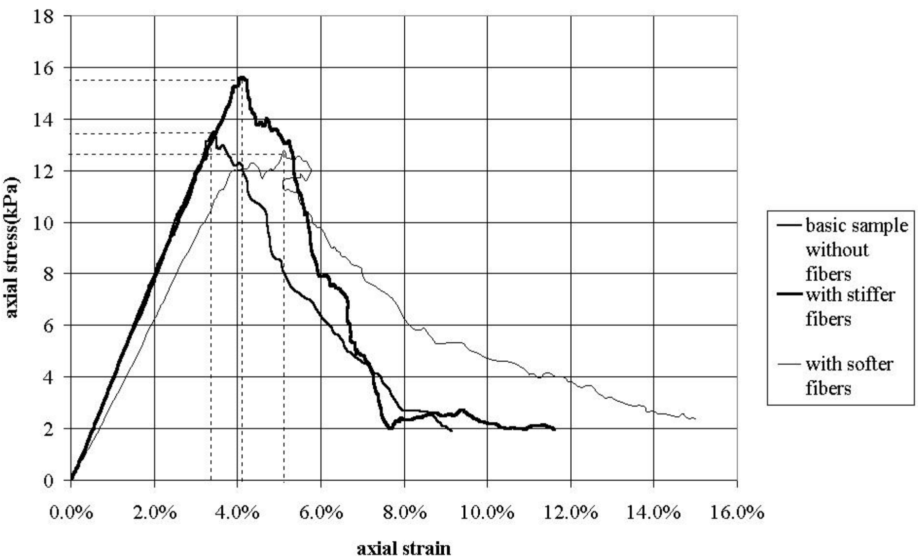

(c) influence of fibre stiffness on sample strength

Fig.6.6. Fibre and sample strength in DEM

6.6 Modelling of confined compression

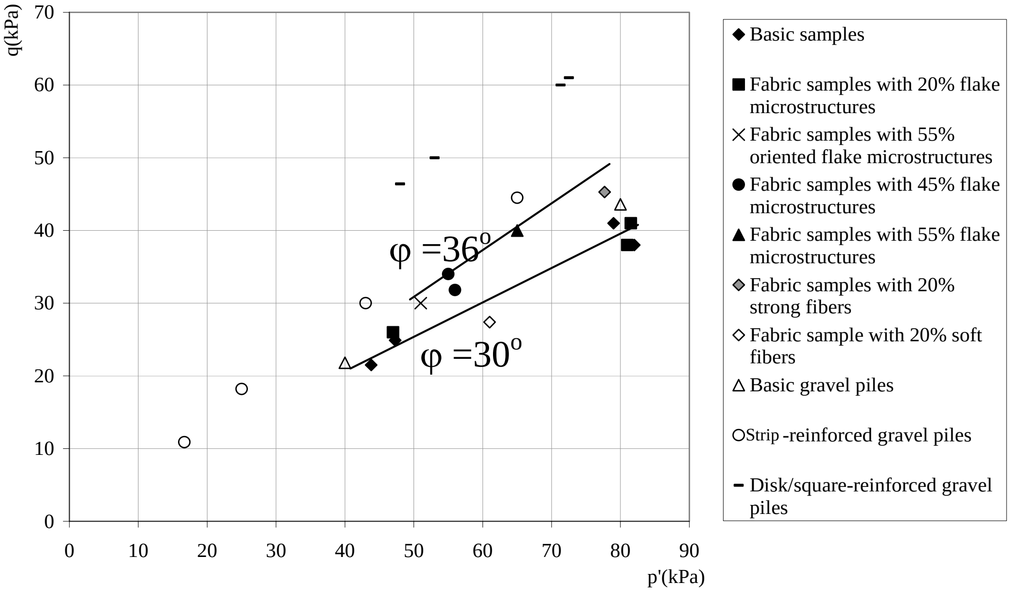

Fig.6.7.Numerical investigation of the compressive strength of confined samples

By supporting the sample with two side walls the confined compressive tests applied for both basic and fabric samples indicate a significant increase of internal friction angles from $\varphi' = 30^0$ to $\varphi' = 36^0$, shown in Fig. 6.7. Besides the nature of bonds, i.e. the strength and stiffness, the content of those bonds do play a role as found for the unconfined compressive strength of samples. This result complies with the effect of reinforcement applied in gravel pile tests (Brinkman, 1992), where a disc or square-like textile flakes rather than strips appeared to be most effective in raising φ'. Brinkman's physical test results are scaled down in terms of confining pressure and added in Fig 6.7 as well for a purpose of comparison.

6.7 Miscellaneous fabric-related concepts at various scales

The present study with DEM focussed on the mechanical effect of clay fabric at micro-scale (micrometers). Based on observations in dynamics the strength and stiffness parameters of bonds and discs as estimated and evaluated are significant at this level. Studies of clay fabric at a nano-scale (nanometers) are commonly used to investigate the nature of contact forces. Clay particles in these studies are needle-like and therefore depend on strong physicochemical forces (hundreds to thousands kPa). Bending forces generated among those needle-like particles are important as well. In such nano-structures the concept of the parallel bond or contact bond is not significant. The present study has shown that the overall strength depends on micro behaviour at micro level, not at nano level. Apparent cohesion, one of the geotechnical properties of clay, is found to be scattered between 8 kPa and 30 kPa with DEM, which is dependent on fabric at micro level. The number and distribution of bonds of high strength are dominating in unaxial compression strength. Fabric anisotropy is of secondary importance, and it is sensitive to the stiffness characteristics of the micro system. The micro deformation mechanism that causes a sample to fail can be described as initiation of slip or tensile cracks–cracks propagation due to internal buckling of microstructure, once a kinematically admissible macro pattern has formed (shear band, diffused cracks, buckling). However, such a deformation process is statically variable and therefore it alters the peak strength and post-peak behaviour.

6.8 Bond, porosity and suction effects at micro-level

Shown by numerical simulations and micro-deformation observations the bonds or secondary lattices dominate the mechanical behaviour of clay. The strength of the secondary lattice, i.e. 1 to 50 μm primary particles and microaggregates in Dutch organic clay, is increased due to the enhancement of physicochemical forces. The nature of these “bonds” has been evolving with the process of estuarine lithification where a transitional or even phase contact type is detected instead of coagulation type known in young clay sediments. According to the estimation made by Grabowska-Olszewska et al. (1984) the strength of bonds can be increased from an order of 10 kPa for a coagulation bond to an order of 1MPa at transitional/phase bond. Moreover, the stiffness of the bonds varies as a result of the composite bonds present in Dutch organic clay, i.e. clay mineral-organic-microcrystrals bonds (stiff or soft). Such high strength and composite bonds characterize the unusual fabric of Dutch organic clay at a micro-scale level. The porosity and water content of Dutch natural organic clay increases whilst the bulk density decreases and the content of porous microfossils, organic debris and microcrystalls increase. However, the pore size distribution found suggests micro-pores (0.5 to 10 μm) are dominant in Dutch natural organic clay. This feature of fabric allows pore water matrix suction in natural clay samples. It has been proved in the laboratory.The matrix suction in natural clay samples (3cm in diameter and 6 cm in height) with a bulk density of 1.36 to 1.38 g/cm^3 rises up to 15 kPa in a period of 120 to 150 hrs. Therefore, the presence of an extra bounded water film in ultra pores (nano-pores) in inorganic clays has been disregarded. Instead, the capillary forces in micro-pores in Dutch natural organic clay are significant and they increase both cohesion and friction. The more micro-pores (or water content), the more increase of strength.

6.9 Summary

A numerical approach (DEM) for distinct granular particles is applied to correlate observed fabrics and macro-mechanical properties of clay. Clay fabric has hitherto been predominantly studied at the nano-scale. A sound explanation of macro-scale behaviour from nano-scale observation is however not available. This study proves that a sound relation between fabric and common geotechnical properties of clay can be formed from micro-scale (micrometers) studies. An explanation from a micro-mechanical point of view is made for unusual mechanical properties of Dutch organic clay by accounting for the high strength and composite micro-bonds as observed and modelled, and the matrix suction developed in micro-pores. Such a micro-scale approach is also essential for the study of mechanical behaviour of modified or contaminated clay.

References (Chapters 1,2,3)

Arthur, J.R.F., Chua, K.S., Dunstan, T., and Rodriguez, J.I. (1980) Principal stress rotation: A missing parameter. *Journal of the Geotechnical Engineering Division,* Vol.106, No. GT4, p:419-433.

Arthur, J.R.F and Dunstan, T.(1982) Ruptured sand sheared in plane strain. *Proceedings of IUTAM conference on deformation and failure of granular materials*, Delft, Balkema, Rotterdam, p:453-459.

Arthur, J.R.F., Dunstan, T., Al-Ani, Q.A.J.L. and Assadi, A.(1977) Plastic deformation and failure in granular media. *Géotechnique* 27, No.1, p:53-77.

Bishop, A.W.(1954) The use of the slip circle in the stability analysis of slopes. *Géotechnique* 5, No.1, p:7-17.

Bishop, A.W. and Green, G.E. (1965) The influence of end restraint on the compression strength of a cohesionless soil. *Géotechnqiue* 15, No.3, p:243-266.

Bjerrum, L. (1967) Progressive failure in slopes of overconsolidated plastic clay and clay shales. *J. Soil Mechs. Found. Div., ASCE*, Vol. 93, No. SM5, p:3-49.

Bolton, M.D.(1986) The strength and dilatancy of sands. *Géotechnique* 36, No.1, p:65-78.

Brace, W.F. and Martin, R.J. (1968) A test of the law of effective stress for crystalline rocks of low porosity. *Int. J. Rock Mech. & Min. Sci*, Vol. 5, p:415-426.

Castro, G. (1969) *Liquefaction of sands*, PhD Thesis, Harvard University, Cambridge, Mass.

Chen, W.F.(1975) *Limit analysis and soil plasticity*, Elsevier PC.

Cheng, X., Den Haan, E.J. and Barends, F.B.J.(2001) Laboratory and numerical investigations of triaxial compression behaviour of a Dutch sand. *GeoDelft Report*.

Cheng, X., Den Haan, E.J. and Barends, F.B.J. (2003) Revisit dilatancy and failure of sand in routine triaxial compression (Part I): Experimentation and modelling. *Proceedings of the 2003 International Conference on Computational and Experimental Engineering*, Herrera, C.A. (ed.), Corfu, Greece.

Cheng, X., Den Haan, E.J. and Barends, F.B.J. (2003) Revisit dilatancy and failure of sand in routine triaxial compression (Part II): Limit analysis on failure mechanism, *Proceedings of the 2003 International Conference on Computational and Experimental Engineering*, Herrera, C.A. (ed.), Corfu, Greece.

De Josselin de Jong, G.(1971) The double sliding, free rotating model for granular assemblies. *Géotechnique* 21, p:155-163.

De Josselin de Jong, G. (1988) Elasto-plastic version of the double sliding model in undrained simple shear test. *Géotechnique* 38, No. 4, p:533-555.

Desai,C. S. and Faruque, M.O. (1984) Constitutive model for geological materials. *Journal of Engineering Mechanics Division*, ASCE, 110, No 9, p:1391-1408

Desrues, J., Chambon, R., Mokni, M., and Mazerolle, F. (1996) Void ratio evolution inside shear bands in triaxial sand specimens studied by computed tomography. *Géotechnique* 46, No. 3, p:529-546.

Drescher, A. and Vardoulakis, I. (1982): Geometric softening in triaxial tests on granular material. *Géotechnique* 32, No. 4, p:291-303.

Finno, R.J., Harris, W.W., Mooney, M.A. and Viggiani, G. (1996) Strain localizaition and undrained stready state of sand. *J. Geotech. Engng., ASCE,* 122, No. 6, p:462-473.

Frank, F.C. (1965) On dilatancy in relation to seismic sources. *Review of Geophysics,* Vol. 3, No. 4, p:485-503.

Gutierrez, M. and Ishihara, K. (2000) Non-coaxiality and energy dissipation in granular materials. *Soils and Foundations*, Vol. 40, No. 2, p:49-59.

Han, C. and Drescher, A. (1993) Shear bands in biaxial tests on dry coarse sand. *Soils and Foundations,* Vol 33, p:118-132.

Han, C. and Vardoulakis, I. (1991) Plane-strain compression experiments on water-saturated fine-grained sand. *Géotechnique* 41, No. 4. p:49-78.

Hettler, A. and Vardoulakis, I. (1984) Behaviour of dry sand tested in a large triaxial apparatus. *Géotechnique* 34, No .2, p:183-198.

Hill, R. (1962) Acceleration waves in solids. *J. Mech. Phys. Solids* 10, p:1-16.

Hill, R. (1958) A general theory of uniqueness and stability in elastic-plastic solids. *J. Mech. Phys. Solids* 6, p:236-249.

Houlsby, G.T. and Wroth, C.P. (1980) Strain and displacements discontinuities in soil. *J. Eng. Mech. Div. 10b,* No. EM4, p: 753-771.

Ishihara, K. (1993) Liquefaction and flow failure during earthquakes. *Géotechnique* Vol. 43, No. 3, p:351-415.

Jakobsen, K.R., Praastrup, U. and Ibsen, L.B. (1999) The influence of the stress path on the characteristic stress state, *Pre-Failure Deformation Characteristics of Geomaterials*, Jamiolkowski et al. (eds), Balkema, Rotterdam.

Lade, P.V. and Pradel, D. (1990) Instability and plastic flow of soils. I: Experimental observations, *Journal of Engineering Mechanics*, Vol.116, No.11, p:2532-2550.

Lee I.K. (ed) (1968) *Soil mechanics(selected topics)*. Butterworths.

Luong, M.P.(1982). Stress-strain aspects of cohesiveless soils under cyclic and transient loading. *Proceedings of International Symposium on Soils under Cyclic and Transient Loading*, p:315-324, Swansea.

McDowell, G.R. and Bolton, M.D. (1998) On the micro-mechanics of crushable aggregates. *Géotechnique* 48, No. 5, p:667-679.

Mokni, M. (1992) Relations entre déformations en masse et déformations localisées dans les matériaux granulaires. PhD Thesis, University of Joseph Fourier-Grenoble 1.

Molenkamp, F. & Luger, H.J. (1981) Modelling and minimization of membrane penetration effects in tests on granular soils. *Geotechnique* 31, No. 4, p:471-486.

Molenkamp, F. (1985) Comparison of frictional material models with respect to shear band initiation. *Géotechnique* 35, No. 1, p:17-34.

Molenkamp F.(1998) Principle of axial shear apparatus. *Géotechnique* 48, No. 3, p:427-431.

Molenkamp, F. (1991) Material instability for drained and undrained behaviour Part 2: Combined uniform deformation and shear-band generation. *Int. J. Numerical and Analysical Methods in Geomechanics,* Vol. 15, p:169-180.

Molenkamp, F. (1991) Material instability for drained and undrained behaviour Part 1: Shear band generation. *Int. J. Numerical and Analysical Methods in Geomechanics*, Vol. 15, p:147-168.

Molenkamp, F. (1989) Liquefaction as an instability. Report of Int. Soc. Soil Mech. Found. Eng. ISSMFE technical committee on Mechanics of Granular Materials, to 12th Int. Conf. Soil Mech. Found. Engng. ICSMFE, Rio de Janeiro, p: 157-163.

Mooney, M.A. and Finno R.J. (1998) A unique critical state for sand?. *Journal of Geotechnical and Geo-environmental Engineering*, Vol. 124, No.11, p:1100-1108.

Muhlhaus H.B. and Vardoulakis I (1987) The thickness of shear bands in granular materials. *Géotechnique* 37, No. 3, p:271-283.

Nadal A. and Wahl, A.M. (1931) *Plasticity*. McGraw-Hill.

Oda,M. and Kazama, H. (1998) Microstructure of shear bands and its relation to the mechanisms of dilatancy and failure of dense granular soils. *Géotechnqiue* 48, No.4, p:465-481.

Oda, M. and Iwashita, K. (eds.) (1999) *An introduction: mechanics of granular materials*. Balkema. Rotterdam.

Palmer A.C. and Rice J.R. (1973) The growth of slip surfaces in the progressive failure of over-consolidated clay. *Proc. Roy. Soc. London*, A 332 , p:527-548.

Papamichos, E. and Vardoulakis, I. (1995) Shear band formation in sand according to non-coaxial plasticity model. *Géotechnique* 45, No. 4, p:649-661.

Pradel, D. and Lade, P.V. (1990) Instability and plastic flow of soils. II: Analytical Investigation, *Journal of Engineering Mechanics*, Vol.116, No.11, p:2551-2566.

Reynolds, O. (1885) On the dilatancy of media composed of rigid particles in contact. With experimental illustrations, *Phil. Mag.*(2) 20, p:469-481.

Rice, J.R. (1975) On the stability of dilatant hardening for saturated rock masses. *J. Geoph. Res. 80*, p:1531-1536.

Rice, J.R. (1976) The localization of plastic deformation. In: Koiter, W.D. (ed), *International congress of theoretical and applied Mechanics*, North-Holland, Amsterdam.

Rowe, P.W. (1969) Osborne Reynoldes and dilatancy. *Géotechnique* 19, No. 1, p:1-8.

Rowe, P.W. (1962) The stress-dilatancy relation for static equilibrium of an assembly of particles in contact. *Proc. Royal Soc.* Vol. 269, p:500-527.

Rowe, P.W.(1971) Theoretical meaning and observed values of deformation parameters for soil. *Proc. Royal Soc.* Vol. 269, p:500-527.

Roscoe, K.H. (1970) The influence of strains in soil mechanics, *Géotechniqu*e 16, No. 3, p:129-170.

Roscoe, K.H., Schofield, A.N. and Thurairajah, A. (1963) An evaluation of test data for selecting a yield criterion for soils in laboratory shear testing of soils. *American society for testing and materials* STP No.361.

Rudnicki, J.W. and Rice, J.R. (1975) Conditions for the localization of the deformation in pressure-sensitive dilatant materials, *J. Mech. Phys. Solids* 23, p:371-394.

Scarpas, A.and Blaauwendraad, J. (1998) Experimental calibration of a constitutive model for asphaltic concrete. In *Proceedings of the Euro-C 1998 Conference on Computational Modelling of Concrete Structures*, p: 193-202, Balkema, Rotterdam.

Skempton, A.W. (1964) Long-term stability of clay slopes. *Géotechnqiue* 14, p:77-101.

Tatsuoka, F., Molenkamp, F., Torri, T. and Hino, T. (1984) Behaviour of lubrication layers of platens in elemental tests. *Soils and Foundations,* Vol. 24, No. l, p:113-128.

Tatsuoka, F., Nakamura, S., Huang, C. C., and Tani, K. (1990) Strength anisotropy and shear band direction in plane strain tests on sand. *Soils and Foundations*, Vol. 30, No. 1, p:35-54.

Tatsuoka,F, Molenkamp, F., Van Deventer, J., Pedersen, A. and Smidt, L.(1982) Stress and strain histories during sample preparation and its effects on deformation properties of sand under low confining pressure, *GeoDelft Internal Report*.

Teunissen, J.A.M. and Spierenburg, S.E.J. (1995) Stability of infinite slopes. *Géotechnique* 45, No. 2, p:321-323.

Vardoulakis, I. and Sulem, J. (1995) *Bifurcation analysis in geomechanics*. Blackie Academic and Professional, Glasgow.

Vermeer, P.A.(1990) The orientation of shear bands in biaxial tests, *Géotechnique* 40, No.2, p:223-236.

Wood, D.M. (1990) *Soil behaviour and critical state soil mechanics*. Cambridge University Press. Cambridge.

References (Chapters 4,5,6)

Allersma, H.G.B. (1993) New design of a biaxial apparatus for soft soils, *Report 354, Geotechnical laboratory*, TU Delft, The Netherlands.

Anandarajah, A. (1994) Discrete-element method for simulating behaviour of cohesive soil , *J. Geotech. Engng. Div., ASCE* 120, No.9, p:1593-1613.

Arnarson, T. S. & Keil, R. G. (2000) Mechanisms of pore water organic matter adsorption to montmorillonite. *Marine Chemistry* 71, p:309-320.

Atkinson, J.H. (2000) Non-linear soil stiffness in routine design. the 40th Rankine lecture, *Géotechnique*, Vol. 50, No. 5, p:457-472.

Barends, F.B.J. (2002) The squeeze problem, *Learned and applied soil mechanics out of Delft*, (Barends & Steijger, eds), Balkema, p:45-50.

Bolton, M. D. (1999) The role of micro-mechanics in soil mechanics, Presented at *The International Workshop on Soil Crushability*, Yamaguchi University, Japan.

Brinkman, J. (1992) *Reinforced gravel piles*, MSc thesis, Delft University of Technology, The Netherlands (in Dutch).

Cheng, X., Janssen, H., Barends, F. B. J. & Den Haan, E. J. (2004). A combination of ESEM, EDX and XRD studies on the fabric of Dutch organic clay from Oostvaardersplassen (Netherlands) and its geotechnical implications, *Applied Clay Science*, Vol. 25, Issues 3-4, p:179-185.

Cheng, X., Den Haan, E.J. and Barends, F.B.J. (2004) Unusual fabric of Dutch organic clay and its implication on geotechnical properties, submitted to *Soils and Foundations*.

Cleveringa, P., De Gans, W. & De Wolf, H. (1995) Natural gas in Amsterdam underground, *Our Amsterdam* 47, No.1, 3pp (in Dutch).

Davis, E.H.and Raymond, G.P. (1965) A non-linear theory of consolidation, *Géotechniqu*e, Vol.15, No2, p:161-173.

Den Haan, E.J. (1996) A compression model for non-brittle soft clays and peat, *Géotechnique* Vol. 46, No.1, p:1-16.

Den Haan, E.J. (2002) The influence of creep ageing on $K_{o,nc}$, *Learned and applied soil mechanics out of Delft*, (Barends & Steijger, eds), Balkema, p:63-68.

Den Haan, E. J.(1999) Dutch cell test or triaxial test, *Geotechniek* 3, No.1, p:5-11.

Den Haan, E.J. (1995) Theme report on special problem soils / soft rocks. Part I: Peats and Organic Soils, *Proc. 11th ECSMFE*, Copenhagen, Vol. 9, p:139-156.

Den Haan,E.J. and Kamao, S. (2003) Obtaining isotache parameters from a C.R.S. K_o-oedometer. Soils & Foundations, 43, Aug., 4, p:203-214.

Goldstein, J. I. (1981) *Scanning Electron Microscopy and X-Ray Microanalysis*, Plenum Press, New York.

Grabowska-olszewska, B., Osipov, V. & Sokolov, V.(1984) *Atlas of the microstructure of clay soils*. Warszawa: Panstwowe Wydawnictwo Naukowe.

Hale, J. and Kocak, H. (1991) *Dynamics and bifurcations*, Springer-Verlag, New York Inc.

Hambly, E.C. (1972) Plane strain behaviour of remoulded normally consolidated kaolin, *Géotechnique* 22, No. 2, p:301-317.

Hvorslev, M.J.(1960) Physical components of the shear strength of saturated clays, *Proceeding of research conference on shear strength of cohesive soils*, ASCE, p:169-216.

Loret, B. and Prevost, J.H. (1990) Dynamic strain-localization in elasto-visco-plastic solids-Part 2: Plane strain examples, *Comput. Meth. Appl. Mech. and Eng.*, Vol. 83, p:275-294.

McDowell, G. R. & Harireche, O. (2002) Discrete element modeling of soil particle fracture, *Géotechnique* 52, No.2, p:131-135.

Mitchell, J. K. (1992) *Fundamentals of soil behavior*, New York: Wiley & Sons Inc.

Nakata, Y., Hyde, A. F., Hyodo, M. & Murata, H. (1999) A probabilistic approach to sand particle crushing in the triaxial test, *Géotechnique* 49, No.5, p:567-583.

Oka, F., Adachi, T. and Yashima, A. (1994) Instability of an elastic-viscoplastic constitutive model for clay and strain localization, *Mechanics of Materials*, Vol.18, p:119-129.

Paul, M. A. & Barras, B. F. (1999) Role of organic material in the plasticity of Bothkennar Clay, *Géotechnique* 49, No. 4, p:529-535.

Plaxis BV (1999) Plaxis manual, Balkema.

Pradel, D. and Lade, P.V. (1999) Instability and plastic flow of soils II: Analytical Investigation, *J. Eng. Mechanics*, Vol. 116, No. 11, p:2551-2566.

Pruiksma, J. P.(2002) *Biaxial test simulations with PFC2D*, GeoDelft Report CO386730/05, The Netherlands.

Sabatini, P.J. and Finno, R.J. (1996) Effect of consolidation on strain localization of soft clays, *Computers and Geotechnics*, Vol.18, No. 4, p:311-339.

Skempton, A.W. and Petley, D.J. (1970) Ignition loss and other properties of peats and clays from Avonmouth, King's Lynn and Cranberry Moss, *Géotechnique* 20,No. 4, 1970 p:343-356.

Smart, P. & Tovey, N. K.(1981). *Electron microscopy of soils and sediments: examples*. Clarendon press, Oxford.

Tanaka, H. & Locat, J. (1999) A microstructural investigation of Osaka Bay clay: the impact of microfossils on its mechanical behaviour, *Can. Geotech. J.*, Vol. 36, p:493-508.

Tigchelaar, J., De Feijter, J.W. & Den Haan, E. J.(2000) Shear tests on reconstituted Oostvaardersplassen clay, *Proc. Conf. Soft Ground Technology*, Noordwijkerhout, The Netherlands, p:67-81.

Tigchelaar, J.(2001) Experimental study of the behaviour of organic clay. *GeoDelft report* CO-710203/28.

Turner, A. and Millward, G .E.(2002) Suspended particles: their role in estuarine biogeochemical cycles, *Estuarine, Coastal and Shelf Science* 55, p:857-883.

Topolnicki, M. (1987) Observed stress-strain behaviour of remoulded saturated clay and examination of two constitutive models, PhD Thesis, TU Karlsruhe.

VanBaars, S. (1996) *Discrete element analysis of granular materials*, PhD thesis, Delft University of Technology, The Netherlands.

Vardoulakis, I. (1985) Stability and bifurcation of undrained, plane rectilinear deformations on water-saturated granular soils, *Int. J. Numerical and Analytical Methods in Geomechanics*, Vol. 9, p:399-414.

Wissa, A.E.Z.and Christian, J.T. (1971) Consolidation at constant rate of strain, *J. Soil Mechanics and Foundations Div.*, Vol. 97, No. SM10, p:1393-1413.

Curriculum Vitae

Xiaohui CHENG

Gender: Male

18 October 1971
Born in Jiangsu, China

February 2000—June 2004
Doctoral researcher
Subject: Localization of soil mechanics
Department of GeoTechnology TU Delft The Netherlands

March 1999—November 1999
Visiting researcher
Subject: Development of a dynamic penetration testing device
CUST, Blasé Pascal University, France

March 1997—March 1999
Assistant professor & Lecturer
Subject:Computer-aided design and FEM analysis of soil nailing embankment
Department of Civil Engineering, Tsinghua University, Beijing, China

September 1994—March 1997
Graduate student (M.Sc.)
Majored in Earthquake and Protective Engineering,
M.Sc.Thesis: Laboratory investigation of seismic behaviour of reinforced concrete beam-column joint for mega-structures
Department of Civil Engineering, Tsinghua University, Beijing, China

September 1989—June 1994
Undergraduate student (B.Sc.)
Majored in Structure Engineering
Department of Civil Engineering, Tsinghua University, Beijing, China